Università degli Studi di Padova - Facoltà di Ingegneria

CORSO DI LAUREA MAGISTRALE
IN INGEGNERIA DELLE TELECOMUNICAZIONI
Anno Accademico 2011/2012

THERMAL CHARACTERIZATION AND OPTICAL RELIABILITY INVESTIGATION OF HIGH-POWER WHITE LEDS

RELATORE: Ch.mo Prof. Enrico Zanoni
CORRELATORE: Ing. Matteo Meneghini

LAUREANDO: *Alessandro Compagnin*

12 Dicembre 2011

Mi era difficile staccarmi da lei.
Mi accompagnò fino alla soglia e la baciai nel vano della porta aperta,
perchè Schmitz e sua moglie là di fronte potessero vedere.
Ci fissarono con gli occhi sbarrati come dei pesci
che scoprono con improvvisa sorpresa
di aver già inghiottito l'amo da un pezzo.

HEINRICH BÖLL - Opinioni di un clown

Contents

Abstract

The solid state lighting has become more and more interesting in the last decade, and innovative lamps based on the white GaN-based LED technology are proposed to substitute the incandescent and fluorescent light sources. Once the superior efficiency of the LEDs towards the old light sources is demonstrated, there is the need to improve their light quality and to increase this technology's reliability, in particular preventing significative changes in its optical and electrical behaviour during its lifetime. In the last years many works demonstrated the thermal issue to be one of the principal problems of this technology, that is itself limiting its efficiency and moreover reliability.

The aim of this work is to fully characterize white high-power LEDs provided by three different manufacturers by the thermal and optical point of view: the use of two MCPCBs is adopted to put in evidence the different thermal management that can be achieved using one or another board, and the different performance that can be obtained by the power devices mounted on it. An accelerated ageing is conducted, imposing a high junction temperature and verifying the changes of the optical and electrical characteristics of the devices during the stress.

The results are pretty different in the three cases, but the two conditions at which the devices were stressed highlight the fact that the involved processes were almost current-induced. The prevalent degrading mechanism has been the creation of nonradiative centers, which is found in the lowering of the optical power and in the increase of the parallel resistance. In some cases also an increase of the serial resistance has been verified, probably due to the worsening of the ohmic contacts.

Introduction

In the last decades the research and development of new technologies has focused on a new and important objective: the optimization and complexive reduction of electrical energy use, in order to achieve not only a substantial economic benefit, but also an active climate change mitigation.

Improved technologies hold great potential for energy savings and for reducing associated gas emission. Among all the bigger innovations in many sectors, such as automotive and solar panels, the white Solid State Lighting (SSL) shows great promise as a source of efficient, affordable, color-balanced white light. Because of this, both the R&D departments of the major lighting industries and the academic research have improved their efforts in this matter, developing firstly a reliable high-power red LED family, such that one based on GaAsP technology, and then searching for a new white light source based on InGaN-GaN LEDs: today this is a new technology, that is destined to completely substitute the most diffused forms of lighting, such as incandescent and fluorescent lamps but, since it is still unreliable, it needs to be examined, proved and perfectioned to fully participate to the lighting innovation process.

An important step in the great and complex process of dismounting all the old and inefficient forms of lighting has been made over the coming decade by many countries like Australia, Brazil, Canada, Ireland, Italy, New Zealand, United States and Venezuela. All these countries have recently moved to implement a phaseout of standard incandescent bulbs

[1]. Actually, among the most old-fashioned sources of light, and apart from the ones used where there is no access to electricity such as oil and paraffin lamps, the incandescent is the more inefficient: it converts only between the 1% and the 5% of the absorbed power in usable light, with an *efficacy* (the ratio of the light output to the input electric power) of only 18 lm/W. This gradual passage from the most inefficent incandescent lighting to the SSL technology is not easy, principally because at the state of art there are no SSL lamps capable of meeting all the consumer's needs. For instance, is not still possible to find a white LED lamp on the retail market with a certain color temperature, and at a reasonable price: if it happens, most cases they are low-quality products, made to work well in the first hours of life, but to considerly decrese their performance under stress conditions. Because of this, getting rid of incandescent bulbs further motivates the developement of more reliable and costumer-suitable LED lamps.

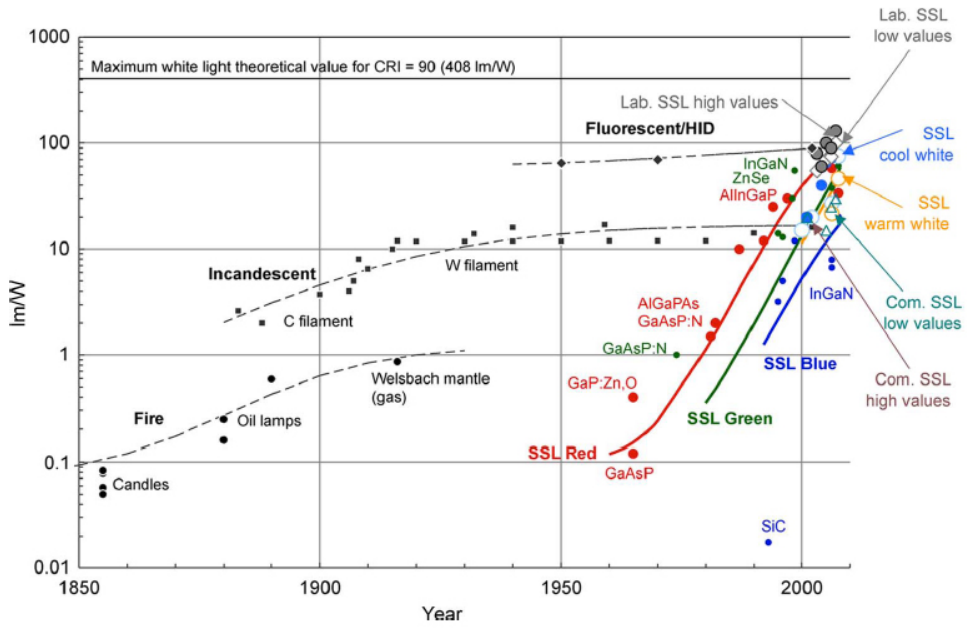

Figure 1: Efficaces of selected lighting technologies between 1850 and 2006. Lab.= laboratory; Com.= commercial. (Figure taken from [1].)

While the red and green LEDs technologies have already reached the efficacy levels of the conventional lighting, the white ones are not so efficient (and overall reliable), but they are expected to be so in the next few years: while the old technologies are yet stable and no

improvement could be imagined on them, the LED technology could reach a much greater potential in a much shorter time, as it is shown in Figure 1. Since bright InGaN-based blue LEDs were commercialized in 1993, there has been considerable interest in improving their output power and moreover their reliability [9].

The aim of this thesis work is to carry out a systematic and accurate study of the white SSL behaviour, especially under stress conditions; in particular, in order to clarify this aspect, we reproduced the more common stress conditions and verified the functionality of three sets of white LEDs, provided by the three leading manufacturers. During the stress the devices was measured as well and the degradation kinetics were deeply analyzed, in order to qualify and quantify the mechanisms that brought to certain changing in the electrical, thermal and optical behaviour of the investigated devices. As the principal degrading causes are thermally-activated, a special investigation has been conducted about the thermal characterization of the studied devices: in particular the thermal resistance of the used printed board has revealed to be quite critical in the heat management during stress, bringing to consider a medium - current ageing and suggesting the use of a different board type during a second ageing process, in which the devices were stresses under high current conditions.

The experimental results will be discussed in the last chapters, while we previously need to consider some basilar characteristics concerning the world of the SSL, especially its principal rules and phenomenology. This thesis report is thus structured in eight chapters:

Chapter 1 describes the principal characteristics of a lighting source, such as color temperature and luminous flux, together with the physical methods and measurement units used to define them.

Chapter 2 will explain how a light emitting diode works, the differences between several compounds and their intrinsic efficiency issues will be stressed from the basilar semiconductor interactions to the simplest LED chip.

Chapter 3 provides the electrical, thermal and optical characterization of a common LED device, the design characteristics of the most used LED chip configurations, and the features of a white LED .

Chapter 4 will report the data concerning each type of device considered during the experimental work, underlining the most critical ones.

Chapter 5 will include the description of the setup used in the lab, the instrumentation and the methodology applied on the measurements of the electrical, thermal and luminous behaviour of the devices.

Chapter 6 will deal with the setup of the devices, in particular the two types of board applied in the measurements, the using of a proper heatsink and thermal interfaces, and their thermal characterization.

Chapter 7 will be focused on a critical analysis of the principal degrading dynamics of LEDs and the exposition of practical results concerning the achieved stress level in the final part of the thesis work.

Conclusions and comments to the experimental details will be reported in the last chapter, where the problems overcome and some suggestions for future challenges will be further deepened.

As the first theoretical part is given in order to better understand the experimental details, these are reported together with some references to related works that involved similar stress conditions and that have been used as well to explain the results here obtained.

CHAPTER 1

The photometric quantities

In this chapter will be presented and discussed the principal features of a light source, such as brightness, efficacy and color, and the way we measure them. These are all basic notions, that we will use in the next chapters. In particular the human eye color perception will be explained, in order to better understand the chromatic properties of a lamp that are not absolute values, but are always to be referred to how the human being perceives them.

Firstly, it is important to know that in order to classify a lamp as a "good" source of light, it must satisfy not only obvious criteria, concerning power consumption and efficacy, but also more qualitative requirements, like the color quality, the lifetime and the way the lamp decreases its performance during its life. We will introduce here the concept of *lumen*, the measurement unit of the luminous flux, and the *temperature color*, another unit that classifies the quality of the light [1]. In order to stay coherent with the promotion of the SSL technology, we will compare its features with the ones of the traditional lighting lamps, observing that sometimes they are right better, and sometimes they have to be developed as well.

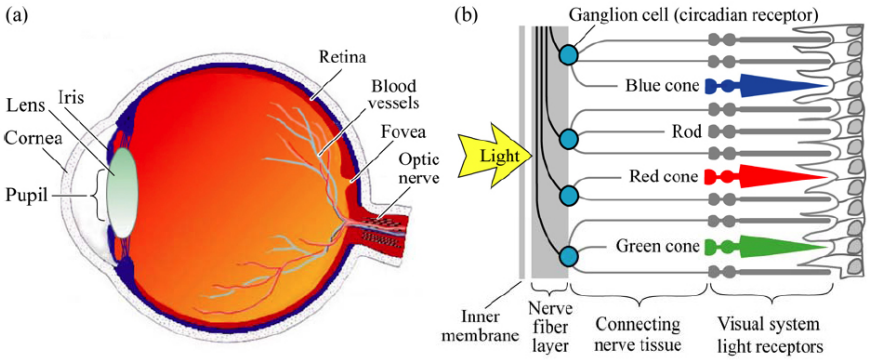

Figure 1.1: A representation of the human eye, where the retina conformation is highlighted. Note the presence of two type of light receptors, the cones and the rods. (Figure from [4].)

1.1 The human eye light perception

The light-sensitive elements of the human eye are the *cones* and the *rods*. As in Figure 1.1, they form the *retina*, which is the part of the eyeball apted for light reception and translation into signal to be sent to the brain.

Since the rods are more abundant and more light sensitive than the cones, they apt in low lighting conditions, forming the *Scotopic vision*, while the cones are well suitable for normal daylight vision, called *Photopic vision*. As reported in Figure 1.2, the sensitivities of the three types of cones are peaked at different wavelengths, so each cone is able to reveal a quite strict portion of the visible, while the combination of these three signals renders the actual whole visible spectrum. On the other side the rods are not color-sensitive, and that is the reason why in low light conditions the color distinguish is difficult.

Notice that in this tractation the photopic vision characteristics will be described, in particular the three cones sensitivity will be considered because they are the basis of the color matching functions development.

1.2 The luminous flux

The measurement unit to evaluate the luminous flux coming from a light source is the *lumen*, that represents the light power of a source as perceived by the human eye. A luminous flux of 1 lm is defined as the light flux of a source that emits an optical power of $1/683$ W at a wavelength of 555 nm [1].

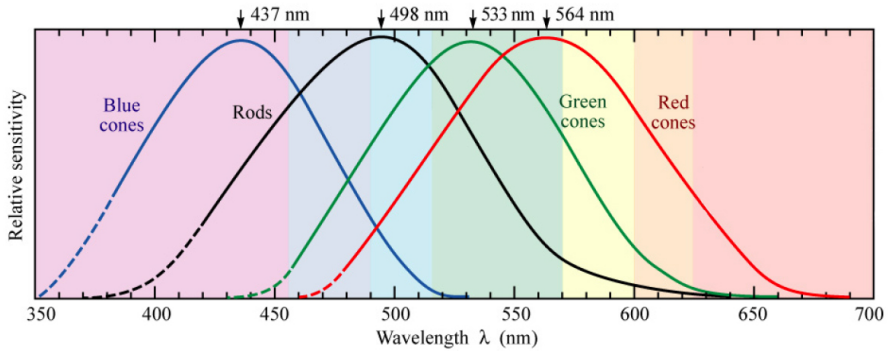

Figure 1.2: The sensitivity functions of the three types of cones and rods, over the visible spectrum. (Figure adapted from [4].)

Because the lumen definition involves the way the human eye perceives the light, we should consider its sensitivity, that is reported in Figure 1.3 as a function of the wavelength, and is very close to the relative sensitivity of the green cone: it is characterized by a function, named $V(\lambda)$, that has a maximum corresponding to the green color, at 555 nm.

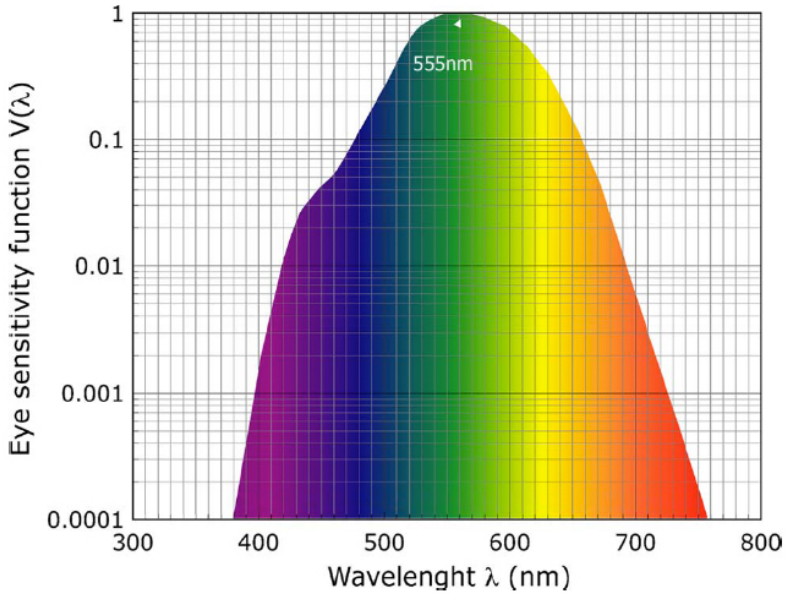

Figure 1.3: Photonic sensitivity of the human eye, $V(\lambda)$. (Figure from [1].)

The lumen is an indirect evaluation of the light flux, that comes from an integral over the visible spectrum of the measured light power $P(\lambda)$. If we consider the mathematic definition

(1.1), and notice that at 555 nm the human eye sensitivity is 1, we can see that a theoretical upper bound for the light flux is 683 lm.

$$\Phi_{lm} = 683 \frac{lm}{W} \int_{\lambda} V(\lambda) P(\lambda) d\lambda. \tag{1.1}$$

It is even possible to measure the photons rate, or the light power, coming out from a light source using special instruments, such as the *integrating sphere*, described in details in chapter 5.3, that allows to collect the whole light radiation from the source, not only the one that can be seen from a particular angulation. In this way a high-level of repeatibility of the measurements is garanteed, and so the spectrum and efficacy measurements are highly reliable.

1.3 The efficacy

The *efficacy* of a lamp is its ability to convert the absorbed power into luminous flux: numerically, it is the ratio between the luminous flux (in Lumens) of light output to the input electric power (in Watts). Whereas if we compare the output power expressed in watts, as happens for the electronics, with the input one, we will obtain a percentage number, called *efficiency*. Because of the existence of some electronic stadium, especially in LED lamps, it is important to compare systems on an equal footing: the electronic ballast absorbs and consumes some power itself, thus the power that reaches the LED is less than the amount absorbed from the network. This observation rises the need to distinguish between the *system efficacy*, that takes on account both the efficiency of the electronic ballast, the device itself and even the fixture efficiency, and the *device efficacy*, that evaluates just the efficacy of the light source. Figure 1.4, depicting the range of the whole system efficacy for various light sources, clearly points out the difference of the two quantities discussed above: the LED efficacy is shown to be the higher, and the whole lamp capability is still limited by the ballast and fixture stadiums.

In this chapter we will deal with the system efficacy since it is the more useful quantity for a macro-level evaluation of the light source performance. Whereas in the next chapters, where we will study only the LED device, we will consider the device efficacy and dissociate all its components.

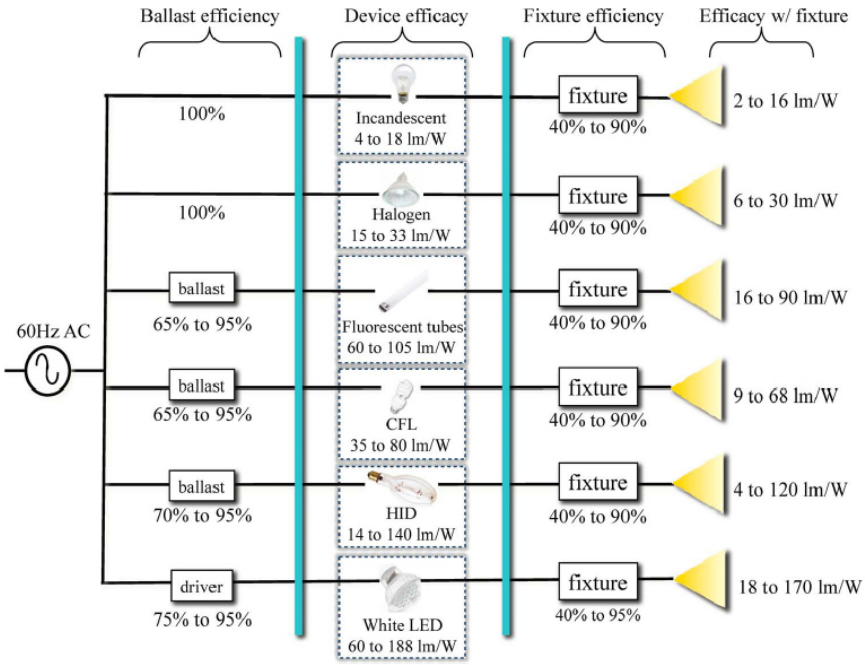

Figure 1.4: Range of variability of the efficacy of lighting devices and systems. CFL = Compact Fluorescent Lamps; HID = High - Density Discharge. (Figure taken from [1].)

The ballast efficiency While the halogen and fluorescent lamps work using directly the 50 Hz AC electric energy from the network, and because of this there were no losses induced by electronic stadiums, the most advanced light systems like LEDs need a particular feeding system that provides a stable flux of DC current. Obviously this introduces additive losses, represented in the leftmost column in Figure 1.4, that limit the whole lamp efficacy.

The fixture efficiency Another loss is due to the fixture applied to the lamp: since the light source alone is not able to offer a pleasing diffused light, there is the need to put it in a variety of fixtures, that reduce the complexive lumen extraction from the lamp. In the case of LED lamps, being this a brand new technology, fixture designers have the freedom to develop new fixtures with much lower losses.

The device efficacy For our considerations the most important term to deal with is the device efficacy, because in this case the LED technology is dominant, and can be much developed. In the following we will examine not only the reasons why the efficacy is limited in the common light sources, but also the mechanisms that lower it during its life.

For the incandescent lamps, the device efficiency is limited by the tungsten filament efficacy, and the lumen depreciation is caused by the filament evaporation inside the bulb: this lowering of the light output ranges from 10% to 15% of the initial output over the course of a lifetime of $\sim 1000\ h$. This process can be limited using certain noble gases inside the bulb, but it is evidently an intrinsic limit of the lamp.

In the fluorescent lamps, the efficacy is much higher than in the incandescent ones, but it is limited too: the constraint is mainly due by the double-conversion process that occurs inside the tube, and more precisely by the phosphors efficacy. The main process that leads to a light lowering during the lamp lifetime is the phosphor degradation, the accumulation of light-absorbing deposits within the lamp and the deterioration of the cathote participate too. Fluorescent lamps usually experience less than 20% depreciation over their 10000 h lifetime, a much better performance than the one of the incandescent.

For both these kinds of lamps, the lumen depreciation is due to intrinsic processes, that can be limited but not eliminated over a certain level. In the case of LEDs the efficacy is generally lowered because of a poor removal of the heat generated at the junction, leading to an increase of the lamp temperature, which results in a lower light output. This depends principally by the chip design, that can be improved in order to better promote the flux of heat outside the junction and towards the thermal pad, to induce the flux of electrons inside it and, the principal one, the flux of photons towards the collector dome. Because of the use of phosphors in white LEDs, the down-conversion of light is another term that influences the complexive device efficacy: all these aspects will be studied in detail in chapter 3.

As concerns the SSL based on LED technology, it has undergone dramatic improvements since it has been developed in 1996. Today the efficacy of a cool white LED is around 80 lm/W, and the aim is to bring it to 174 lm/W by 2015 [1]. In this scenario, the LED technology efficiency would overcome the one of all the best existent commercial light sources and, if equal improvements would follow in the thermal stabilization as well as in color and ageing control, this technology would soon substitute the traditional lamps.

Some of the targets provided by the DOE (U.S. Department Of Energy) both for luminaires and for devices of warm and cool white LEDs are reported in Figure 1.5, looking at the figure we can notice that the complexive trend is exponential, and the efficacy in laboratory devices is expected to overcome 200 lm/W by 2015.

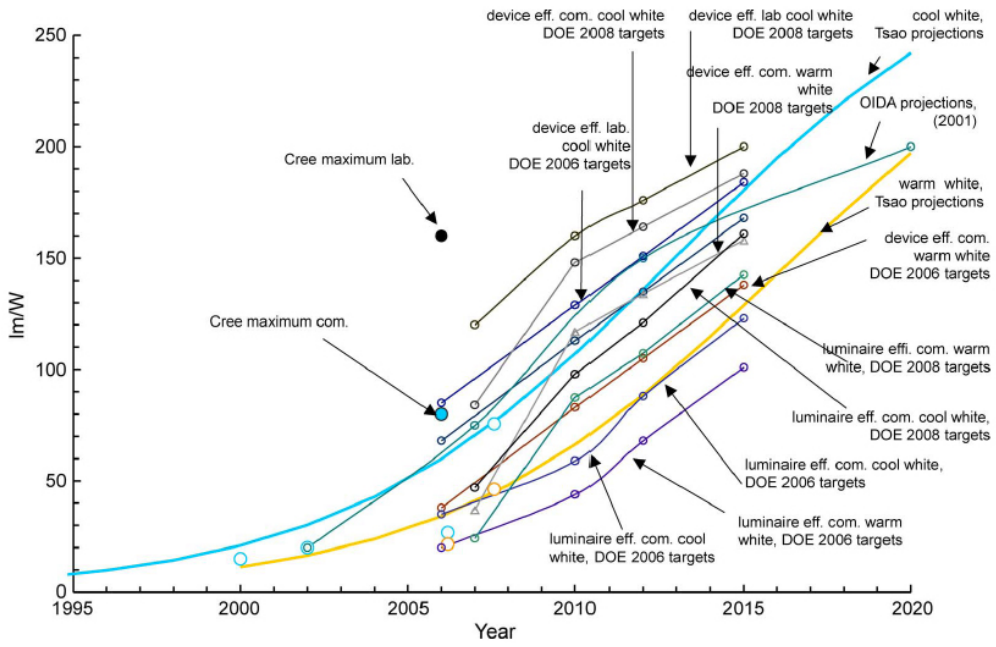

Figure 1.5: Laboratory and commercial efficacy projections for cool and warm white LEDs. (Taken from [1].)

1.4 The color

As stated before, not only the quantitative characteristics of a lamp, like the ones already explained, are interesting. Also the light color and the way it reveals the object color are preponderant in a lamp choice: in this section we are going to better explain the concept of color, rendering index and color temperature for a common light source, and we will apply these concepts to the LED world.

Solar radiation at the top of the atmosphere has a spectrum that is close to the one of a black body with a temperature of 5500 K. The solar spectrum is reported in Figure 1.6, here it can be noticed that the radiation at sea level in the visible region has the same trend of the human eye sensitivity, reported in Figure 1.3: this match is obvious because the human eye evolved in the context of the Earth's natural illumination. In order to reproduce a perfectly white light, or somewhat that our eye perceives like white light, we just need to assembly the colors, for example three monochromatic blue, green and red LEDs or, as we will see in the next chapter, simply putting yellow phosphors over a blue LED chip, so providing a

two-peaks spectrum. The light obtained would be perceived as white, but if an object's color lies between two peaks of this source illumination, it would be revealed in the wrong way. This way to render colors, that is the core of the color-matching theory and the principal issue in the right color-mixing in today's white LED production, needs a definition, as strict as possible. Unfortunately none of the strategies so far developed excels in this issue, but we can consider the most common ones developed by the Commission Internationale de L'Éclairage (CIE) [1].

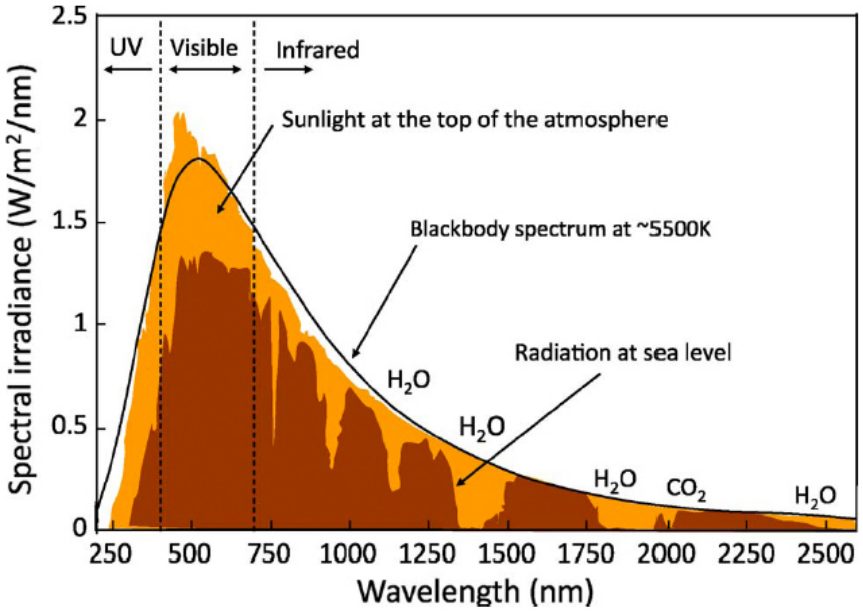

Figure 1.6: Solar radiation at the top of atmosphere (orange) and at the surface (red) as compared with a black body at 5500 K. (From [1].)

The color matching functions The CIE has developed a set of three functions, the *color matching functions* (CMFs), in order to simply classify the colors present in nature. The theoretical basis is that every color can be perceived by the human eye if it is producted by a certain combination of the three basilar red, blue and green colors. This is called *color-matching theory*, and is the basilar principle of all the RGB applications now existent. In particular, it is possible to identify over the visible spectrum three functions, $\bar{x}(\lambda)$, $\bar{y}(\lambda)$ and $\bar{z}(\lambda)$, represented in Figure 1.7, that render the level of stimulation of the red, green and blue cones respectively. As a matter of fact, the three CMFs are quite similar to the relative

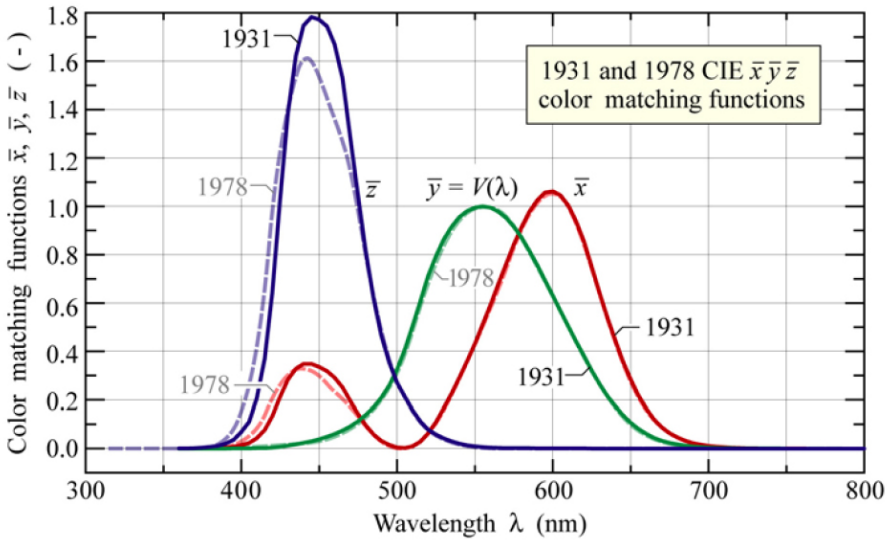

Figure 1.7: CIE 1931 and CIE 1978 $\bar{x}(\lambda)$, $\bar{y}(\lambda)$ and $\bar{z}(\lambda)$ color matching functions (CMFs). The $\bar{y}(\lambda)$ CMF is identical to the eye sensitivity function $V(\lambda)$. Note that the CIE 1931 CMF is the currently valid official standard. (From [4].)

sensitivity of the three cones, and an illumination of the eye with a certain light source $P(\lambda)$ can produce a certain stimulation X, Y and Z for each cone given by the following:

$$X = \int_{\lambda} \bar{x}(\lambda)P(\lambda)d\lambda; \tag{1.2}$$

$$Y = \int_{\lambda} \bar{y}(\lambda)P(\lambda)d\lambda; \tag{1.3}$$

$$Z = \int_{\lambda} \bar{z}(\lambda)P(\lambda)d\lambda. \tag{1.4}$$

Notice that the CMFs have no measurement unit, so the value of the three relative stimulations is expressed in Watts. These indexes are used to produce a very important diagram, the *color chromaticity space*.

The color chromaticity space A normalization of the X, Y and Z values is possible in order to represent in a two-dimensional diagram, reported in Figure 1.8, the colors perceived by the human eye. These coordinates (x, y) are obtained by the following:

$$x = \frac{X}{X + Y + Z}, \tag{1.5}$$

$$y = \frac{Y}{X + Y + Z}, \tag{1.6}$$

where the third, z, is obtained from the other two through the relation $z = 1 - x - y$ and can be ignored in the diagram. These relations are very important because they derive from an evaluation of the light properties weighted by the human eye sensitivity, then they render the actually perceived color; once they are calculated for a specific light source, it is possible to extract the color rendering index and the color temperature of that source.

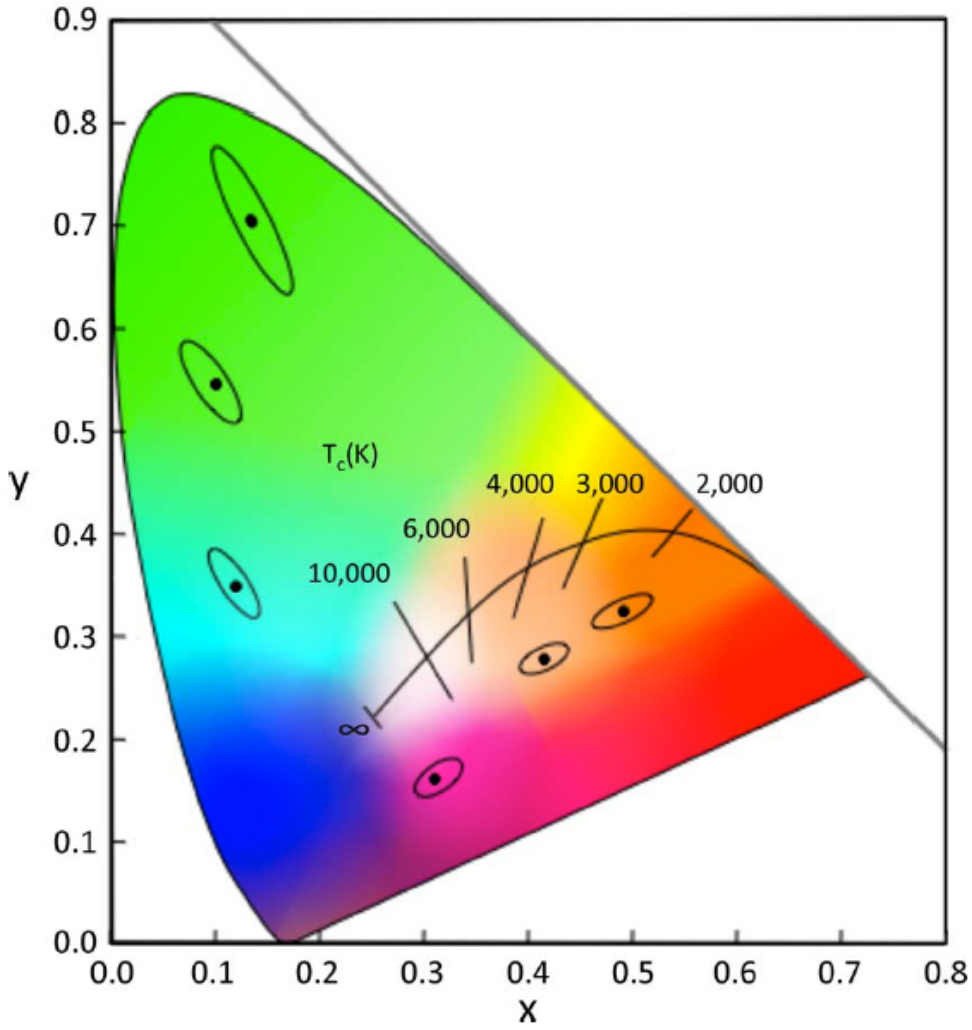

Figure 1.8: CIE color chromaticity space, from [1]

Figure 1.8 shows that the pure colors lay on the edges of the space, while the white is in the center. The black line in the center of the space is called *Wein's law*, and it represents the radiation of an ideal black body with the reported temperature. If a light source emits

radiation with a spectrum similar to a black body, like and incandescent bulb, it is common to refer to that source with the temperature of the corresponding black body, called the *color temperature*. This reference is not always possible, nonetheless if a white-light source does not lay on the black body curve it can be characterized by a *correlated color temperature* (CCT), according to where it intercepts the lines crossing the Wein's law. It is also important to notice that the higher is the temperature of a source, the cooler appears its radiation.

The color rendering index Using the color space, it is possible to obtain a very important parameter, the *Color Rendering Index* (CRI), which can be interpreted as the way a light source can render the colors of a generic object.

This index can be measured by illuminating a standard set of color chips with a reference black body radiation, whose temperature is the same of the light source of interest, and then comparing the results with the ones obtained illuminating the same color chips with the light source. Each couple of measurements in the same color chip returns a couple of coordinates (C, D), the average of the Euclidian distance between them, $\Delta\overline{CD}$, substituted in the formula:

$$CRI = 100 - 4.6\Delta\overline{CD}, \tag{1.7}$$

renders the CRI. This proceeding is commonly repeated for just eight standard color chips, among the 14 initially used, and the results are always less than 100: indeed if the light source is perfectly matched by the black body radiation, the distance would be zero and the CRI would be the maximum possible.

Using CRI as an index of light quality means that any deviation from how an object appears when illuminated by a black body is considered bad: in other words, the perfect way to illuminate an object is using a black body radiation, exactly as it happens for the sunlight, or the incandescent light, indipendently from its color temperature. If we want to evaluate another light source, and consider its spectrum, as much the spectrum is far from the one of a black body, as much that source will be bad. For example, if the spectrum of a light source presents some holes of light absorption or not generated, as happens for the fluorescent lamps or for the LED white lamps, represented in Figure 1.9, the CRI would be much less 100.

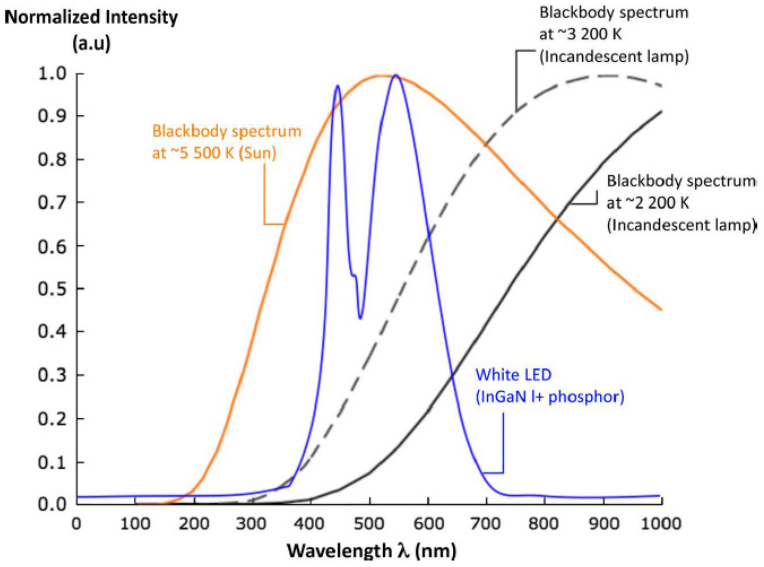

Figure 1.9: Normalized intensity in arbitrary units for a blackbody radiator at $5500\ K$ (Sun), for a black body radiator at $3200\ K$ (warm white incandescent lamp), for a black body radiator at $2200\ K$ (cooler white incandescent lamps), and for a white LED, where the perception of white light is achieved using a blue LED + phosphor. (Figure taken from [1].)

1.5 A brief comparison of lighting technologies

In Table 1.1 is reported a comparison of the key characteristics of the already mentioned lighting technologies. The first thing to notice is that while for the traditional lighting sources the technology is stable and no more significant improvement is possible, for the LED one these data are only indicative and temporary, because they are fastly evolving. This table has been adapted from [1], dated 2009: as we will see in chapter 7, the LEDs measured in this thesis work are fine better than those mentioned here.

Lamp Type	Power (W)	Efficacy (lm/W)	Lifetime (x1000 h)	CCT (K)	CRI
Incandescent	3-150	4-18	1	2400-3100	98-100
Halogen	-	15-33	2-6	3000-3100	98-100
Fluorescent	4-120	35-80	5-20	3000-6500	75-90
SSL LEDs	1-20	160 (lab), 20-55	20-40	5000-6000	70-80

Table 1.1: Main characteristics of lamps, adapted from [1]

CHAPTER 2

Physical principles of a Light Emitting Diode

In this chapter the operating of a common LED will be discussed: considering a standard LED device, we will analyze the physical principles on which it works. We will start from the band representation of a semiconductor, and then discuss what is the difference between a material that can emit light and one that can not. Before considering the mechanisms that induce light radiation, we will study the electrical behaviour of a diode, analyzing the homojunction between two semiconductors and introducing the heterojunction.

2.1 The band model: direct and indirect gap semiconductors

While for a conductive material the conduction and valence bands are not energically separated, thus the transition of electrons between them thanks to their thermal energy is always possible because there is no energy gap, in a semiconductor a transition is more difficult to achieve, because the two bands are well distinguished, as shown in Figure 2.1. In order to obtain, for example, an electron promotion from the valence to the conduction band, an amount of energy equal to the energy gap E_g that it has to overcome has to be externally supplied. On the other hand a decay of one electron from the conduction to the valence band, and the subsequent recombination with a hole can give origin to a radiation

process, that is accompained by a release of a photon with a frequency $\nu = E_g/h$[1].

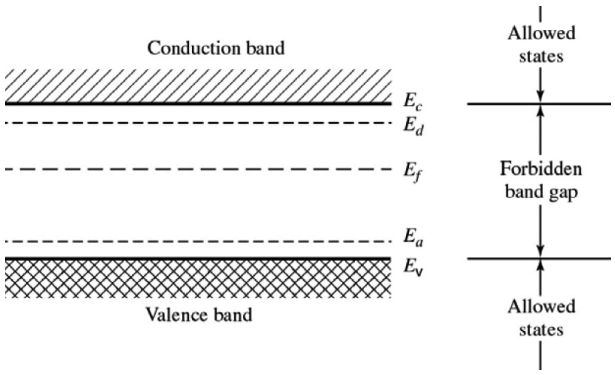

Figure 2.1: The conduction and valence band scheme, in a semiconductor. (From [2].)

A distinguish is now necessary, because not all the semiconductors can give origin to light radiation phenomena: this happens only for *direct bandgap* semiconductors, such as GaAs, InP or InGaAs, because the transition between the bands does not need other energy than the one absorbed or released by the electron. Figure 2.2 shows the energy curves versus momentum of an electron inside the valence band (VB) or the conduction band (CB), the curves suggest that the only minimum-energy transition possible is the one in which both the electron in the CB and the hole in the VB have momentum $p = 0$.

Those diagrams can be obtained considering that for free electrons the following identity holds:

$$E = \frac{p^2}{2m_0} = \frac{1}{2}m_0 v^2, \tag{2.1}$$

with $p = m_0 v$, m_0 the electron mass and v its group velocity inside the semiconductor lattice.

In an indirect bandgap semiconductor, i.e. Si, a radiative decay is still possible but, as we notice from Figure 2.2 (a), the minimum-energy transition occurs only with an additive energy contribution, called *phonon*, that is a packet of vibrational energy that rebalances the momentum of the electron. Because of the improbability of this spontaneous contribution of phonons to the lattice, this transition hardly happens thus this kind of semiconductors are not used as light emitters.

[1]The formula $E_g = h\nu$ contains the radiation frequency ν and the Planck constant $h = 6.63 \cdot 10^{-34}\ Js$

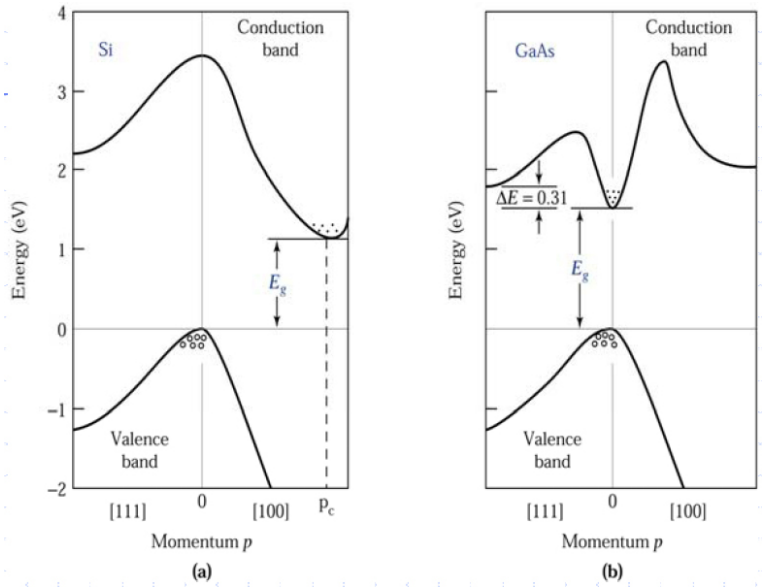

Figure 2.2: Energy vs momentum diagram in a indirect Si (a) and direct GaAs (b) gap semiconductor. (From [2].)

2.2 Doped semiconductors

In nature, an intrinsic semiconductor is not very useful, because at steady state the promotion and decay processes are balanced, and it is not able neither to produce nor to absorb additive photons. If we want to increase, for example, the number of radiative decays, it has to be doped, introducing into the lattice some imperfections, i.e. atoms that can raise the number of electrons or lower it (in this case it is said the doper would raise the number of holes). As we will see in detail further on, doping a semiconductor creates an unbalanced electric field in the lattice, that allows the creation of a special region.

Let's call n the density of donor elements inside a semiconductor lattice, i.e. electrons, and p the number of acceptor ones, i.e. holes. If the semiconductor, for example Si, is not doped, for the law of the charges balancing we have $n = p = n_i$ where n_i is the free electrons density in the CB, that can be calculated by

$$n_i^2 = BT^3 \exp\left\{-\frac{E_g}{kT}\right\} \tag{2.2}$$

where we can notice the strong dependency from the temperature T and the band gap E_g. The silicon lattice is kept together by covalent bonds, as depicted in Figure 2.3: because of the bond weakness, a certain number of electrons is free to move and occupy the conduction

band, when the temperature is over 0 K and especially if an external electric field is applied.

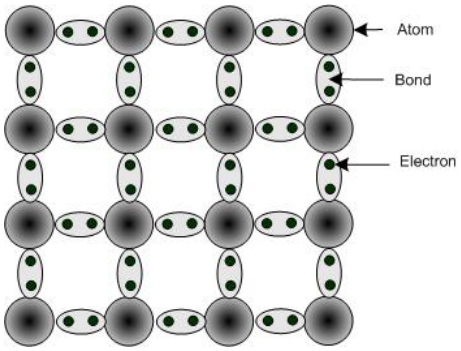

Figure 2.3: Atoms bonds representation for an intrinsic Silica lattice.

If we dope it with donor atoms, there would be more electrons than the ones bonded with the lattice, so the charge excess will populate the donor level (E_d in Figure 2.1) near the CB and will increase the semiconductor conductivity. Analogously, if we dope it with acceptor atoms, there would be a surplus of holes near the VB (E_a in Figure 2.1), and this will again increase the conductivity.

It is possible to dope a semiconductor either with acceptor atoms and with donor atoms, but obviously the holes generated by the former would be conpensated by the electrons of the latter, so the actual doping would be the greater one. If $p > n$ we have a *p-doped* semiconducor, with N_A = number of complexive acceptor atoms = p, otherwise the semiconductor is termed *n-doped* one, with N_D = number of donor atoms = n.

Given the semiconductor features, such as E_g, its temperature and the doping type and value, it is possible to calculate the number of the remaining holes or electrons.

Because of the great number of electrons and holes and the complexity of their dynamics inside the lattice, the physical properties of a semiconductor have to be determined with a statistical approach. We consider the Fermi-Dirac function $f_D(E)$, that gives the probability for a state of energy E to be occupied by one electron:

$$f_D(E) = \frac{1}{1 + \exp\left\{\frac{E - E_f}{kT}\right\}}, \tag{2.3}$$

where E_f is the energy of the Fermi level, that descriminates whether the CB or VB is occupied: notice that at $T = 0$ K all the states beyond the Fermi level are occupied. Let's call N_V and N_C the actual densities of acceptors and donors in the valence and conduction

band, respectively. We can put them in relation obviously with the doping density p or n, and with the Fermi level by the following equations:

$$n = N_C \exp\left\{-\frac{E_C - E_f}{kT}\right\}, \tag{2.4}$$

$$p = N_V \exp\left\{-\frac{E_f - E_V}{kT}\right\}. \tag{2.5}$$

Applying these in $n_i^2 = np$, we find an important identity, namely:

$$n_i^2 = N_C N_V \exp\left\{-\frac{E_V - E_C}{kT}\right\} = N_C N_V \exp\left\{-\frac{E_g}{kT}\right\} \tag{2.6}$$

which renders the equilibrium relation between the electrons and holes generation and recombination inside the lattice. As the n_i density is a pre-fixed quantity, every modification of the number of carriers inside the CB is balanced by an equal modification of the carriers in the VB, and vice versa.

The Fermi level is strictly dependant to the doping of the semiconductor, indeed the larger the p-doping (or the n-doping), the nearer is the Fermi level to the VB (or the CB), and this increases the probability to find acceptors (or donors) in there. In other terms, if the semiconductor is intrinsic, we can approximate $n \simeq p$ and the intrinsic Fermi level $E_f = E_i$ is right in the middle of the bandgap, $|E_c - E_i| \simeq |E_i - E_v|$, as according to Figure 2.4. If the semiconductor is p-doped, then $|E_c - E_f| \gg |E_f - E_v|$, otherwise, in a n-doped one, $|E_c - E_f| \ll |E_f - E_v|$.

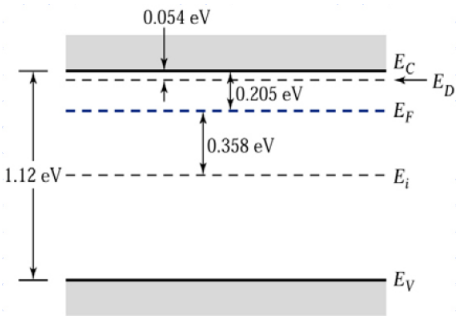

Figure 2.4: The Fermi level distribution in a n-doped Silica lattice, with $N_D = 10^{16}\ cm^{-3}$.

2.2.1 The drift current

We previously observed that if a semiconductor is exposed to an electric field, a weak electron movement could be noticed even if it is intrinsic. In a doped semiconductor the

current is more easily detectable, because the applied field drives not only the intrinsic charge, that spontaneusly passes from the VB to CB, but also the one added with the doping. This moving of charges (both electrons and holes) gives origin to the *drift current density* J_{drift}, that is proportional to the charge mobility, namely

$$\mu_n = \frac{-q\tau_{cn}}{m_n^*} \qquad \text{electron mobility,} \tag{2.7}$$

$$\mu_p = \frac{-q\tau_{cp}}{m_p^*} \qquad \text{hole mobility,} \tag{2.8}$$

where τ_c is the average time between two collisions, while m^* is the effective mass. With these we can now define the drift velocity:

$$V_{d,n} = -\mu_n E \qquad \text{for the electrons,} \tag{2.9}$$

$$V_{d,p} = \mu_p E \qquad \text{for the holes,} \tag{2.10}$$

and the drift current density for electrons and holes, respectively:

$$J_n = \sum_i -qV_{d,n} = nq\mu_n E, \tag{2.11}$$

$$J_p = \sum_i qV_{d,p} = pq\mu_p E. \tag{2.12}$$

the drift current density is defined as the average of the two, i.e.:

$$J_{drift} = q(p\mu_p + n\mu_n)E = \sigma E \tag{2.13}$$

where σ is the conducibility of the material. Once again eq. (2.13) points out that doping the semiconductor, either p or n, means increase its conductivity.

2.2.2 The diffusion current

Another type of current that is present inside a doped semiconductor, is the *diffusion current*. This current is originated by the simple unbalancement caused by the doping: as a matter of fact, if just one side of the semiconductor is doped, or both the two sides are doped in the opposite way, there will be a charge concentration gradient $dn/dx \neq 0$ or $dp/dx \neq 0$ that will cause the charges to diffuse through the whole semiconductor. If the charge distribution

is not constant along one of the axis of the semiconductor, here generically x, there would be a diffusion current density that can be written as:

$$J_n = qD_n \frac{dn}{dx} \qquad \text{for the electrons,} \tag{2.14}$$

$$J_p = -qD_p \frac{dp}{dx} \qquad \text{for the holes,} \tag{2.15}$$

where $D_{n,p}$ the *diffusivity coefficient*, is given by the Einstein's relations with the mobility:

$$D_n = \frac{kT}{q}\mu_n, \tag{2.16}$$

$$D_p = \frac{kT}{q}\mu_p. \tag{2.17}$$

As done for the drift current, we can sum the two contributions to the diffusion current density and find:

$$J_{diff} = q\left(-D_p \frac{dp}{dx} + D_n \frac{dn}{dx}\right) \tag{2.18}$$

that is, with eq. (2.13), one the most important equations of the semiconductors physics.

2.2.3 The pn homojunction

If we dope two pieces of a semiconductor, one p-type and the other n-type, and put them nearby, we will obtain a pn junction; in this way the consequent charge gradient will create a diffusion current from the p-side to the n-side. The electrons moving will induce an inverse and opposite electric field, thus another current, the drift one, will flow as showed in Figure 2.5. The electrons injected in the p region, and the holes injected in the n one will soon recombine with the dopers: once the system reaches the steady state, a *Spatial Charge Region* (SCR) appears, in which there is not free charge and the electric field is constant.

If we examine the band diagram of the whole junction with zero-bias applied, as depicted in Figure 2.6, we notice that since the Fermi level must stay constant, the other levels namely E_V and E_C change their positions and form a three-region scheme:

- the p-type region, where the hole doping has induced a low-energy Fermi level and as a result the CB is more energetic than the one in the n-type one;
- the SCR that has been depleted from free charge and represents a transition region for the electric field;

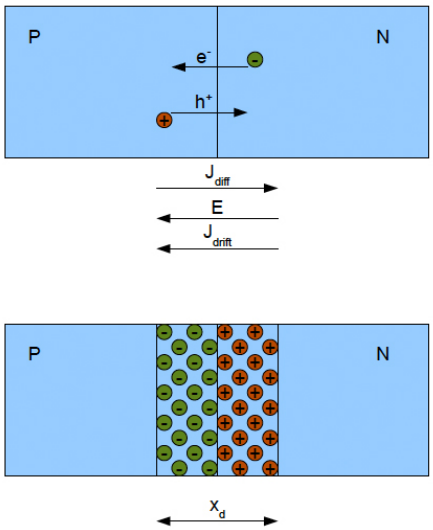

Figure 2.5: (Up) the diffusion and drift current after the creation of a pn junction, and (down) the SCR at steady state.

- the n-type region where both the CB and the VB are less energetic than the p-type ones.

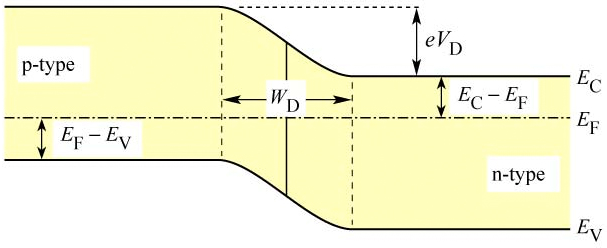

Figure 2.6: The energy levels of the bands diagram for a simple pn junction, with no bias applied. (Adapted from [4].)

Knowing the density of donors and acceptors contained inside the lattice, it is possible to evaluate the electric field profile, and so the potential inside the junction. We start from the two basilar equations:

$$\frac{dD}{dx} = \rho, \tag{2.19}$$

$$D = \epsilon E, \tag{2.20}$$

where D is the modulus of the electric displacement field, ρ the charge density and ϵ the

medium dielectric constant. These equations, combined, give:

$$\frac{dE}{dx} = \frac{\rho}{\epsilon}. \tag{2.21}$$

The last equation can be solved considering that for potential V the following identity holds:

$$\frac{dV}{dx} = -E \tag{2.22}$$

and eventually we arrive to the Poisson's equation, that combines the potential to the electric field as:

$$\frac{d^2V}{dx^2} = -\frac{\rho}{E}. \tag{2.23}$$

If we solve this, through the Gauss equation (2.21), both for the p and the n charge distribution, we find the electric field profiles in the two regions, namely:

$$E_p(x) = -\frac{qN_A}{\epsilon}(x - x_p) \qquad \text{for the field at the p-side,} \tag{2.24}$$

$$E_n(x) = \frac{qN_D}{\epsilon}(x - x_n) \qquad \text{for the field at the n-side,} \tag{2.25}$$

where x_n and x_p are the limits of the SCR at the p and n-side respectively. Assuming the continuity of the electric field at $x = 0$, we find the charge balancing relation

$$N_D x_n = N_A x_p. \tag{2.26}$$

From eqs. (2.24) and (2.25) we notice that, as shown in Figure 2.7, a potential barrier is created from the n-side to the p-side of the junction, so at steady state any flux of free electrons is forbidden. If we apply a forward bias to the junction, this potential barrier will low down, as represented in Figure 2.8, and the injected electrons will flow through the SCR, combining with the holes in the other side. This dynamics is the physical principle that stands behind a diode operation: when the diode is not biased, it presents an intrinsic potential barrier that can be lowered or increased whether a forward or reverse voltage is applied. In the first case the current can flow through the device, while in the second it can not.

2.2.4 The heterojunction

Even though a forward-biased diode may emit light too, it is inefficient because of the low concentration of free electrons in the SCR, hence we need to find another way to enhance

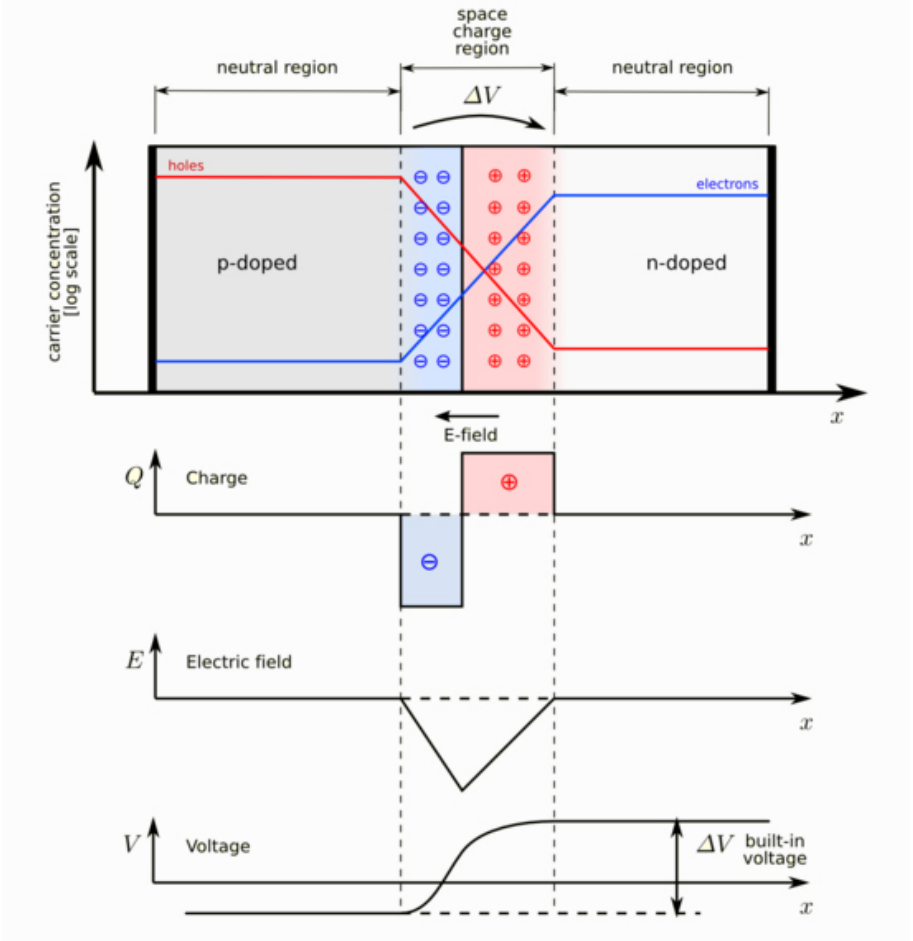

Figure 2.7: A pn junction with the related distribution of charge, electric field and potential: if no external bias is applied, the junction presents an intrinsic potential difference ΔV.

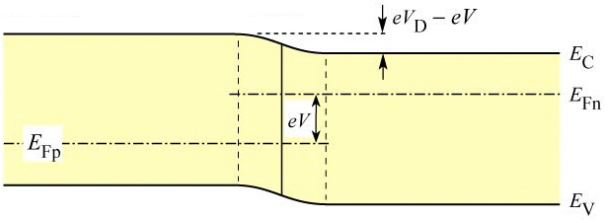

Figure 2.8: The pn homojunction bands distribution when a forward bias is applied. From [4]

this concentration in order to obtain a more rapid and likely radiative recombination. A way to achieve this is the creation of a heterojunction.

A heterojunction is a junction made up of two dissimilar semiconductors, having different

bandgaps, dielectric permettivities and electron affinities $q\chi$, as shown in Figure 2.9 (a). The electron affinity is the energy required to remove an electron from the conduction band to the vacuum level [3].

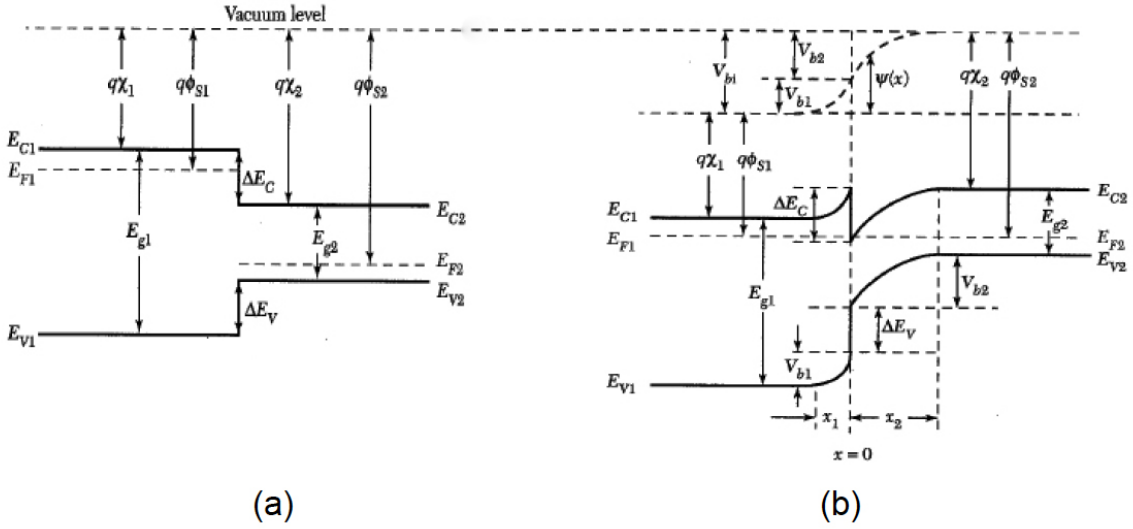

Figure 2.9: Energy band diagram for a heterojunction, (a) for the two isolated semiconductors, (b) at thermal equilibrium. (Image adapted from [3].)

Because of the different energy gaps, we notice that, if $\Delta E_g = E_{g1} - E_{g2}$, we have

$$\Delta E_C = q(\chi_2 - \chi_1) \tag{2.27}$$

and

$$\Delta E_V = \Delta E_g - \Delta E_C. \tag{2.28}$$

Figure 2.9 (b) shows that the complexive potential barrier is given by two contributions, $V_{bt} = V_{b1} + V_{b2}$ and each electrostatic potential can be derived from the Poisson's equation assuming the continuity of the carriers flux at the interface, obtaining:

$$V_{b1} = \frac{\epsilon_2 N_2 (V_{bi} - V)}{\epsilon_1 N_1 + \epsilon_2 N_2}, \tag{2.29}$$

$$V_{b2} = \frac{\epsilon_1 N_1 (V_{bi} - V)}{\epsilon_1 N_1 + \epsilon_2 N_2}, \tag{2.30}$$

where $N_{1,2}$ are the doping concentration for the two semiconductors, V_{bi} is the built-in potential and V is the applied bias.

When the thermal equilibrium is reached in the heterojunction, the final band diagram results as in Figure 2.9 (b). We have already observed that as regards the pn junction, it is important to keep constant the Fermi level in the final band diagram through the whole junction and the vacuum level must be parallel to the bands. With these requirements both the VB and the CB bends, and, moreover, the CB reaches a minimum of energy in which injected electrons could be trapped. This is the key feature of the whole heterojunction structure, that, as we will soon see, allows a high density of electrons in a region, that is called *quantum well*, which induces a great number of radiative recombinations.

2.3 The radiative and non-radiative recombination

As explained above, if a decay of an electron from the CB to the VB occurs in a direct-gap semiconductor, there is a very high probability to give origin to an energy release, in the form of light. Here we will better analyze both the case of a simple radiative recombination and some cases of non-radiative recombinations, together with the reasons why they occur.

A good light emitting device must evidently give a greater number of radiative recombinations than nonradiative ones, thus we define the quantum efficiency of such a device as the ratio between the electron decays that generate photons and the ones that can not.

Even though the non-radiative decays are impossible to avoid, we can find some materials, costructing and growing techniques that can minimize them.

The first thing to analyze is how we can generate electron-hole couples that cause radiation emission through recombination: to generate a donor excess we can illuminate, inject current or hit the semiconductor with an electron beam. If we generate a number of Δn or Δp couples, the complexive number of holes and electrons becomes:

$$n = n_0 + \Delta n, \tag{2.31}$$

$$p = p_0 + \Delta p; \tag{2.32}$$

since the total number of recombinations is proportional to the number of both electrons and holes, we define the coefficient of recombination per unit of time as

$$R = -\frac{dn}{dt} = -\frac{dp}{dt} = Bnp, \tag{2.33}$$

where B is the *bimulecolar recombination coefficient*, which depends from the semiconductor.

At steady state a certain number of recombinations R_0 occurs, and it is balanced by a number of generations G even if the semiconductor is not stimulated. If we apply, for example, a photonic beam, the number of electron-holes couples increases, and an excess charge with a rate of R_{excess} recombinations is induced. Because of this, the complexive recombination rate would be

$$R = R_0 + R_{excess}. \tag{2.34}$$

If we analogously consider the rate of generation of electron-holes couples, then we have

$$\frac{dn(t)}{dt} = G - R = (G_0 + G_{excess}) - (R_0 + R_{excess}), \tag{2.35}$$

that can be solved in a certain condition, for example if at $t = 0$ the illumination of the sample is interrupted and so $G_{excess} = 0$ for $t > 0$. In these conditions we obtain

$$\Delta n(t) = \Delta n_0 e^{-B(n_0+p_0)t} = \Delta n_0 e^{-t/\tau}, \tag{2.36}$$

with $\Delta n_0 = \Delta n(t = 0)$ and τ defined as the recombination time:

$$\tau = \frac{1}{B(n_0 + p_0)}; \tag{2.37}$$

this time constant is very important and can be explicited if the semiconductor is n-doped or p-doped, as:

$$\tau_n = \frac{1}{Bp_0} = \frac{1}{BN_A}, \tag{2.38}$$

$$\tau_p = \frac{1}{Bn_0} = \frac{1}{BN_D}. \tag{2.39}$$

These identities state that the more a semiconductor is doped, the more rapidly the concentration of electrons would decay due to the recombination processes.

If we hypotize a high level of excitation of the semiconductor, for example by a large current injection, the intrinsic generation and recombination rates can be neglected, thus arriving to

$$\frac{d\Delta n(t)}{dt} = G - R = -B\Delta n^2, \tag{2.40}$$

that is solved by the non-exponential term

$$\Delta n(t) = \frac{1}{Bt + \Delta n_0^{-1}}, \tag{2.41}$$

that implies a time-dependent decay constant $\tau(t)$, that is:

$$\tau(t) = t + \frac{1}{B\Delta n_0}. \tag{2.42}$$

The recombination rate can be modified with the doping of the semiconductor, but even if the induced one can be very fast, the intrinsic recombination speed is very low and this limits the use of LED devices, for example in the modulation of signals.

Concerning the recombination processes, we have already distinguished the radiative from non-radiative ones, in which the latter imply a release of energy in the form of thermal energy. Among the causes that lead to a non-radiative recombination, the most likely ones are the recombination into deep bound states and the Auger recombination, both reported in Figure 2.10 (a) and (b).

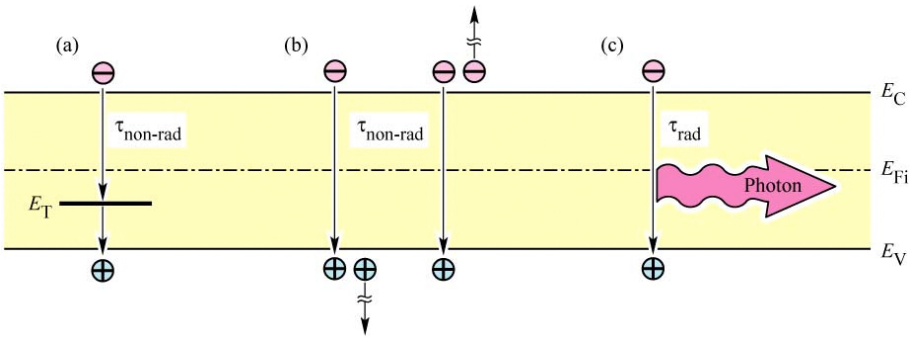

Figure 2.10: Energy band diagram for a semiconductor, representing (a) a non-radiative recombination into deep bound states, (b) an example of Auger recombination, (c) a radiative recombination, from [4].

2.3.1 Recombination into deep bound states

If we want a photon with energy $E = \nu h$ to be released, we need to obtain a decay of an electron from an equal energy gap. In decaying from the CB to the VB, the electron is possibly trapped by an intermediate state, called *deep bound state*, that prevents it to release the desired quantity of energy, and so giving origin to a non-radiative recombination.

These intermediate energy levels, that are also called *trap levels* or *luminescence killers*, are caused by imperfections or impurities inside the semiconductor lattice.

The medium lifetime of the electrons inside the trap levels is obtained with the equation:

$$\tau_n = \frac{n_0 + p_0 + 2n_i \cosh \frac{E_{int} - Ei}{kT}}{n_0 + p_0} \tau_0 \tag{2.43}$$

that points out the strict dependence from the temperature. If the temperature arises, the τ_n time coefficient drops down so the non-radiative recombination is more likely to happen: this is one of the main reasons why the LED efficacy drops at high temperatures.

In the last years the better techniques in producing semiconductors for optoelectronics devices have brought to a substantial reduction of both impurities and lattice imperfections, so the non-radiative recombination due to trap levels is much less frequent in actual devices than the ones of the first LEDs .

2.3.2 Auger recombination

As shown in Figure 2.10 (b), the Auger effect is a process in which both electrons or holes can be promoted or decay to other energy levels, different from the wanted one.

The Auger recombination rate, both for the holes and for the electrons, is defined as:

$$R_{auger,p} = C_p n p^2, \tag{2.44}$$

$$R_{auger,n} = C_n p n^2, \tag{2.45}$$

and, if a high excitation level is present, we approximate $n = p$, thus

$$R_{auger} = (C_n + C_p) n^3 = C n^3 \tag{2.46}$$

because of the low value of the Auger coefficient $C \simeq 10^{-31} \sim 10^{-28}\ cm^6/s$, we notice that a very high concentration of electrons or holes in the semiconductor is required for the Auger recombination to be evident.

Thus a way to mitigate this effect is to build devices in which the recombination region is wider, and so that the term n^3 is lower.

2.3.3 Recombination at surfaces

Since the more regular is the lattice the more probable is the radiative recombination, along its surfaces a strong perturbation of the lattice is present thus nonradiative events are more likely to happen there. The band diagrams of the atoms at the edges of the semiconductor presents strong modifications due to the lack of neighboring atoms, and this modifications include the addition of electronic states within the forbidden gap of the semiconductor, as depicted in Figure 2.11 (b).

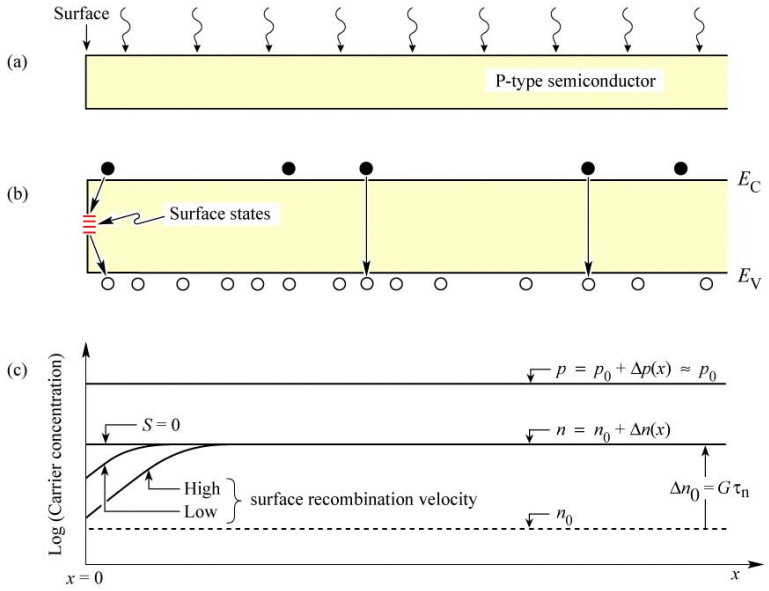

Figure 2.11: (a) Illuminated p-type semiconductor, (b) band diagram, including the nonradiative energetic states on the semiconductor surface, and (c) minority and majority carrier concentration near the surface assuming uniform carrier generation due to illumination. The excess carrier concentrations are Δn and Δp. (Figure taken from [4].)

An evaluation of the carrier concentration at the surface is done considering the continuity equation in the case of a p-doped semiconductor under illumination condition, thus considering a constant carrier generation G:

$$\frac{d\Delta n}{dt} = G - R + \frac{1}{q}\frac{dJ_n}{dx}, \tag{2.47}$$

that takes on account the diffusion current of electron towards the surface J_n, given by

$$J_n = qD_n\frac{d\Delta n(x,t)}{dx}; \tag{2.48}$$

considering the latter, eq. (2.47) becomes

$$\frac{d\Delta n(x,t)}{dt} = G - \frac{\Delta n(x,t)}{\tau_n} + D_n\frac{d^2\Delta n(x,t)}{dx^2}. \tag{2.49}$$

At the surface ($x = 0$) the following recombination identity holds:

$$qD_n\frac{d\Delta n(0,t)}{dt} = qS\Delta n(0,t) \tag{2.50}$$

where S is the surface recombination velocity, and depends from the considered semiconductor. Considering eq. (2.50), the (2.49) is finally solved by the following carrier concentration:

$$n(x) = n_0 + \Delta n(x) = n_0 + \Delta n_\infty \left[1 - \frac{\tau_n S e^{-x/L_n}}{L_n + \tau_n S} \right] \tag{2.51}$$

where Δn_∞ is the steady state carrier density and L_n is the carrier recombination length. This expression is represented in Figure 2.11 (c), where is evident the exponential decay of the carrier concentration nearby the surface.

2.3.4 The steady-state rate equation

Under steady-state conditions, we express the electron density inside the active region with the following differential equation:

$$\frac{dn}{dt} = \frac{J}{qd} - (Bnp + AN_T n) = 0, \tag{2.52}$$

where J is the complexive injected current density, d the thickness of the active layer, B and A the radiative and nonradiative recombination coefficients respectively, and N_T is density of defects that are often responsible for the nonradiative recombinations. Under high injection conditions, the following holds:

$$n \simeq p \gg N_A,\ N_D, \tag{2.53}$$

so we can simplify (2.52) as

$$Bn^2 + AN_T n - \frac{J}{qd} = 0. \tag{2.54}$$

Once the basilar differential equation is determined, we impose two hypotesis:

- the radiative recombination is major than the nonradiative one, so having $AN_T n \ll Nn^2$ we arrive to
$$Bn^2 \simeq \frac{J}{qd}; \tag{2.55}$$
- on the other hand, if the nonradiative recombination dominates over the radiative, i.e. $AN_T n \gg Bn^2$, we have
$$AN_T n = \frac{J}{qd}. \tag{2.56}$$

As the light output L is obviously proportional to the intensity of the radiative processes, $L = Bn^2$, we will see in chapter 7 how is possible to retrieve the prevalence of one or the other process from the light output versus current (L-I) measurements.

Once the recombination dynamics has been explained, now we introduce the concept of *internal quantum efficiency*, that is one of the most important parameters that evaluate the efficiency of a LED device.

As we saw, not all the recombinations inside the active region are radiative, because of this the internal quantum efficiency is defined as the ratio between the emitted photons and the total number of recombinations. If we denote with τ_r the time coefficient of the radiative recombinations, and τ_{nr} the one of the nonradiative, the total recombination probability reads as:

$$\frac{1}{\tau} = \frac{1}{\tau_r} + \frac{1}{\tau_{nr}}, \tag{2.57}$$

while the internal quantum efficiency is given by:

$$\eta_r = \frac{\frac{1}{\tau_r}}{\frac{1}{\tau_r} + \frac{1}{\tau_{nr}}} = \frac{\tau_{nr}}{\tau_{nr} + \tau_r}. \tag{2.58}$$

2.4 Quantum well structure

If we want to radically increase the total number of recombinations, we should find a way to trap a larger number of electron-hole couples inside the active region of the device, and this can be obtained using more than one heterostructure.

In order to fully understand the dynamics of electrons nearby a quantum well, or generally their behaviour inside a heterostructure so thin that its length is comparable with the wavelength, we have to consider the basilar principles of quantum mechanics, as the De Broglie's Hypotesis, the wave function and the Shrödinger's equation.

2.4.1 The wave function

The De Broglie's Hypotesis is the basis of the whole quantum mechanics: if a particle has a certain momentum, then it has also a certain wavelength; thus to a kinetic energy corresponds always an ondulating phenomenon. If we write the momentum $p = \hbar k$, then [2]

$$E_{kin} = \frac{p^2}{2m} = \frac{(\hbar k)^2}{2m}. \tag{2.59}$$

[2] with k the wave number so that $k = 2\pi/\lambda$ and $\hbar = h/2\pi$

This hypotesis was demonstrated by the Davisson and Germer experiment, in which they assessed the analogy between the wavelength of an X-radiation with a certain energy and the one of an electron with the same energy.

If an electron has an ondulatory motion, it can be described by the wave function

$$\Psi(x,t) = \Psi_0 e^{i(kx-\omega t)} \tag{2.60}$$

that can be applied to describe an electron movement through some properties, such as:

1. Supposing the electrons movement inside the active region to be monodimensional, we can just consider the variability of the function along the x coordinate, so

$$\Psi(x,y,z,t) \simeq \Psi(x,t). \tag{2.61}$$

2. The quantity

$$\Psi^*(x,t)\Psi(x,t) \tag{2.62}$$

is a density probability function, so we can express the probability of find the electron at time t in a certain spatial element dx as

$$\Psi^*(x,t)\Psi(x,t)dx, \tag{2.63}$$

and the following normalization holds:

$$\int_{-\infty}^{+\infty} \Psi^*(x,t)\Psi(x,t)dx = 1. \tag{2.64}$$

3. Both $\Psi(x,t)$ and its derivative $d\Psi(x,t)/dx$ are continous functions in isotropic media.

4. The conversion from the classical mechanics operators to the quantum ones is possible. For example if we want to find the momentum or the energy of an electron once its wave function is known, then the following can be used:

$$p\Psi = \frac{h}{i}\frac{d\Psi}{dx}, \tag{2.65}$$

$$E\Psi = -\frac{h}{i}\frac{d\Psi}{dx}. \tag{2.66}$$

If we apply the energy conservation to the operators above, we obtain the Schrödinger equation:

$$-\frac{\hbar^2}{2m}\frac{d^2\Psi(x,t)}{dx^2} + U(x)\Psi(x,t) = -\frac{\hbar}{i}\frac{d\Psi(x,t)}{dt} \tag{2.67}$$

where the equation $E_{tot} = E_{kin} + U(x)$ has been applied to the operators, with $U(x)$ the Potential Energy. This equation is very difficult to solve. If we want to apply it to the electron distribution inside a heterostructure, we can consider the simplified time-invariant version:

$$-\frac{\hbar^2}{2m}\frac{d^2\Psi(x)}{dx^2} + U(x)\Psi(x) = E\Psi(x). \tag{2.68}$$

Noticing that, while the classical mechanics is not only much simpler, but also more deterministic than the quantum one, we should point out why it is necessary to use the latter. If the device we want to study has dimensions much larger than the wavelength, then we can admit the quantic effects to be neglegible and then its dynamics can be studied in the classical mechanics framework, for example determining the quantity of charge inside it in a deterministic way with the Poisson equation. Conversely if the device structure is as wide as the wavelength, as it is for our case, we cannot precisely determine how many electrons are present, and thus we have to use the wave function $\Psi(x,t)$.

2.4.2 The infinite potential well

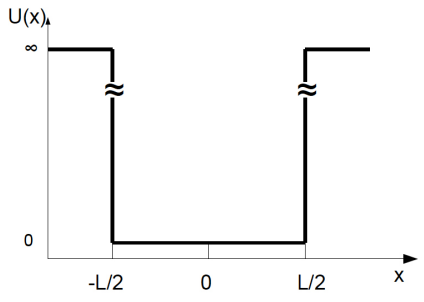

Figure 2.12: An infinite potential quantum well energy representation.

As shown in Figure 2.12, we suppose to create a quantum well where the upper state has infinite potential energy, so once an electron falls in there it never returns on top and the probability to find an electron outside the well is zero:

$$\Psi^*(x,t)\Psi(x,t) \neq 0 \;\Leftrightarrow\; x \in \left[\frac{-L}{2}, \frac{L}{2}\right]. \tag{2.69}$$

Inside this quantum well the electrons occupy different states of energy, and it is found that multiples of half of the De Broglie's wavelength can be matched to the width of the quantum

well, so

$$\frac{1}{2}\lambda(n+1) = L \tag{2.70}$$

$$E = \frac{p^2}{2m} = \frac{1}{2m}\left(\frac{2\pi\hbar}{\lambda}\right)^2 \tag{2.71}$$

$$\Rightarrow\ E_n = \frac{\hbar^2}{2m}\left[\frac{(n+1)\pi}{L}\right]^2 \qquad (n = 0, 1, 2, \ldots) \tag{2.72}$$

where n is the quantum number: a wave function $\Psi_n(x,t)$ can be associated to each energy level E_n, as depicted in Figure 2.13.

Actually we do not have infinite quantum wells in our heterojunction, but we can still

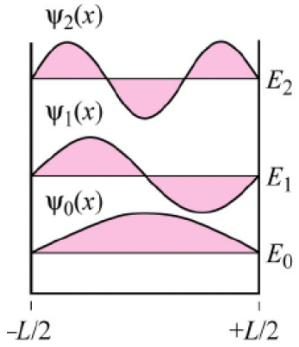

Figure 2.13: The wave vector distribution for an infinite quantum well, in the first three orders, from [2].

consider this wave function as a valid distribution. Nonetheless, since the energy gap is finite, there is the possibility for an electron to stay outside the well, so that the wave function would be modified near the band edges.

The quantum well, as seen in this section, allows the creation of a region with a high concentration of electron-hole couples. This can be created with a double heterojunction, as shown in Figure 2.14, that can be moreover repeated inside the active region of a device, in order to more increase the probability of radiative emission, forming a *Multi Quantum Well* (MQW) structure.

2.5 Materials used for LEDs lighting

As shown in Figure 2.15, if we want a radiation peaked at a certain wavelength, we need to use materials with a certain E_g and so only a few combinations of compound semiconductors

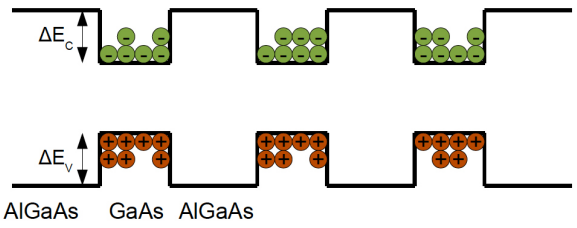

Figure 2.14: The structure of a MQW formed by layers of AlGaAs and GaAs

are possible. Since we also need to built MQW structures, lattice-matched materials must be employed so that the whole structure results to be coherent and without imperfections. We will see here that the materials used for the SSL are systems based in Phosphide and Nitrogen.

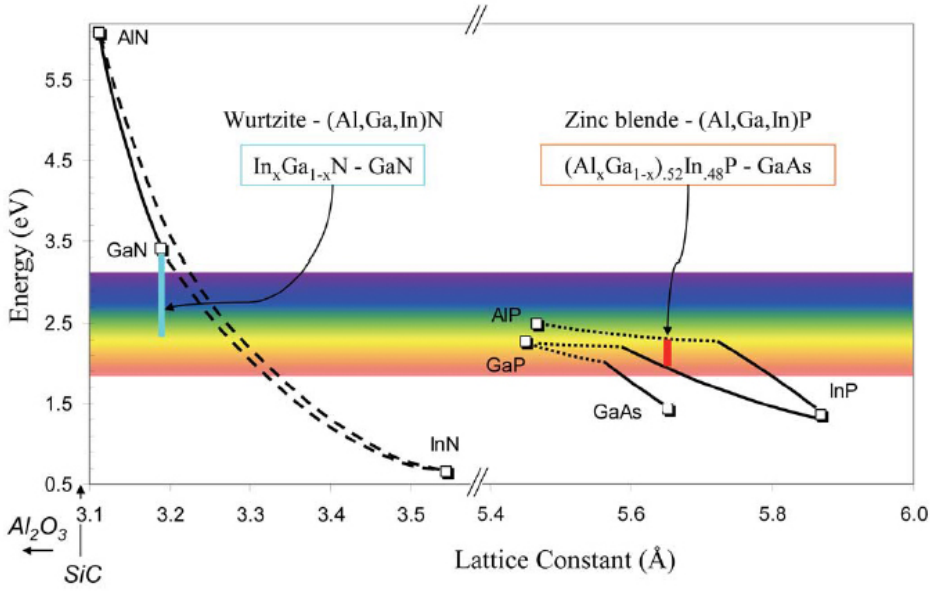

Figure 2.15: Energy bandgap versus lattice constant for wurtzite III-Nitride and zincblende III-Phosphide semiconductor alloy systems employing Al, In, and Ga. Solid lines indicate direct bandgap alloys, dotted lines indicate indirect bandgap alloys, and dashed lines are estimates. (From [5].)

As concerns the material system based on the III-Phosphide group, the lower-bandgap part of the MQW could be occupied by the $(Al_x, Ga_{1-x})_{1-y}In_yP$ alloy, that for $y = 0.48$ is lattice-matched to GaAs, while the bandgap is easily tuneable by varying the molar fraction

x. For example, placing no Aluminium gives $x = 0$, so that an InGaP compound with emission at $\lambda \sim 650\ nm$ (deep red) is obtained, while by setting $x = 0.53$ the emission will be at $\lambda \sim 560\ nm$ (yellow-green).

For the system based in III-Nitrogen, the alloy of interest with radiative decay in the whole visible spectrum is $In_xGa_{1-x}N$, where we have for $x = 0$ (GaN) $\lambda \sim 365\ nm$ with UV-A radiation, and for $x = 1$ $\lambda \sim 1800\ nm$, infrared.
The spectral range achievable by this type of composition is in theory very wide, but construction issues constrain its realization: the principal problem is the absence of a native bulk-substrate for the InGaN alloy, so the growth of alloys with a high concentration of InN leads to non-homogeneity and eventually to the breakdown of the cristallographic structure. Because of this, only low mole fraction of InN could be achieved maintainig a relatively high quantum internal efficiency, so high performing GaN-based LEDs are available from $\lambda = 365\ nm$ (UV-A) to $\lambda = 550\ nm$ (deep green). In Figure 2.16 are summarized the most used alloys together with their energy bandgap and radiation energy.

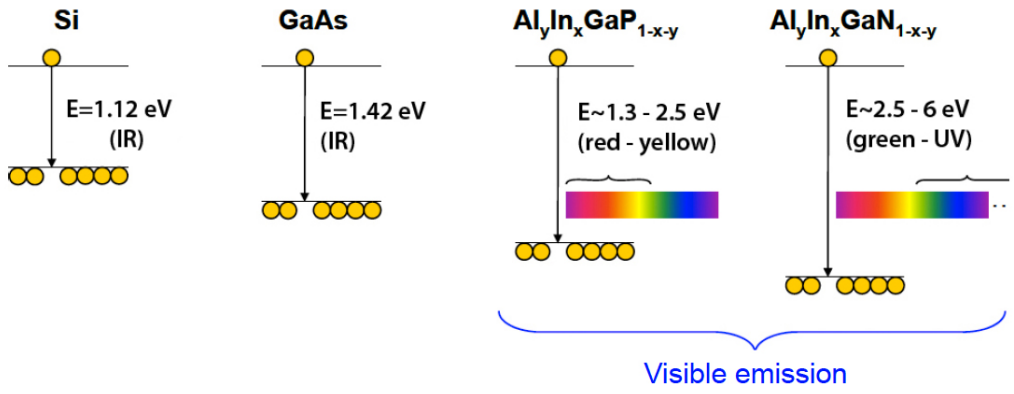

Figure 2.16: The emission wavelengths ranges of the considered semiconductors, adapted from [2].

CHAPTER 3

Principles and design of white LEDs

In this chapter the optical and electrical characteristics of a common LED chip will be analyzed, underlining the problems that must be overcome to increase the total efficiency and to improve the thermal behaviour. After this, a brief classification of the most diffused chip configurations will follow, together with the explanation of how they work: once a detailed description of a LED has been provided, it will be much easier to understand the electrical and thermal principles. In the last section we will focus on the central issue of the whole tractation, that is how a white LED works, in particular its differences from common LEDs will be explained and its main problems, especially concerning the efficiency management, will be discussed.

3.1 The electric properties of LEDs

3.1.1 The I-V relation

As explained in details in chapter 2, a LED device is essentially a diode, thus it has its same electric characterictics. Because of this, we can recall the I-V relation for a diode:

$$I = I_S \left(e^{\frac{qV}{kT}} - 1 \right) \tag{3.1}$$

with I_S the saturation current, that can be expressed as:

$$I_S = qA\left(\sqrt{\frac{D_p}{\tau_p}}\frac{n_i^2}{N_D} + \sqrt{\frac{D_n}{\tau_n}}\frac{n_i^2}{N_A}\right), \tag{3.2}$$

where $D_{p,n}$ is the diffusion coefficient of holes and electrons, and $\tau_{p,n}$ is their average recombination time.

If the applied voltage is $V \gg kT/q$, then the diode is running saturation eq. (3.1) becomes

$$I = qA\left(\sqrt{\frac{D_p}{\tau_p}}N_A + \sqrt{\frac{D_n}{\tau_n}}N_D\right)e^{\frac{q(V-V_D)}{kT}}, \tag{3.3}$$

where the saturation current becomes prevalent, and the intrinsic junction potential is given by

$$V_D = \frac{KT}{q}ln\left(\frac{N_A N_D}{n_i^2}\right). \tag{3.4}$$

As already stated before and represented in figure 2.6, if the doping of the semiconductor is sufficiently high, then the Fermi level is much separated from the CB in the p-doped side and from the VB in the n-doped, so

$$E_C - E_F \ll E_g, \tag{3.5}$$

$$E_F - E_V \ll E_g, \tag{3.6}$$

and, from the band diagram we obtain the intrinsic junction voltage

$$V_{th} \simeq V_D \simeq \frac{E_g}{q} \tag{3.7}$$

that is also the threshold potential that an external applied voltage has to overcome in order to get the diode directly conductive. In Figure 3.1 is well reported this situation: once the applied voltage is greater than a pre-fixed value (V_{th}), the conductivity is exponentially enhanced. From the same figure we can also notice that V_{th} is strictly dependant from the semiconductor, i.e. the E_g value. Ideally, once the direct bias is $V > V_{th}$, the potential barrier of the diode is completely lowered and the pn junction becomes an ideal conductor. Because of the serial and parallel resistances, the I-V characteristic is not perfectly vertical, as happens in Figure 3.1 (e). Then the I-V relation must be corrected:

$$I - \frac{V - R_S I}{R_P} = I_S e^{\frac{q(V-R_S I)}{n_{ideal}kT}} \tag{3.8}$$

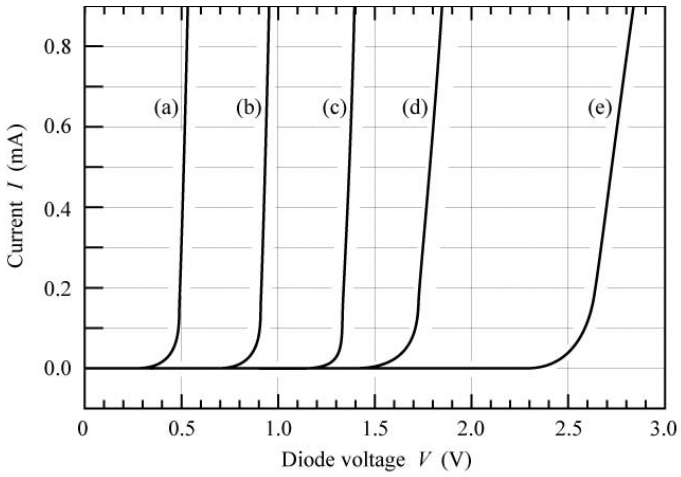

Figure 3.1: The I-V relation at $T = 295\ K$ for diodes composed by different materials: (a) Ge, (b) Si, (c) GaAs, (d) GaAsP, (e) GaInN. From [4].

where R_S is the serial resistance and R_P is the parallel one. The term n_{ideal} is a correction called *ideality factor* that is $n_{ideal} = 1$ only for an ideal diode, while in a real one it accounts for all the non-ideal phenomena that can occur, for example the recombination in the space charge region. Diodes containing one or more heterostructures present an ideal factor from 2 to 4.

3.1.2 The carrier escaping

The parasite resistance that characterizes the heterostructured semiconductors can be easily explained by the traps induced by the QWs. Because of them, the current is notably counteracted in the diffusion from the p-side to the n, as shown in Figure 3.2. The heterostructure is expressly designed in order to not let the electrons flow from one side to the other, because if they escape they do not contribute to the radiative recombination. In the following we will examine the reasons why they do not stay trapped inside the quantum well.

The number of escaping electrons is inversely proportional to the height of the energy edges that form the QW and directly proportional to the injected current: the first occurrence is called *carrier escape* and the second one the *carrier overflow*, and they both cause electrical inefficiencies in LEDs devices.

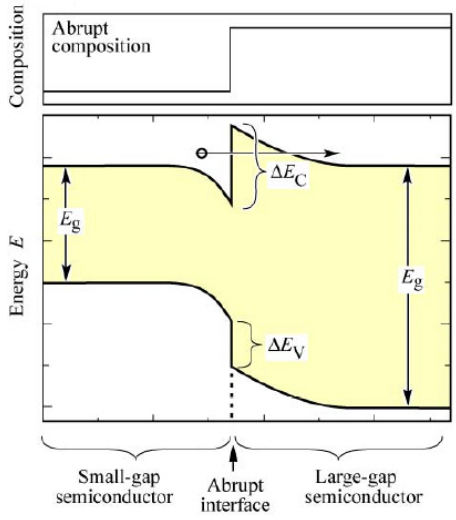

Figure 3.2: Band diagram for an abrupt n-type-n-type heterostructure: the trap created from an heretojunction gives a parasite resistance to the direct current flow. (From [4].)

The Carrier Escape is due to the presence of electrons in the higher part of the CB even in the lower-bandgap semiconductor, as the Fermi-Dirac function confirms. These electrons, that are the most energetic, are very likely to jump the energy barrier induced by the heterostructure and flow on the n-side, as represented in Figure 3.3.

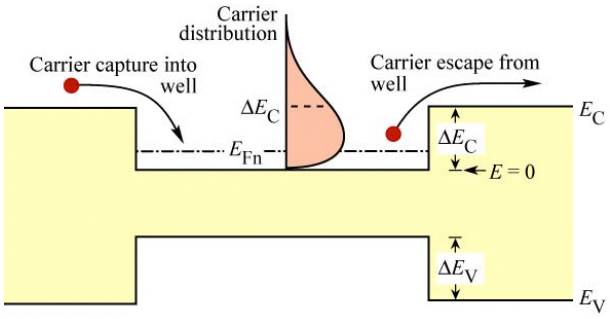

Figure 3.3: Carrier capture and escape in a double heterostructure. Also shown is the carrier distribution in the active layer. (Figure from [4].)

The Carrier overflow is due to an electron distribution with high energy even over the CB, according to the Fermi-Dirac distribution, but the number of these electrons can be in this case enhanced if the current injected is very high, so electrons can not be trapped inside the QW.

In order to prevent the effects given by these carrier escaping, we can design the band diagram of the device including a special layer, called the *Current Electron Blocking Layer* (EBL), that is able to block the escaping layers inside the QW structure, as can be seen in Figure 3.4.

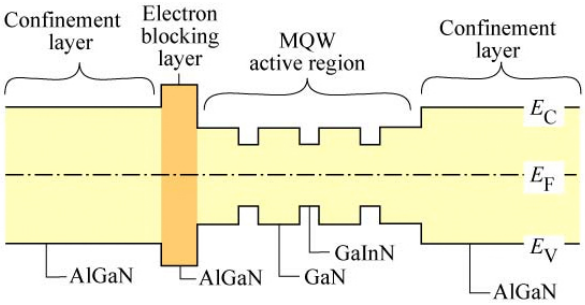

Figure 3.4: AlGaN current- blocking layer in an AlGaN/ GaN/GaInN multi quantum well structure, represented in a band diagram without doping, from [4]. This bandscheme also features a higher bandgap confinement layer, that can provide a greater number of trapped electrons and a lower escape probability.

3.2 The thermal model

As we will see in the efficiency extimation, the thermal management is one of the main issues concerning a LED device, and its improvement is one of the keys of a successful light source.

For what concerns this thesis work, the study of the thermal characteristics and behaviour for LEDs under stress conditions requires the construction of a valid thermal model in which we must base our consideration and evaluate our results. This model is represented in Figure 3.5 and deals with the thermal path that the heat has to follow. Each path can be represented with a *thermal resistance* that is not only peculiar for each device, but also vary with the disposition of one or more LEDs onto the Printed Circuit Board (PCB) and, obviously, with the applied thermal interfaces.

Each thermal resistance, expressed in K/W, consists in the resistance of a certain material to the thermal flux, as the electrical resistance opposes to the current. As shown in Figure 3.6, if $T_A > T_B$, there will be a thermal power flux from the point A to B, and as a consequence a temperature gradient $\Delta T = T_A - T_B$. The relation between the power transferred, P_{th}, the

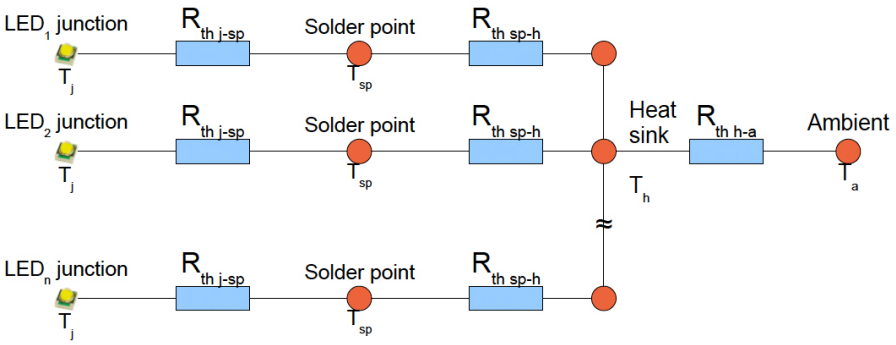

Figure 3.5: Thermal model used to represent the thermal path from the LED active region to the heatsink

thermal resistance R_{th} and temperature gradient is very similar to the Ohm's law:

$$\Delta T = P_{th} R_{th} \tag{3.9}$$

Using a measurement process that will be described in section 5.2, the complexive thermal

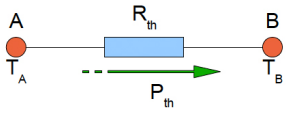

Figure 3.6: A simple scheme of the thermal flux between two point with different temperatures ($T_A > T_B$) and over a thermal resistance

resistance (from junction to ambient) can be calculated. This is necessary not only because the device working and its ageing are very dependant from the thermal resistance, but also because the thermal resistance from junction to solder point, that is provided by the LED producer, is pretty useless: as a matter of fact we cannot simply add the new thermal resistances in the path to ambient (i.e. the resistance introduced by the PCB, the thermal adhesive and the heatsink), because once we change one of them, even the thermal flux does.

3.3 The optical properties of LEDs

Some of the most attractive features of LEDs are their optical properties, and lots of efforts to enhance their optical efficiency have been done, especially in the last years. To this continous improvement contributes not only the increase of the Internal Quantum Efficiency,

but also many tricks that have been adopted in the design of both the chip and the epoxy lens in order to obtain a higher extraction of photons from the active region. In this section the optical behaviour of a LED is described, from the relation between the energy states and the output luminous power to the configuration of the light escaping cone. In addition to this further issues are considered, i.e. the reasons why there is the need to improve the LED package design in order to reach a better photon extraction from the active region to the free space.

3.3.1 The L-I relation

The relation between the luminous intensity and the injected current is strictly bond to the efficiency of the chip, in particular to the relation of the total emitted photons and the current effectively injected into the active region [21]. If we call generally η this efficiency, we find that the photon current is

$$I_{ph} = \eta \frac{I}{e} = \eta \frac{ndA}{\tau_r}, \tag{3.10}$$

where d is the width of the active region, A the diode area, n the number of injected electrons and τ_r is their average recombination time. The total optical power is then

$$P_{opt} = I_{ph} \hbar\omega = \eta \frac{\hbar\omega ndA}{\tau_r}. \tag{3.11}$$

In this relation the optical output power is proportional to the injected current, but it does not take on account the influence of the nonradiave decays or the carrier escaping, that can significally modify it. Actually the measured L-I relation is divided into three parts:

- for low current injection, the nonradiative processes can be prevalent over the radiative, so the lumious output is quadratic with the current;
- as the current rises the radiative processes prevale over the nonradiative, and the relation becomes linear;
- a further increase of the current renders a higher value of radiative decays but also a greater probability of carrier escaping, that leads the L-I curve to a sub-linear trend. Higher current levels saturate the decays number: this saturation is reflected by a pretty constant light output for very high currents. Obviously the carrier escaping strictly depends on the heterostructure and the number of quantum wells: as depicted

in Figure 3.7, a greater number of QW gives a lower carrier leakage and the sub-linear part of the curve is shifted onto higher current levels.

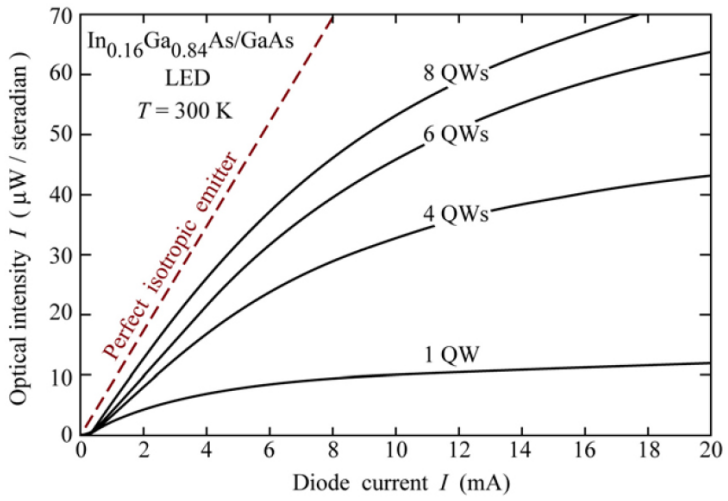

Figure 3.7: Optical intensity emitted by $In_{0.16}Ga_{0.84}As/GaAs$ LEDs with active regions consisting of one, four, six, and eight quantum wells and theoretical intensity of a perfect isotropic emitter (dashed line). (Figure taken form [4].)

As the presence of these regions is an immediate reflection of the internal efficiency properties of the LED chip, their moving during the device operation is a direct and simple signal of the internal changes of the chip, i.e. the increase of nonradiative centers. A detailed analysis will be conducted during the experimental results presentation.

3.3.2 The external quantum efficiency

If we want to evaluate the total efficiency of a LED , from the injection of current to the extraction of photons, three different contributions have to be considered:

- The *injection efficiency*, the ability to inject electron-hole couples to the SCR of the heterojunction before they recombine out of it, namely

$$\eta_{inj} = \left(1 + \frac{\mu_h N_A L_e}{\mu_e N_D L_h}\right)^{-1}, \tag{3.12}$$

where $L_{e,h}$ are the recombination lengths and $\mu_{e,h}$ the mobilities of electrons and holes.

- The *internal quantum efficiency*, that is the number of radiative recombinations (and so of photons emitted by the active region) versus the total number of recombinations:

$$\eta_{int} = \frac{\tau_{nr}}{\tau_r + \tau_{nr}} = \frac{P_{int}/h\nu}{I/q}, \tag{3.13}$$

  with P_{int} the optical power emitted by the active region and I the current injected in it;

- The *extraction efficiency* is the ratio between the photons that reach the free space outside the device to the number of photons emitted from the active region:

$$\eta_{extraction} = \frac{P/h\nu}{P_{int}/h\nu}, \tag{3.14}$$

  where P is the optical power emitted.

  This parameter is strictly dependant from the LED package design because the longer is the path they have to cross the higher is the probability that they stay trapped inside the device, absorbed by the metallization or by some impurities with a lower energy gap.

If we want to consider the whole optical efficiency, comprehensive of the number of injected electrons, we can use the *external quantum efficiency*, that is

$$\eta_{ext} = \eta_{int}\eta_{extraction} = \frac{P/h\nu}{I/q}. \tag{3.15}$$

3.3.3 The emission spectrum of a LED

Ideally, as the energy gap is defined for any semiconductor, and the relation $E_g = h\nu$ holds, each recombination and respective photon release should be accompained by a monochromatic radiation. We already saw why the distribution of electrons inside the CB and VB is not just determined by the energy gap but it follows the Fermi-Dirac function. In a real semiconductor there are electrons with larger energy decay than the energy gap, thus we expect a broader radiation spectrum. We already analized the parabolic distribution of the valence and conduction bands in respect to the momentum of electrons, so for the energy conservation we have

$$h\nu = E_g + \frac{\hbar^2 k^2}{2m_r^*}, \tag{3.16}$$

with $1/m_r^* = 1/m_e^* + 1/m_h^*$ is the *reduced mass*.

Among the continous of states thus found, there is only a certain number of allowed ones, given by the parabolic relation

$$\text{allowed states density} = \frac{1}{2\pi^2}\left(\frac{2m_r^*}{\hbar^2}\right)^{3/2}\sqrt{E-E_g} \tag{3.17}$$

while the electron energies are distributed with the Boltzmann function

$$f_B(E) = e^{-E/kT} \tag{3.18}$$

so the intensity of the emitted radiation is proportional to the (3.17) and (3.18) product:

$$I(E) \propto \sqrt{E-E_g}e^{-E/kT} \tag{3.19}$$

that is represented in Figure 3.8. This output spectrum seems to be very large but, for

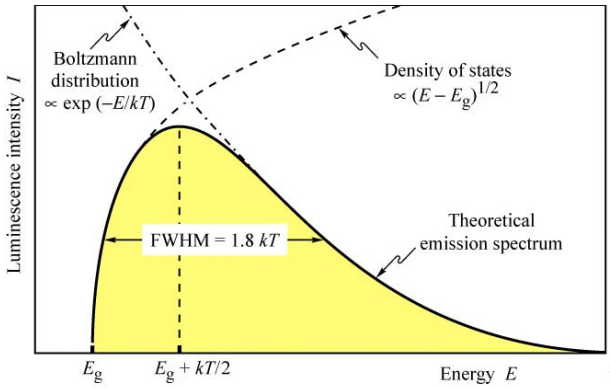

Figure 3.8: Theoretical emission spectrum of an LED. The full width at half maximum (FWHM) of the emission line is 1.8 kT. (From [4].)

example, in a GaAsP red LED the FWHM is just 24 nm, that is thinner than the single-color perception of the human eye.

If we increase the feed current the trend of the spectrum is characterized by a widening due to the occupation of the more energetic states, that leads to a greater number of high-energetic recombinations.

The dependence of the Boltzmann function with the temperature is also important and is remarkable onto the spectrum variation both when the device is put at different ambient temperatures and when its temperature rises under self-heating conditions. A higher temperature gives an increasing of the number of more energetic electrons over the CB, so the probability of the carrier escape arises: in these conditions the complexive radiation will be given by

the electrons that stay trapped inside the barriers, which present a lower energy gap and so the radiative processes will give origin to a lower-frequency photons. The whole resulting spectrum will suffer of a shift towards higher wavelenghts as the temperature increases.

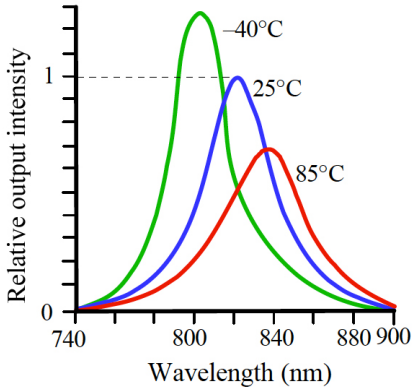

Figure 3.9: The relative spectrum emission of a red AlGaAs LED , normalized to the peak emission at $25\ ^{o}C$. (Adapted from [2].)

3.3.4 The escaping angle of light

In order to prevent the total internal reflection of the radiation inside the chip, an epoxy dome is often applied where the light has to be extracted, and because of this it is possible to estimate the escape angle, that gives origin to an escape cone, inside which light can succesfully irradiate in free space, and outside it is most likely trapped and then losed.

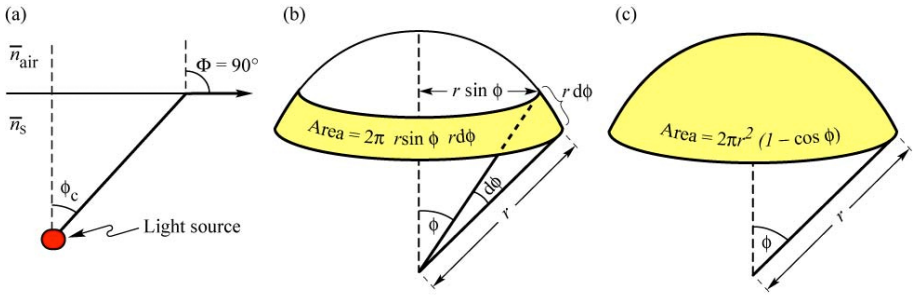

Figure 3.10: (a) Definition of the escape cone by the critical angle Φ_c . (b) Area element dA. (c) Area of calotte-shaped section of the sphere defined by radius r and angle Φ_c. (Figure taken from [4].)

If we evaluate, as in Figure 3.10, the surface area of the spherical escaping cone with

radius r and assuming that the light is emitted froma point-like source with power P_{source}, we obtain the relation:

$$P_{escape} = P_{source}\frac{2\pi r^2(1-\cos\Phi_c)}{4\pi r^2} = P_{source}\frac{1}{2}(1-\cos\Phi_c), \tag{3.20}$$

which is stricly dependant from the critical angle Φ_c:

$$\Phi_c = \frac{n_{air}}{n_s}, \tag{3.21}$$

where $n_{air} \simeq 1$ is the air refractive index, $n_s > 1$ is the semiconductor's. Expanding in eq. (3.20) the cosine into a power series and combining this with eq. (3.21), we arrive to

$$\frac{P_{escape}}{P_{source}} \simeq \frac{1}{4}\Phi_c^2 = \frac{1}{4}\frac{n_{air}^2}{n_s^2}. \tag{3.22}$$

Since the semiconductor's refrative index can be quite high ($n_s > 2.5$), the quantity in (3.22) can be significantly increased with the application of an epoxy dome with an interediate refractive index over the chip top surface: this leads to a rising of the critical angle, thus a greater light escaping is achieved.

In the next section we will examine the performance of the most diffused chip designs, and we will see how in their development a great importance is given to the quest for an optimal escaping of light.

3.4 The efficiency droop of InGaN LEDs

Since in this work we will manage LEDs based on the InGaN-GaN alloy, that, as we will see in the next sections, are the ones used in the white SSL, a deeper study of their efficiency behaviour is conducted.

Although nitride LEDs have demonstrated high external quantum efficiencies at low currents, high-power LEDs suffer of a great efficiency lowering at desired operating currents: this phenomenon called "efficiency droop" is not due to the simple heating, because it happens both in pulsed and in continous conditions, and it is found to be more stressed at longer wavelengths, but it is also present in the operating of near-UV's InGaN LEDs [6].

If we neglect the thermal causes, we can consider the non-radiative recombination as the principal mechanism, that can be due to carrier delocalization, defect-assisted tunneling of carriers out of the active region, Auger recombination or inefficient carrier injection. Even

though the effect has not been studied enough and a resolutive reason has not been found yet, some hypotesis have been advanced:

- Philips Lumileds has identified, during a study on their Luxeon green LED device [6], the Auger process as the predominat nonradiative mechanism leading to efficiency loss at high carrier densities. This supposition have been challenged because of the small

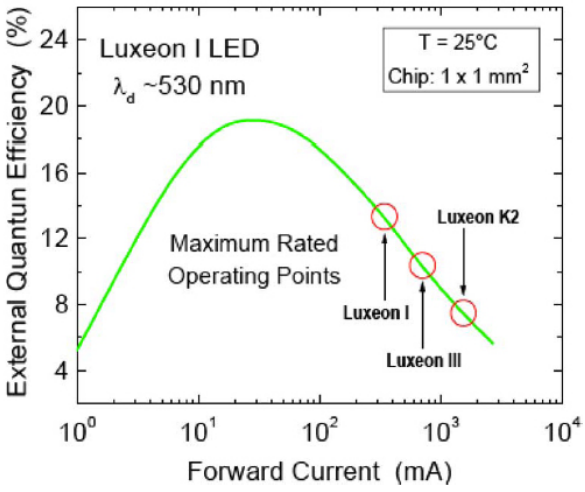

Figure 3.11: External quantum efficiency of commercial green LEDs (Philips Lumileds' Luxeon line) as a function of operating current. Maximum rated operating currents of three different Luxeon models are indicated. (From [6].)

  Auger coefficient of wide-bandgap semiconductors, and had been proposed a phonon-assisted and defect-assisted Auger recombination mechanism.

- A second hypotesis attributes the droop to limitations in the carrier transport and injection: in other words, there are some difficulties on the carrying of holes into the active region, in front of a electron leakage out of it, and this leads to a carrier recombination in the p-side of the junction, as depicted in Figure 3.12. These two phenomena put together are evidently the cause of a inefficient recombination inside the active region, but the cause-effect relation between them is not entirely clear. A group from the Rensselaer Polytechnic Institute (RPI) [6] has identified as a major contibutor to the inefficiency the polarization-induced electron leakage outside the active region. This effect could be mitigated introducing the EBL, that can reduce the efficiency droop of 18 % into AlInGaN blue LEDs , or improving the hole injection, for example developing

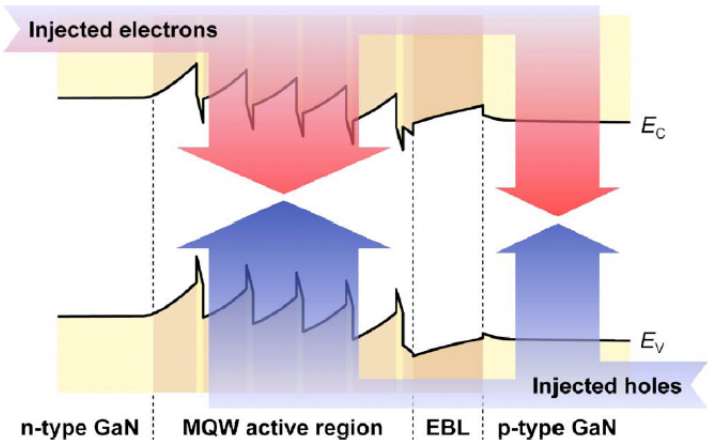

Figure 3.12: Schematic of the CB and VB energies of an InGaN-based LED heterostructure, including n-type GaN, InGaNMQWs, AlGaN EBL, and p-type GaN regions. Arrows indicate regions of electron and hole injection and recombination. From [6].

a p-type MQW structure or a single p-type InGaN active layer.

Overall, the origin of efficiency droop is still under investigation, but improving the hole distribution in the QW is a common strategy to avoid both higher order nonradiative processes and carrier transport limitations, and it will be likely better developed in future LED chip designs.

Because of the monotonic decreasing of the η_{ext} with the operating current, an efficiency enhancing is possible through an enlargement of the LED die, so that a lowering of the complexive current density is obtained. With this and other manufacturing accorgiments, similar to those applied to the OSLON LED and described in section 3.7, Narukawa et Al. [9] built a super-high luminous efficacy white LED .

3.5 Some examples of LED chip design

The chip design strictly depends on the heterojunction used in it, and so from the materials adopted. We have seen that to each composite heterostructure corresponds a determined bandgap and as a consequence a certain light radiation and peak wavelength. If we want to create a light source with a certain color, we will have to choose among only few direct-bandgap semiconductors and then we will be bounded in the LED chip design. The reason

of this is the growing process, that will involve a type or another of fundamental substrate because of the required lattice matching.

Here we will consider the principal light extraction techniques and issues as regards the LEDs chip made with phosphide and nitride alloys.

3.5.1 III-Phosphide family LEDs

In this alloy family the principal problem is to reduce the negative effect of the absorbing GaAs epitaxial growth substrate on light extraction. On this purpose, many approaches have been adopted, and are described below.

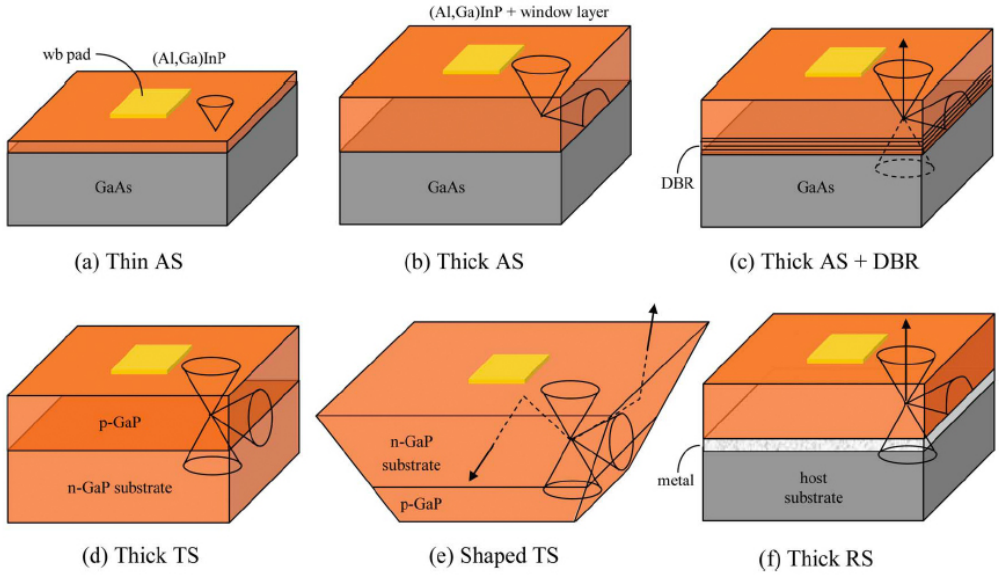

Figure 3.13: Common chip designs for AlGaInP LEDs. (a) Thin epilayers on GaAs absorbing substrate (AS). (b) Thick window layer on AS. (c) Thick AS design but including distributed Bragg reflector (DBR) above substrate. (d) Thick window layer on transparent substrate (TS). (e) Shaped TS (truncated-inverted-pyramid, TIP, LED shown). (f) Thick window layer on reflective substrate (RS). Consideration of escape cones (shown) allow estimations of extraction efficiencies. (Figure taken from [5].)

1. **Thin AS** is the simplest chip configuration and the one in which the absorbing substrate (AS) provides the lowest light extraction. It is represented in Figure 3.13 (a), and it is simply made up by a thin layer of AlGaInP over the growth GaAs substrate. Applying the Snell's Law to this configuration and considering that over the chip there might be

a silicone dome ($n_d \simeq 1.5$) that improves light extraction from the chip ($n_s \simeq 3.5$) to air ($n_a \simeq 1$), an escaping cone can be obtained. If the medium is thought to be an isotropic emitter then we obtain $\eta_{extraction} \simeq 4\%$, that is an upper bound because we do not take into account the Ohmic contact on top of the chip.

2. **Thick AS** is represented in Figure 3.13 (b) and features a thick window layer made of a transparent material, such as AlGaAs or GaP, that must be rightly mixed to garantee the transparency at the radiation wavelength. In this case, the window layer can help both spreading the current from the metallization, that is on the top, to the active region, and providing a side cone for the light to escape. If the extraction efficiency is calculated for this chip design, it will be approximately $\eta_{extraction} \simeq 12\%$.

3. **Thick AS + DBR** in 3.13 (c) has the same configuration of the previous one, but differs for a reflective substrate over the GaAs one, where the reflectivity is provided by a Distributed Bragg Grating (DBG), that can give an additional recovery of light from a "bottom" escape cone. This configuration increases the efficiency to $\eta_{extraction} \simeq 16\%$, but is not very used due to the difficulty in growing a perfect DBG, and the intrinsic limitation on this, such as the restricted reflection bandwidth.

4. **Thick TS** gives an opportunity to put the metallization below the whole chip, since the absorbing substrate of GaAs is here replaced by a transparent substrate (TS) such as GaP, represented in Figure 3.13 (d): this can be done removing the former with a selective wet chemical etching, and bonding the latter using high pressures and temperatures. In this way the transparency of the substrate provides a four-cone escaping for the light, plus the two on the upper and bottom side that depend on the metallization, and so a $\eta_{extraction} \simeq 20\% - 24\%$ can be estimated. In this configuration even an internal total reflection of the light has a chance to escape, and this is due to the transparency of the used substrates. In this way we will have a major light extraction, but the escaping pattern of the light may not be the desired one since it may be directed in an unwanted way.

5. **Shaped TS** resolves the problem of the directional flux of light, giving to the chip a shape that creates a preferential way of light escaping. In Figure 3.13 (e) is represented a Truncated-Inverted-Pyramid (TIP) shaped TS, but it is even possible to give a dome

shape (Hemispherical Dome) or a Compound Parabolic Concentrator (CPC). For the TIP configuration, that is actually the most used in commercial devices, it has been evaluated an external quantum efficiency of $\eta_{ext} \simeq 60\%$.

6. **Thick RS** features a metallization between the bulk substrate and the active semiconductor, in order to provide a reflective substrate (RS), as shown in Figure 3.13 (f). This configuration has been combined with the shaping of the whole chip into small active regions surrounded by reflective edges, together with a top surface texturing that garantees a higher light emission: this is an advantage as regards to what happens in the TIP-shaped LEDs , even though the external quantum efficiency is lower in this case, $\eta_{ext} \simeq 50\%$.

We have just pointed out that the extraction efficiency is strictly dependant from the chip design, and in the best case it reaches the 60%. Further improvements in the extraction of photons in this LEDs family are possible, even though intrinsic problems, like the weak-confinement power of the AlGaP-GaP heterojunction, are still limiting their complexive efficiency.

3.5.2 III-Nitride family LEDs

The design of LEDs chips from this material family is strictly dependant from the growth substrate: as a matter of fact the growth onto a SiC substrate provides a both transparent and conductive base so the Thick TS and Shaped TS approaches described above are viable. For the case of the Sapphire (AlO_3), we need to apply brand new designs because of the electrical insulation given by this substrate. They are summarized in Figure 3.14 and described below.

1. **Conventional Chip (CC)** is obtained depositing the Ohmic contact of the cathode onto the n-type layer, that is reached by etching the p-layers. This typically does not provide a good current-spreading, so a semi-transparent current-spreader p-type layer is deposited over the whole chip. The resulting configuration is represented in Figure 3.14 (a). The calculation of the extraction efficiency leads to $\eta_{extraction} \simeq 30\%$ considering a total loss of 50% of the light escaping from the upper and the bottom cone and counting the loss due to metallization. In this case, it is important to notice that approximately

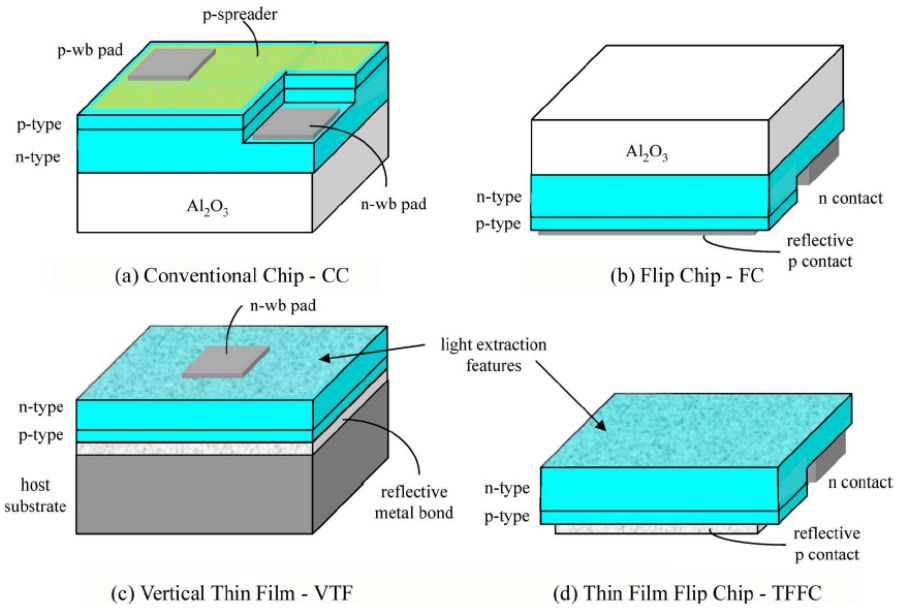

Figure 3.14: Common chip designs for sapphire-based InGaN-GaN LEDs: (a)"Epi-u" conventional chip (CC) with semi-transparent top p contact. (b) Flip-chip (FC) with reflective p contact. (c) Vertical-injection thin-film (VTF) bonded to reflective metal on host substrate. (d) Thin-film flip-chip (TFFC). Both thin-film designs provide access to the GaN surface for incorporation of light extraction features such as texturing or micro-optics. From [5].

half of the light is trapped within the GaN, so the improvements should aim to harvest this light.

2. **Flip Chip (FC)** overcomes the principal problems of the CC configuration, that concern the difficulties in spreading the current and light extraction, and even the thermal management due to the poor thermal conductivity of the sapphire substrate is improved. The FC design, reported in Figure 3.14 (b), presents a high-reflective p-contact in the bottom while the n-contact is realized as in the CC. Combining a localized QW and a series of thiny p layers, we can obtain a very high extraction efficiency, $\eta_{extraction} \simeq 60\%$, especially realizing a very accurate control of the distance between the reflective p-contact and the quantum wells, that can strongly improve the radiation pattern of photons and so the light extraction. In this way, and hypotizing a silicone dome over the chip, we can reach an essentialy complete extraction of light, except for the one that is totally-internally reflected at the GaN/sapphire interface.

This chip configuration enjoys also a very high thermal conductivity because of the proximity of the active region to the heatsink.

3. **Vertical Thin Film (VTF)** is very similar to the AlGaInP RS configuration, described above, but in this case the substrate is removed, and the GaP layer is substituted with a layer of GaN that is much lower resistive, and thus allows a thinner thickness for a good current spreading from the p contact, as reported in Figure 3.14 (c). Since lifting off the substrate is possible to access to the GaN epitaxy, a texturing of its surface can be implemented, bringing a very high extraction, such as $\eta_{extraction} \simeq 75\%$. It is worth to note here that the 100% of the extracted light is out from the top surface.

4. **Thin-Film Flip Chip (TFFC)** combines the characteristics of good light extraction and current spreading of the VTF with the good heat removal of the FC configuration. Indeed, after creating both the contacts opposite to the sapphire substrate, this layer is removed from the chip and the upper GaN layer is textured, in order to provide a good harvesting of the light that would be trapped within the GaN. This configuration bring to a light extraction of $\eta_{extraction} \simeq 80\%$ and is reported in Figure 3.14 (d).

   The performance of this chip configuration is so good that it is the most used one in state-of-art LEDs and it is useful to more deeply analyze the external quantum efficiencies measured in a study conducted in [5] and reported in Figure 3.15. In this figure is evident the efficiency droop, that is probably due to the increasing of current and heating within the chip, while very high values of η_{ext} and light output are obtained for a blue LED . This is a very important achievement since the blue LEDs are the one used in white SSL.

3.6 The structure of a white LED

We have already presented the structure of a Nitride LED , and mentioned that is used for the white lighting creation: here we will see how this is possible, applying and putting together all the notions so far analized.

Previously, a precisation is necessary, because the generation of white light can be implemented in many ways: the white light is the mixing of two or more spectral components, that can be perceived as white from the human eye, or can be saw as a quasi-continous spectrum

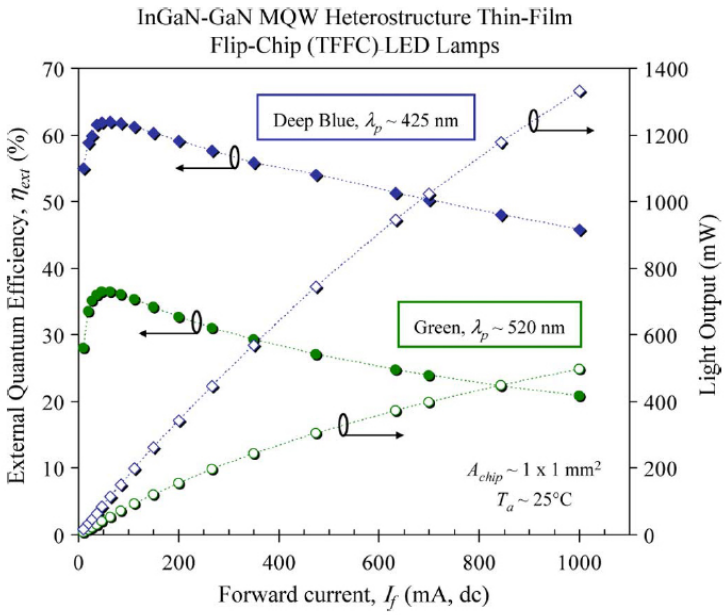

Figure 3.15: External quantum efficiency and light output versus dc forward current for both blue and green InGaN-GaN QW-based TFFC LED lamps. Chip sizes are $1 \times 1\ mm$. (Figure from [5].)

by a deeper analysis. This color mixing technique can obviously be obtained in different ways, for example [6]:

- $\mathbf{R_B G_B B}$ is a way to obtain an RGB-similar spectrum with a single LED source, that presents a blue LED that pumps a red and a green phosphor. In this case the complexive spectrum will be smooth and continous over the whole visible spectrum, but the phosphors conversion will introduce an additional intrinsic inefficiency;
- $\mathbf{RG_B B}$ is very similar to the previous one, but implies the use of two LEDs : one blue that pumps a green phosphor, and one red that covers the red portion of the spectrum;
- **RGB** uses instead three different light sources, to which can also be added a yellow one, obtaining a RYGB system. This system presents the most peaked spectrum among the ones considered because, as we know, each of the three light sources renders a narrow-band and intense color, and the resultant light would appear white to the human eye, whereas the CRI will be much lower than the others.

In this work we will just analyze a white light source obtained with a blue LED that pumps a mixture of yellow phosphors (YAG), so that the resultant spectrum will be much

similar to the one represented in Figure 3.16.

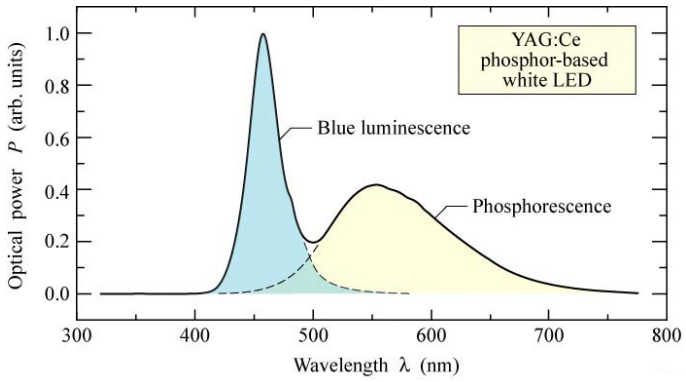

Figure 3.16: Emission spectrum of a phosphor-based white LED, from [4]

3.6.1 The InGaN blue LED die

The InGaN-GaN alloy is used to create blue and green LEDs with high-brightness and high efficiency characteristics. The Indium mole fraction determines the energy gap and so the final color peak of the radiation: if we want to obtain a blue LED , then the right alloy would be $In_{0.2}Al_{0.8}N$. The structure of a blue LED chip is represented in Figure 3.17, it is a single-quantum-well structure because it presents just one very thin active layer of $In_{0.2}Al_{0.8}N$.

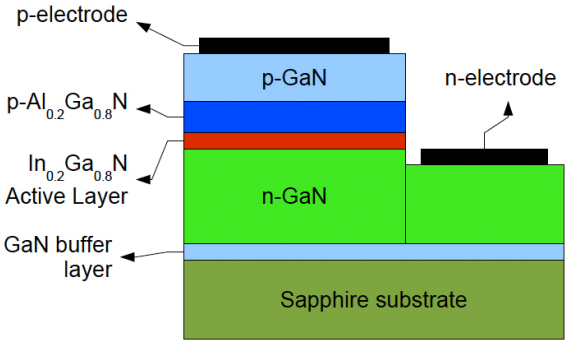

Figure 3.17: The structure of a blue InGaN LED die

3.6.2 The phosphor conversion

As we saw for the fluorescent lamps, the phosphors are very useful in fulfilling a part of the visible spectrum that the principal light radiation cannot cover. To implement this we need a pump source and the right mix of phosphors that must have the same excitation wavelength of the pump and the desired radiation pattern.

A common down-converting phosphor material is the $Y_3Al_5O_{12} : Ce^{3+}$, named also YAG. Its excitation spectrum is peaked at $\sim 440 - 460\ nm$, and is well matched with the radiation spectrum of a InGaN-GaN LED , while its radiation is a broadband spectrum, as can be seen in Figure 3.16, around the yellow. The adding of the yellow color to the pumping blue gives the opportunity to reach very high CCTs, from 4000 to 8000 K.

Now, we shall consider the effect of the phosphor down-conversion in the computing of efficiency of the whole device [5]. If a blue LED that pumps YAG at $\lambda = 460\ nm$ is considered, there will be a certain blue light residual as the pump transfer energy to the phosphors, and the more the blue peak is converted, the more important becomes the yellow emission. The chromatic coordinates nearer to the white point occur at CCT $\sim 5000\ K$ and for a blue leakage of 35%. The lumen equivalent of the white emission would be theoretically of 328 lm/W, but the down-conversion increases the efficiency losses that can be determined as follows.

Let's consider a LED with a total output power of P_{LED}, then the residual pump light, that corresponds to the blue peak, is

$$l \cdot P_{LED} \cdot \eta_{opt,pump}, \tag{3.23}$$

while the down-converted light is

$$(1 - l) \cdot P_{LED} \cdot \eta_{QE,ph} \cdot \frac{\bar{E}_{n,ph}}{\bar{E}_{n,pump}} \cdot \eta_{opt,ph}, \tag{3.24}$$

where l is the fraction of residual pump light, η_{opt} is the optical extraction efficiency, $\eta_{QE,ph}$ is the quantum efficiency of the phosphors, and $\bar{E}_n$ are the centroid photon energies of the pump and phosphors radiation. The total conversion efficiency (CE) is found adding (3.23) to (3.24) and normalizing to P_{LED}:

$$\text{CE} = l \cdot \eta_{opt,pump} + (1 - l) \cdot \eta_{QE,ph} \cdot \frac{\bar{E}_{n,ph}}{\bar{E}_{n,pump}} \cdot \eta_{opt,ph}. \tag{3.25}$$

It is worth to notice the strict relation of the total CE with the quantum efficiency of the phosphors and the extraction efficiency. If the latter equals 100% then CE reaches its maximum value, which is always lower than 100% because of the different energies of yellow photons ($\bar{E}_{n,ph}$) and blue pump radiation ($\bar{E}_{n,pump}$). At the white point, that is reached for a particular combination of blue LED and YAG phosphors, we have CCT $\sim 5000\ K$ while CE $\simeq 86\%$ (or $283\ lm/W$) if this quantity is evaluated in the ideal case described above.

Not all the pump radiation is necessary to be converted, as it happens for the UV-pump radiation of fluorescent lamps, because the blue peak is necessary to render complete the final radiation spectrum. In order to fully exploit the phosphors, the chip design has to be changed, thus a little cavity between the active chip and the epoxy dome is filled with the phosphors, as depicted in Figure 3.18.

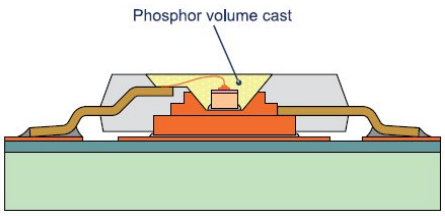

Figure 3.18: The common design of a LED with phosphors over the chip

The multi-phosphors approach A the single-phosphor solution for obtaining a white light source is very simple and its spectrum is characterized by a blue radiation peak and a lower but wider phosphor emission. This solution makes CRI to be tipically below 80 and CCT to be of about 4000 K: these characteristics are not acceptable for an indoor lighting, and another solution must be found. In order to achieve a CCT of about 3200 K (like the incandescent one), and a CRI as high as possible, one solution is a multi-phosphors approach [5], since recent researches on nitride compounds have developed a new class of phosphors based on nitrosilicates. These materials exhibit high quantum efficiency, good thermal behaviour and chemical robustness, so they are an optimal solution to adopt in SSL.

The nitride compounds are called N1 and N2, and their spectra, with the blue pumping LED , are reported in Figure 3.19. For the YAG+N1 case (orange curve), we obtain a quite warmer spectrum but with a low red component, and the resulting CRI is still too low, while the lumen equivalent (LE) is as high as for the single YAG use. In order to reach a higher

	YAG	YAG+N1	YAG+N2
LE (lm/W)	340	342	274
CCT (K)	5600	3200	3100
R9	-39	-24	73
CRI	71	73	89

Table 3.1: Main characteristics of a multi-phosphor LED device, found combining a InGaN LED plus a YAG phosphor or YAG+N1 or YAG+N2 nitride phosphors. Adapted from [5].

CRI, a different type of Nitride phosphors must be employed, as it happens in the YAG+N2 case (red curve). These phosphors emit in the deeper red thus the R9 index (that is the red-reference one) is evidently higher in this case, and the resulting CRI is much higher too, as reported in Table 3.1. This improvement costs a LE lowering that passes from the previous 340 lm/W to a modest 274 lm/W, that is due to the increased quantum deficit, increased optical losses and lowering of the quantum efficiencies.

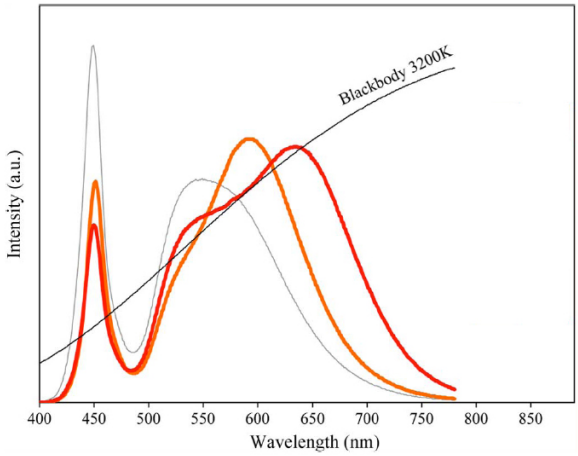

Figure 3.19: Relative luminescence specta of blue 450 nm-pumped phosphors for generating white light. Shown are high CCT white from YAG (grey), and low or "warm" CCT white from YAG plus nitride phosphors N1 (orange) and N2 (red). (Figure adapted from [5].)

3.7 The ThinGaN chip design

A particular white LED design is now to consider, principally because of the high efficiency it provides and also because it is applied in the OSLON design [8], a device that we will study

in the next chapter.

We have already stated how important is the light extraction efficiency within the chip: in order to improve this feature, OSRAM pioneered a thin-film approach that revealed to be successfull and that is running productive since 2004. The structure, that is represented in Figure 3.20, is doted of a reflective mirror on the carrier side that helps confining the photons on the GaN layer, and a structured surface at the LED top side that improves the light extraction. As it can be noticed, the configuration of the surface, is optimized for high-power

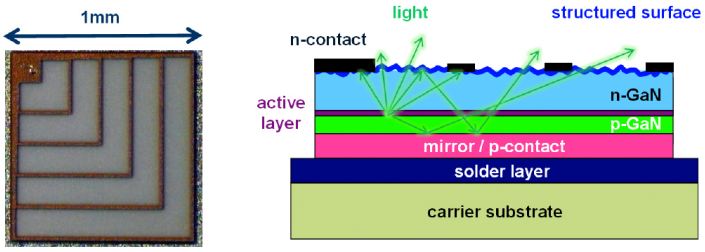

Figure 3.20: Top view on a 5-current-spreader PowerThinGaN chip (left) and a schematic cross-sectional view on ThinGaN-LED design (right). (Figure from [8].)

operating by means of a special design of the metallization that has a current-spreading functionality. The absorber layers are minimized and the most relevant one is the upper metallization: a reduction of the number of current-spreading contacts from 5 to 2 yields to a 35% lowering of absorbers but also a more inefficient current injection.

A minimization of the metallization on the surface, still maintaining a good current spreading is provided by a buried n-contact, as represented in Figure 3.21 (right), that is disposed below the p contact, and is mirror-shaped thanks to a highly reflective contact. In

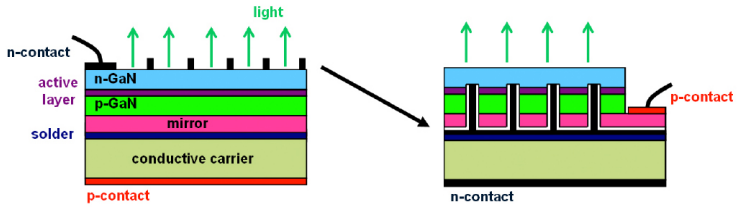

Figure 3.21: Comparison of cross sectional views of ThinGaN chip structure (left) and advanced chip design (right). The light extraction can be remarkably enhanced by moving the n-side current distribution layers below the p-contact. (Figure taken from [8].)

this configuration, the n-contact fingers are connected to the buried n-current distribution

layer by insulated vias through the insulation and the p-metallization. The whole structure is wafer bonded to a carrier substrate, and the sapphire is lift off via laser removal. In this design approach the mechanical and thermal control are clearly critical, but the reliability tests were successful.

In addition to the optimization of the external quantum efficiency, this chip design improves also the electrical aspects, thus especially for high current operation the serial resistance is reduced and a significant reduction in forward voltage is observed.

Eventually, the carried improvements both in the external quantum efficiency, that are due to an optimized epitaxial growth MQW structure, and in the current spreading, give to the chip excellent high current characteristics: at 350 mA operation the chip produces a light output of 643 mW and, if a suitable phosphor coating is applied, an efficacy of 136 lm/W can be achieved. In addition to this, advanced tests realized under stress conditions have demonstrated an optical power of 830 lm for a forward current of 3 A.

Another important advantage of this LED chip is the maintainment of the light emission pattern, that can be a critical aspect, for example in automotive applications. The light emission has been demonstrated to remain constant even for high current densities, and this proves the full scalability of the technology, that can be applied to produce high luminance multichip arrays.

3.8 Future challenges in efficiency improvements

According to [5], many improvements in the InGaN LED structure are possible, especially in the internal quantum efficiency and heat generation and management. As stated in section 3.5.2, the light extraction has already reached satisfactory levels, so the main issue regards the internal quantum efficiency. For InGaN/GaN QW blue and green LEDs the η_{int} reaches the $\sim 70\%$ and $\sim 36\%$ respectively, at low current densities; if the current is increased the internal efficiency decreases and the junction temperature raises: this represents a serious challenge for solid-state lighting since high operating current densities is the key to reduced cost of ownership.

Considering the impact of such improvements into the overall efficiency, a simple scheme is provided in Figure 3.22. (a) represents the energy distribution for a commercial single-phosphor high-power LED with an efficacy of 70 lm/W, while (b) shows the potential future

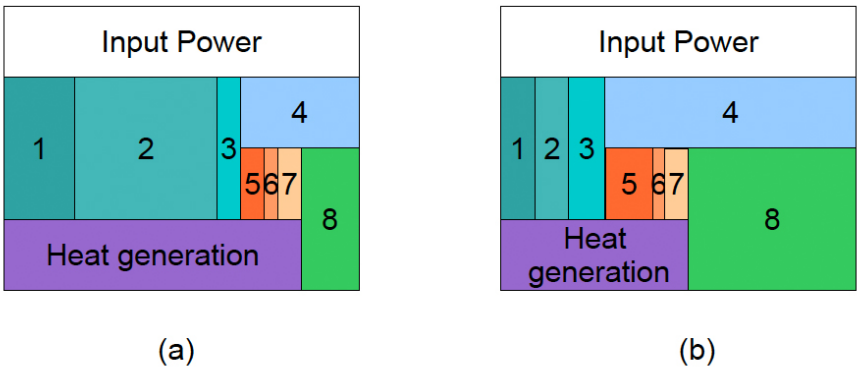

1 – Resistive losses (19 → 10%)	5 – Photon down-conversion (7 → 14%)
2 – Nonradiative – InGaN (41 → 9%)	6 – Nonradiative – phosphor (1 → 3%)
3 – Opt. absorpion – blue (6 → 12%)	7 – Opt. absorption – phosphor (5%)
4 – Visible radiation – blue (34 → 69%)	8 – Visible radiation – white (21 → 47%)

Figure 3.22: Energy balance diagrams for blue-pumped single phosphor (YAG) high-power white LEDs ($350\ mA$). (a) Commercially available LEDs at $70\ lm/W$: 80% of power is lost to heat, so only 20% goes to useful light output. (b) Potential future performance - assuming internal quantum efficiency for the blue LED reaches 90% and modest reductions to electrical and optical losses - reaches $160\ lm/W$. In this case, the power split between heat and light is approximately 50/50. (Figure adapted from [5].)

performance under the assumption that η_{int} is increased to $\sim 90\%$, while the electrical and optical losses are modestly reduced: in this way the efficacy would rapidly increase to $\sim 160\ lm/W$. In addition, it is clear that once the internal quantum efficiency is improved the heat removal issue becomes vastly simpler: while in the upper part of the scheme the light gains a quarter of the total input energy, in the second scenario the amount of heat generation reduces to be about the same as the light generation.

CHAPTER 4

Three examples of commercial high-power LEDs

In this chapter a review of the LED device is presented, and a deep analysis of the three LEDs studied during this thesis work is conducted. As a matter of fact, once the working of a common LED has been fully understood, it is important to see how its variants are implemented and what are their features.

In the following the more relevant features of these LED devices are provided, taken from their respective datasheets. This descriptive chapter is important because it either provides a direct and practical application of the notions previously analyzed and it introduces the measurements applied and explained in the next chapters.

The LEDs that have been examined in this thesis are the state-of-the-art of the cool white LEDs that are currently used in the SSL and more precisely in LEDs lamps, provided by the leading manufacturers, and these are:

- CREE XLamp XP-G LEDs , represented in Figure 4.1 (a);
- OSRAM OSLON SSL 80 - LCW CP7P.PC LEDs , Figure 4.1 (b);
- PHILIPS LUXEON REBEL General purpose white LEDs , Figure 4.1 (c).

All these LEDs belong to a very large family, and almost all of them are used as part of a multi-LED lamp, sometimes commercialized by the same productor, sometimes not. The Cree

Maximum DC forward current (mA)	1500
Maximum reverse voltage (v)	5
Forward voltage at 350 mA (v)	3.0 - 3.75
Forward voltage at 700 mA (v)	3.2
Forward voltage at 1000 mA (v)	3.3

Table 4.1: Main electrical properties for the CREE XP-G, as provided in [11].

LEDs , for example, belong to a family whose devices have different optical characteristics, but with the same configuration and solder footprint.

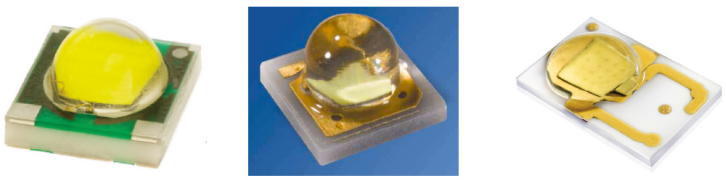

(a) (b) (c)

Figure 4.1: The representation of the studied LED devices: (a) CREE XP-G, (b) OSRAM OSLON, (c) PHILIPS REBEL. Figure has been taken from their respective datasheets, [11], [12], [13].

4.1 The XP-G LED

This device is available in many tipology, for example distinguished by the CCT in the cool, warm or indoor white, or alternatively in many types with a predefined CRI, and each category offers various LEDs with differents light flux.

The one used is a cool white LED with a luminous flux of 130 lm, that is not the highest of its family, nor the lowest. In the next sections are reported its principal electrical, thermal and optical characteristics.

The electrical features

In Table 4.1 are reported the values for the current and the measured voltage, while in Figure 4.2 a plot of the I-V characteristic is provided.

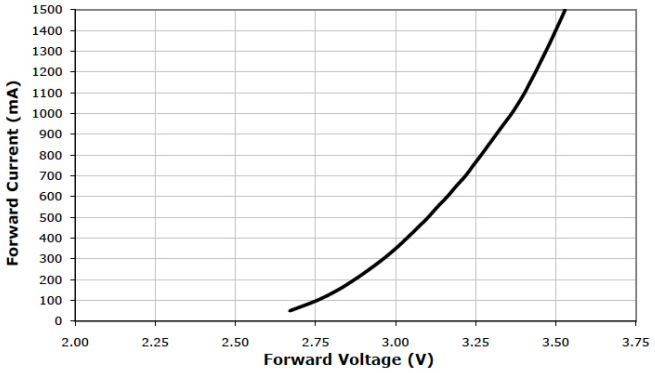

Figure 4.2: The CREE XP-G I-V characteristic, for $T_{junction} = 25\ ^oC$, from [11].

The thermal features

During a characterization of a LED device a particular attention is given to its thermal properties, since they can determine its lifetime and also its stress and operational conditions. The reported thermal resistance from junction to solder point is of $R_{thj-sp} = 4\ K/W$, while the maximum declared LED junction temperature is $T_j = 150\ ^oC$. In order to maximize the final lamp life and the optical performance, the maximum operating current is provided in Figure 4.3 where different values of thermal resistance from junction to ambient are considered. Once the thermal resistance is calculated for a particular lamp, and the ambient temperature is known, in order to avoid the device overheating a proper current derating is recommended.

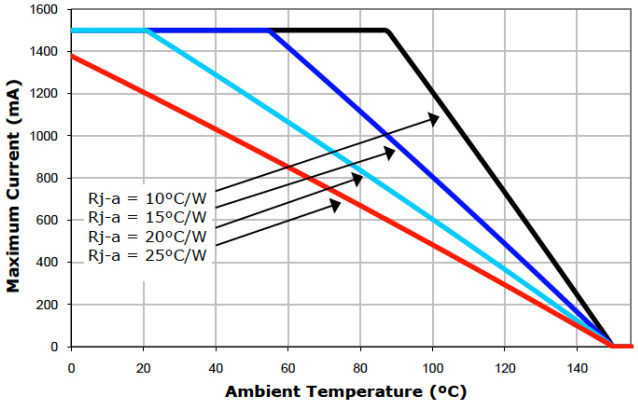

Figure 4.3: The maximum operational current for the CREE XP-G LED where different values of thermal resistance are considered, from [11].

CCT range (K)	5000 - 8300
CRI	75
Minimum luminous flux at 350 mA (lm)	130
Minimum luminous flux at 700 mA (lm)	243
Minimum luminous flux at 1000 mA (lm)	325
Minimum luminous flux at 1500 mA (lm)	433

Table 4.2: The CCT and luminous flux for the CREE XP-G, as provided in [11].

The optical features

Another detailed description is provided for the optical characteristics, as they are the basis on which we choose the device, but they are also the more variable with the operating conditions and the LED mounting process.

In Table 4.2 are reported the data from the mamufacturer and in Figure 4.4 is reported the relative spectrum for several XP-G LEDs devices. Figure 4.4 shows that the phosphors conversion in the red curve leads to a relative lowering of the blue peak with respect to the phosphors emission, and the result is a warmer light with a lower CCT.

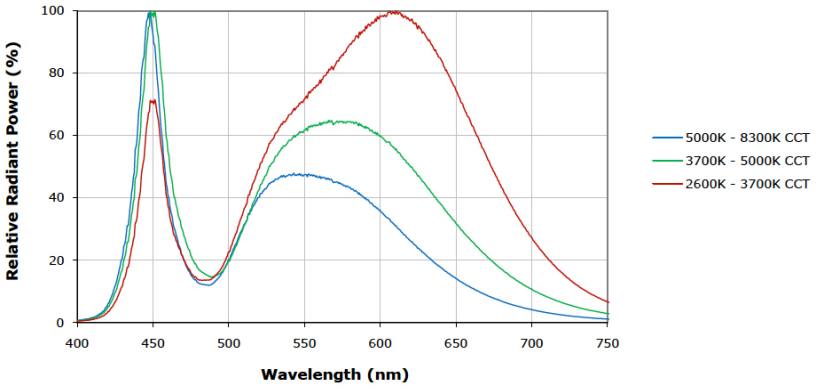

Figure 4.4: The relative spectrum intensity for the CREE XP-G LEDs family, where Cool White (blue), Neutral White (green) and Warm White (red) are considered. From [11].

DC forward current range (mA)	100 - 1000
Maximum reverse voltage (v)	Reverse operation is not allowed
Forward voltage at 350 mA (v)	2.75 - 3.2 - 3.75

Table 4.3: Main electrical properties for the OSRAM OSLON, measured for an ambient temperature of $T_{amb} = 25\ ^oC$, and provided in [12].

4.2 The OSLON LED

The second considered device is produced by OSRAM, and takes part of a larger family, the OSLON, which provides differents LEDs for various applications. Even in this case we will report the electrical, thermal and optical properties provided by the datasheet [12].

Moreover in this case we dispose of additional information about the chip configuration: as a matter of fact, the chip is an application of the ThinGaN technology, that has been described in section 3.7. The chip has been installed in the pre-existent generation of OSLON device, which demonstrated a very high and useful affinity for what concerns both the electrical characteristics and the secondary optics applications.

The electrical and thermal features

In Table 4.3 are reported the maximum and standard operating conditions, while the I-V characteristic is represented in Figure 4.5(a).

The maximum declared junction temperature is of $T_j = 125\ ^oC$, which is very low compared to the others probably because of the reduced dimensions of the device, that is certainly the smallest among the ones considered here and probably the smallest among all the existing power LEDs too. This low value could be a problem once a stress condition is forced, even because of the high junction-to-solder point thermal resistance, that is declared to be from 7 to 9.4 K/W. In addition to this, the manufacturer provides an optimistic plot of available currents as a function of the ambient temperature, reported in Figure 4.5(b). In this plot is also not clear what is the considered thermal resistance.

The optical features

Since this device is based onto the InGaN alloy, the spectrum is very similar to the other's one, and the color temperature is about 6500 K. The principal luminous characteristics are

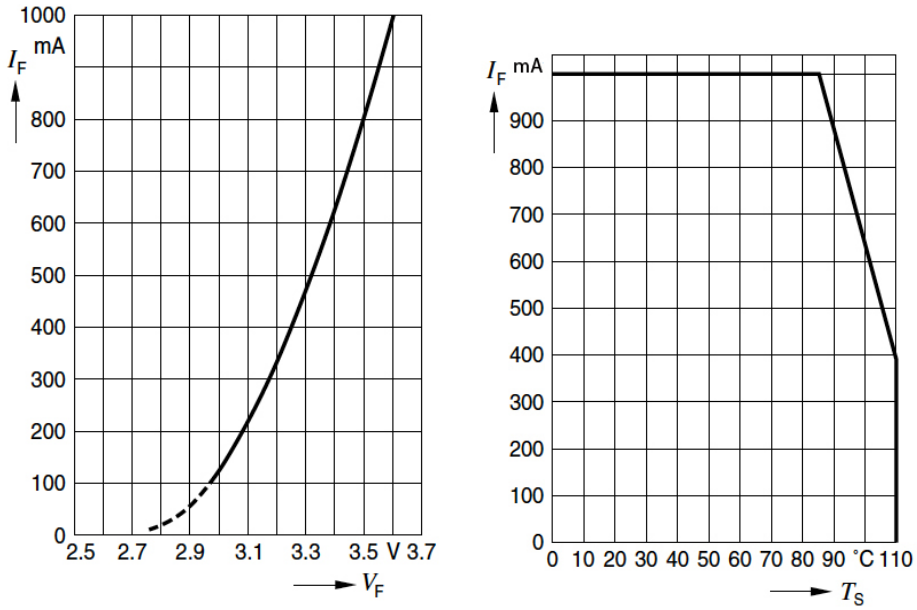

(a) (b)

Figure 4.5: (a) The forward I-V characteristic for the OSLON LED , with $T_{amb} = 25\ ^oC$, and (b) the maximum recommended forward current for various ambient temperature values, from [12].

CCT (K)	6500
Luminous flux range at 350 mA (lm)	89.2 - 112
Optical efficiency at 350 mA (lm/W)	100

Table 4.4: The main optical properties of the OSRAM OSLON, as provided in [12]. In this case the manufacturer does not provide the data concerning the CRI value.

listed in Table 4.4, while in Figure 4.6 is reported the emission spectrum together with the human eye sensitivity.

4.3 The REBEL LED

This device, described by the manufacturer as "the most widely used power LED today" [13], is the third sample that we will consider in our analysis and its features are here reported.

The datasheet of this device is the most detailed and provides, among the typical information, even a "Average Lumen Maintenance Characteristics", a projection by PHILIPS Lumileds that states that its product will deliver, on average, 70% of Lumen maintenance at

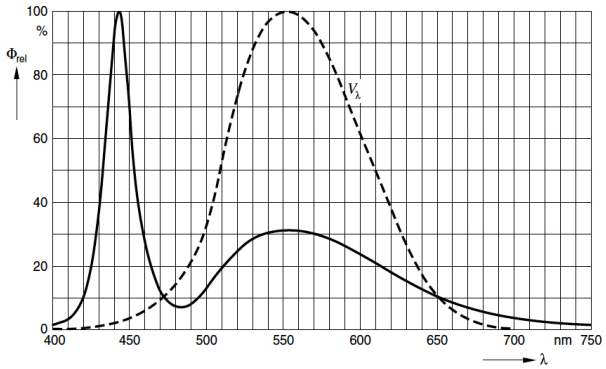

Figure 4.6: The relative spectrum of the OSLON LED (solid line), for a forward current of $I = 350\ mA$ and an ambient temperature of $T_{amb} = 25\ ^oC$. The human eye sensitivity $V(\lambda)$ is also reported (dashed line). (Figure from [12].)

Maximum DC forward current (mA)	1000
Maximum reverse voltage (v)	Reverse operation is not allowed
Forward voltage at 350 mA (v)	2.55 - 3.0 - 3.99
Forward voltage at 700 mA (v)	3.2

Table 4.5: Main electrical properties for the LUXEON REBEL, as provided in [13]. The data are measured with a thermal pad temperature of $T_{thpad} = 25\ ^oC$.

50.000 hours of operation at the operating current of 700 mA. This value has been obtained by the measurement of the light output with the junction temperature maintaned below 135 ^oC and it is much interesting because it is the typical statement that this thesis work should finally confute or confirm.

As regards the other provided data, they can still be divided into three sets, that are listed below.

The electrical features

The description of these LEDs provides not only a precise measured value for the voltage reached in different conditions, but also a whole range of voltage values that can be measured at different temperatures, as reported in Table 4.5: as a matter of fact, the data represent the minimum - typical - maximum set of measured voltage for the junction temperature ranging from 25 ^oC to 110 ^oC and thermal pad at 25 ^oC. The I-V characteristic is reported in Figure 4.7.

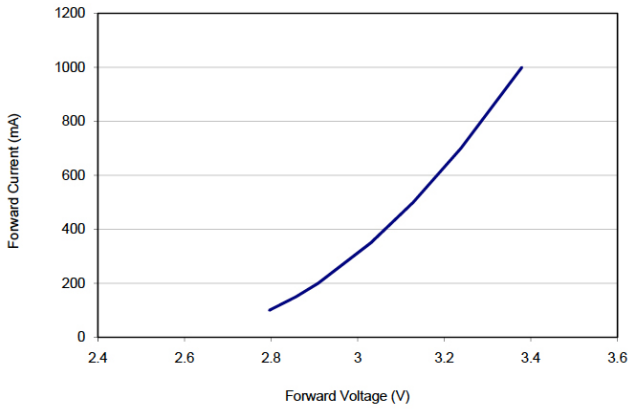

Figure 4.7: The LUXEON REBEL I-V characteristic, for $T_{thpad} = 25\ ^oC$, from [13].

The thermal features

A thermal resistance of $T_{thj-sp} = 10\ K/W$ is provided, while the maximum junction temperature is of 150 ^oC. A lowering of the current is recommended in case the maximum temperature is achieved, and some plots for the current derating for a drive current of 350 mA, 700 mA and 1000 mA are also provided. In Figure 4.8 is reported the one about a driving current of 700 mA, where different deratings for certain values of thermal resistance are plotted. This plot is realized setting the current to 700 mA and verifying that the junction temperature stays below the maximum of 150 ^oC for different ambient temperatures: if it overcomes the limit, a proper derating of the current is necessary as indicated. For an optimal

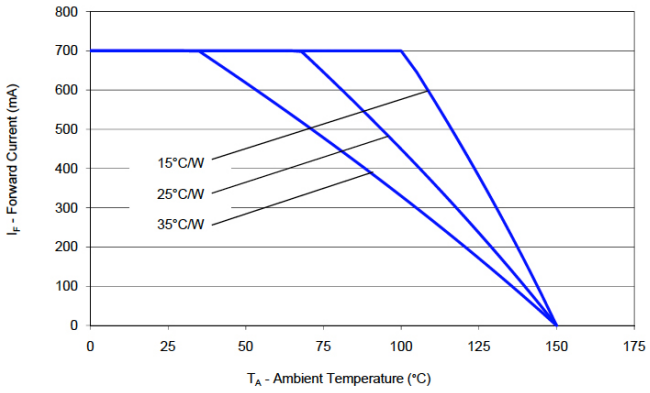

Figure 4.8: The maximum operational current for the PHILIPS REBEL LED where different values of thermal resistance are considered, starting from 700 mA and then derating the current with the junction temperature increase. From [13].

CCT range (K)	6020 - 7040
CRI	65 - 70
Luminous flux (lm)	90 - 105

Table 4.6: The CCT, CRI and luminous flux for the PHILIPS REBEL, as provided in [13], for the test current of 350 mA.

soldering process, even in this case the oven-heating profile is provided, and even the footprint of the package is represented in this datasheet.

The optical features

In Table 4.6 are provided the minimum - typical optical characteristics for this LED , while in Figure 4.9 is reported the typical spectrum obtained with the test current of 350 mA.

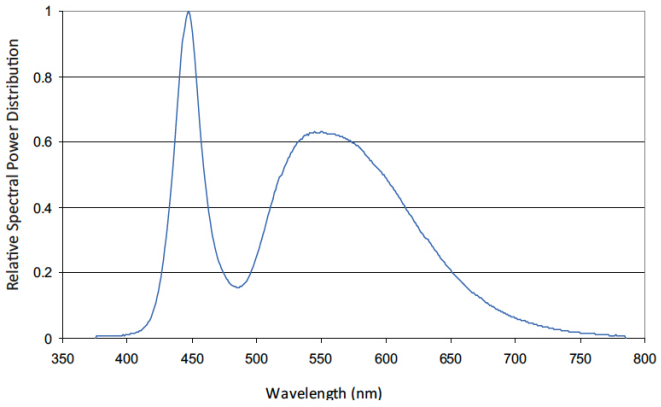

Figure 4.9: The relative spectrum distribution of the PHILIPS REBEL LED when a test current of 350 mA is applied and the thermal pad temperature is $T_{thpad} = 25\ ^oC$, from [13].

CHAPTER 5

Measurement methodology and applied instruments

In this chapter the instrumentations used in the measurement laboratories are described, and the applied methodologies and processes. Once the theoretical basis are set we point out the phases of the measurements and the used media in order to fully understand the experimental results: the various types of characterizations implemented are presented, each explained as in details as possible.

The main instrument used is definitely the 2612 SourceMeter, because as we will see in this chapter almost the investigations are conduced via electrical measurements. The second is the Integrating Sphere, described in section 5.3, that, used in association with the spectrometer and the sourcemeter, provides the main optical data needed to verify the stress results.

5.1 The electrical characterization

As it has already been mentioned, the electrical measurements are the basis of all the others, so it is useful to start from the description of the sourcemeter, the switch unit and the 4-wire measurement method and some measurements examples.

5.1.1 The Keithley 2612 SourceMeter

This instrument, manufactured by Keithley, is the main sourcemeter adopter for electrical measurements, sometimes it is replaced by the 2612A that maintains the same characteristics described below.

This dual-channel device, obviously apted for the 4-wire measurement, has been controlled by a Labview software scripted for the required measurements, throught the GPIB interface, sometimes just one channel has been used, sometimes both two: in most of the cases the instrument was used synchronized with the Switch Unit or the oven, in order to obtain more efficient and rapid measurements.

In Figure 5.1 is reported the I-V capability of the instrument, both in pulsed and DC operation: the low DC voltage of each LED , that was of 4 V maximum at 1 A, makes this instrument suitable to our purposes.

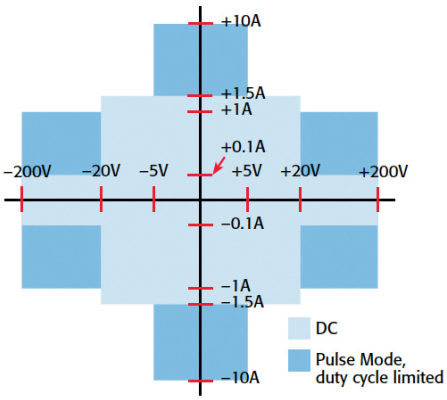

Figure 5.1: I-V capability of the 2612 SourceMeter, as provided in [15].

Considering that LEDs must be driven by current, the source was set in current mode, imposing a compliance voltage value of almost 5 V, while the voltage was measured, we will consider just the capabilities in current for the source and in voltage for the meter:

- source accuracy is of 30 μA, while the peak-to-peak additive noise is of 600 nA maximum;
- meter accuracy is of 350 μV, where a very high input resistance is applied, $> 10G\Omega$.

These data evidently state how suitable is this instrument for our measurements and that the accuracy provided is well below the one needed.

5.1.2 The HP 3488A Switch Unit

The Switch Unit is a very simple instrument used to speed up the measurements, indeed when it is used with the sourcemeter it allows a fast metering of each LED onto each board.

It consists in a passive matrix of switches controlled via the GPIB interface, and it is capable to switch an input channel between several outputs, so that the same source or metering signal can be applied to two or more devices one by one. Each of the measured PCB contained four LEDs , so a single input (based on a 4-wire setting) was switched to four outputs. The switching scheme is represented in Figure 5.2: the multiplexer provides a

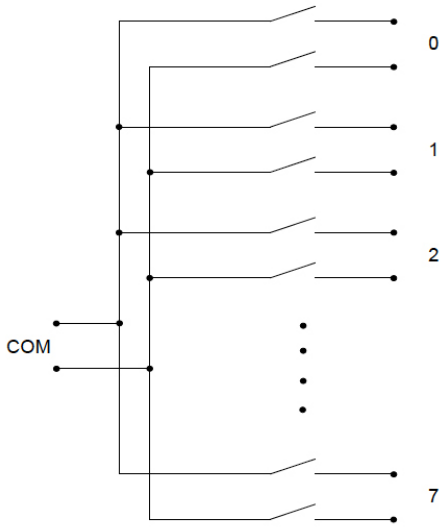

Figure 5.2: The relay multiplexer scheme of the switch matrix, in a 2-wire configuration. The 4-wire setting is obtained using two of multiplexers in parallel, as provided in [16].

control of eight devices, but we have used just the first four of them.

The sourcemeter and the switch matrix have been combined in order to perform measurements concerning thermal (transients, thermal maps and supertransients) and optical characterization (together with the integrating sphere and spectrometer), as we will discuss in the next sections.

5.1.3 The 4-wire Kelvin measurement

If we want to measure the voltage between the terminals of the device, we need to find a way to neglect the electrical influence of the measurements setup once a forward current

is applied to an electrical device: for example, if a resistance is to be measured, the wires used from the instrument to the device and back are still non-negligible resistances, so the complexive measured value will be a series of one or more parasite resistances.

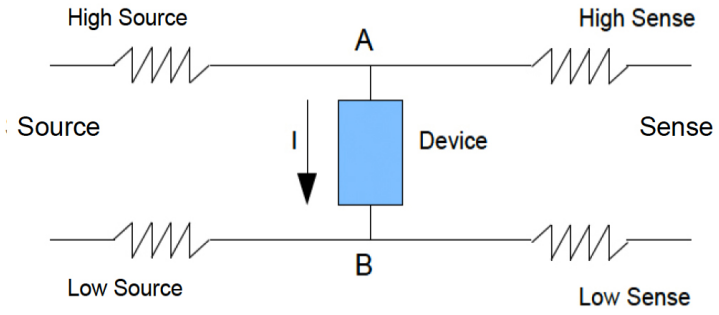

Figure 5.3: The setup used in the 4-wire measurement.

The solution to this problem is the *4-wire Kelvin measurement* that implies the use of four terminals instead of two, but assures more reliable results. The setup is represented in Figure 5.3: the source terminals are used to apply the required bias, thus the circulating current is the same in both the wires and the device, while two wires forming the sense stadium are connected in parallel: here no current is applied but just the voltage is measured, and this prevent the influence of the sense wires since the only biased element is the target device.

The only caution adopted in this proceeding is due to the fact that most of the times the A and B terminals are put on the PCB so the electrical vias from there to the effective device must be done with a certain accuracy.

5.1.4 The V-I and I-V measurements

The simplest electrical measurement is the one in which a current is applied and the voltage is measured, this is called he V-I measurement, conversely it is possible to polarize the device with the voltage and then measure the flowing current, obtaining the I-V.

Since the devices are usually driven in current, the V-I measurement is the more obvious because it renders the voltage reached for a certain current and a certain auto-heating condition, as we will see in the thermal characterization. In Figure 5.4 is reported an example of V-I measurement.

Let's notice how for a certain current each LED presents a peculiar V(I) curve; the voltage difference among devices of the same type is actually the reason why they are polarized in

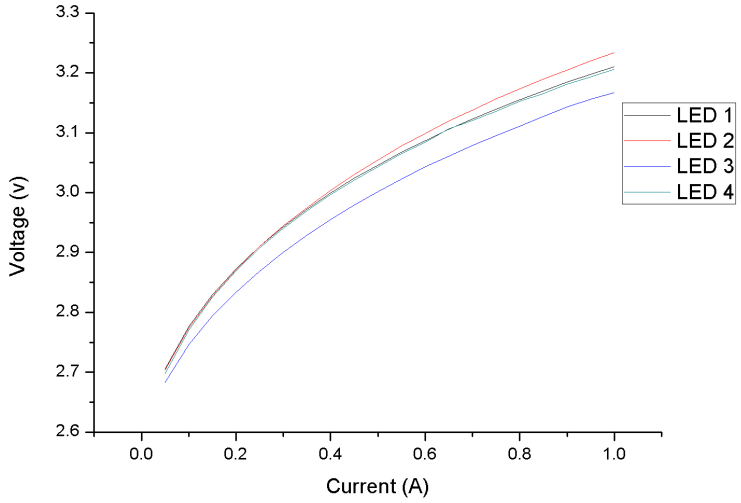

Figure 5.4: The V-I measurement for one of the XPG LEDs MCPCB, actually the XPGA. This has been done during the zero-hours optical characterization, and all the four LEDs are reported.

current: since the voltage difference is directly due to the built-in voltage of each LED , the same current driving for all the chips assures a homogeneous current injection into the active region and so the same light output power among the LEDs [1].

The complementary measurement, the I-V one, is done during the stress in order to conferm the right electrical operation of the chip. With the data it provides it is evident the diode nature of the device: as a matter of fact, the I-V plots, as the ones reported in Figure 5.5, are similar to the ones reported in the section that deals with the diode.

5.2 The thermal characterization

As we underlined in section 3.2, one of the most important aspects in the SSL is the thermal management. The first step in a LED device characterization consists in aestimating its thermal resistance R_{th}. We can not assume valid the thermal resistance value provided by the manufacturer because of the particular setup of the stress condition, so the R_{th} of our devices was calculated: this is principally due to the fact that the datasheet-provided

[1] This homogeneity of the light radiation is just nominal and it does not take into account the differences concerning the electron injection, the photon extraction and other chip-peculiar characteristics that can still vary among the retail LEDs .

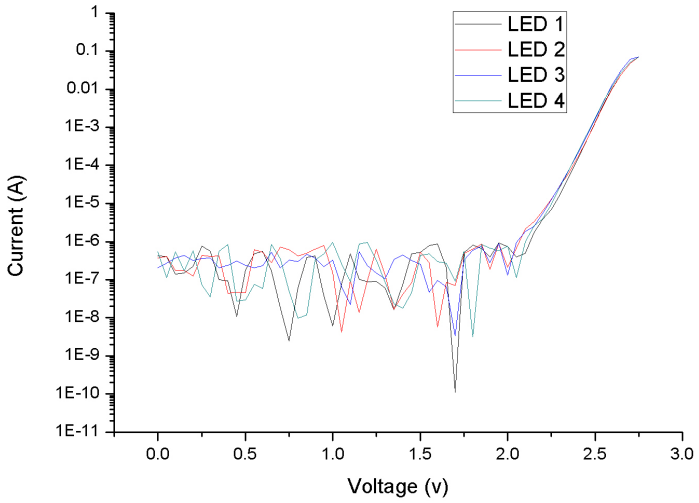

Figure 5.5: The I-V measurement for the XPGA PCB. This too derives from the zero-hours optical characterization, and all the four LEDs are reported. The current axis is logaritmic to put in evidence the low voltages for which the diode is not conducting.

R_{th} is the one from the junction to the solder point. In our assembly the LED is put firstly onto the Metal Core (MC) PCB and then upon the heatsink, thus the R_{th} value results to be extremely increased.

Postponing the measurement results to the next chapter, we analize here the methodology used in order to obtain the thermal resistance value [10]. This process is principally divided into three steps: the transients, the thermal maps and the elaboration of the results derived from both of them. The first two steps imply the use of the sourcemeter and a controlled climatic chamber only, and all the measurements are exclusively electrical thanks to the fact that, once a certain current is applied, the LED operating voltage is strictly dependant from the junction temperature. The idea underneath this measurement process is to fix the ambient temperature and, making simple electrical measurements, retrieve the junction temperature during the subsequent stress condition.

5.2.1 The transients

If the device is biased with a certain and constant current, the auto-heating triggers an exponential lowering of the voltage, until the heatsink and the junction reach a steady state

during which the temperature remains constant, because the thermal flux and its dissipation are constant too. This dynamics is called here *transient* and can be characterized by measuring the voltage at steady state V_f. In this case the effective junction temperature is still unknown, but the ambient temperature can be imposed: the devices are put inside the oven, a temperature of 35 ^oC is set and, after some temperature-stabilization ripples, the measurement is done.

Our aim is to find the thermal resistance, that, as seen in section 3.2, is

$$R_{th} = \frac{T_{junction} - T_{ambient}}{P_{th}} \tag{5.1}$$

which is actually a ratio between unknown values, thus we will realize different transients, varying the current in order to change the thermal power flux, as will be explained in the third step of this analysis. Figure 5.6 shows a single transient, realized with a XP-G LED for a current of $I = 700\ mA$ (left), and different transients realized for currents from 100 mA to 1.2 A with a step of 100 mA (right), the second plot includes also the classical operating current of 350 mA.

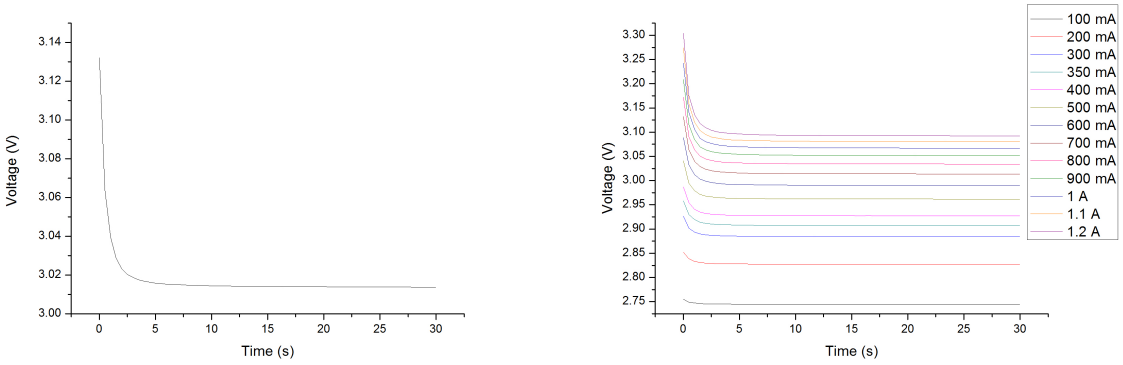

(a) Current of 700 mA (b) Currents from 100 mA to 1.2 A

Figure 5.6: Transients obtained from the thermal evaluation of XP-G LEDs , referring to the LED 1 of the PCB A (XPGA_1), for the first 30 s of operation.

Once the measurement is done, the data are fitted in order to find the necessary steady-state voltage V_f: the used fitting function is a third-order decay exponential, namely:

$$V(t) = V_f + A_1 e^{-t/t_1} + A_2 e^{-t/t_2} + A_3 e^{-t/t_3}, \tag{5.2}$$

where V_f is the quantity we need. In order to have a reliable datasets we must obtain a transient that is stable in its final part: this stabilization can be reached after at least 30

seconds of working, as the ones here reported. During these first operating seconds of the LED , the transients can reveal some misfunctions or electric problems of the device.

5.2.2 The thermal maps

The second step is the measurement of a set of data called *thermal maps* for each LED , that will be elaborated with the transients.

Even in this case using electrical measurements we will retrieve the effective operational junction temperature by the imposal of the ambient one: this measurement is performed by varying not only the current but also the ambient temperature. The device is put inside the oven and, for various steps of temperature, the V-I characteristic is measured. An example is reported in Figure 5.7.

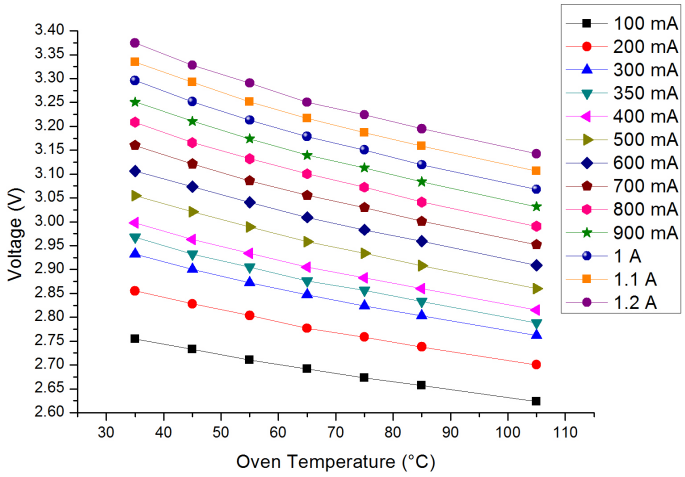

Figure 5.7: Thermal maps for a set of seven temperatures and for the same currents used in the transients. The plot refers to the measurement of the same device of Figure 5.6, the first LED of the XPGA PCB.

The oven temperature has been varied from 35 ^oC to 85 ^oC with a step of 10 ^oC, and a measurement at 105 ^oC has been done too. As soon as the temperature inside the oven is stable, the sourcemeter proceeds polarizing the device with the same set of currents as the ones used during the transients, and then it measures the voltage. Differently from the transients measurement, the voltage was measured in this case as soon as the device is fed, thus there was no thermal flux, and we can neglect the autoheating contribution during the

measurement. Nevertheless we can approximate the junction temperature with the ambient one, that corresponds to the oven temperature.

After the measurement, once again the data are fitted in order to retrieve the needed values: the voltage is a function of the junction temperature T, more precisely:

$$V(T) = V_0 + A_1 e^{-T/t_1}. \tag{5.3}$$

Hence, fitting each curve that represents the varying of the measured voltage with the junction temperature at a fixed current, we obtain the three parameters ($V_0,\ A_1,\ t_1$) that describe the thermal-electrical dependence for a LED device, as is stated by eq. (5.3).

5.2.3 The thermal resistance extrapolation

At this point we determine the junction temperature for the transients steady state condition, because we know either the steady state voltage V_f and all the other parameters useful to satisfy eq. (5.3). The temperature can be evaluated from eq. (5.3) as:

$$T = -t_1 ln\left(\frac{V_f - V_0}{A_1}\right). \tag{5.4}$$

If this proceeding is repeated for all the currents that have been applied, we find that the higher is the current, the higher is the temperature of the junction.

The thermal resistance is obtained referring to relation (5.1), where the unknown term is just P_{th}, because the $T_{junction}$ has been jet found and the $T_{ambient}$ can be set equal the oven temperature during the transient (35 ^oC). If we impose a certain current to the device and measure the voltage, the electrical power is known: a part of it, the *Joule power* (P_{th}), will be lost in heat, and the other in optical radiation (P_{opt}), so the following holds:

$$P_{tot} = IV = P_{opt} + P_{th}. \tag{5.5}$$

In this relation we considered neglectable the optical power in respect of the thermal-released one, $P_{tot} = IV \simeq P_{th}$, and the relation of the thermal resistance becomes

$$T_{junction} = T_{heatsink} + P_{th} R_{th}. \tag{5.6}$$

From this linear relation we can obtain both R_{th} and $T_{heatsink}$ by simply linearly fitting the Temperature vs. Power relation. The first parameter, i.e. the slope, is finally the thermal resistance while the second one, i.e. the intercept, is nothing more than the oven temperature that should be equal to the one set on the device (in our case 35 ^oC).

5.2.4 The junction temperature: supertransients

In addition to the determination of the thermal resistance, the thermal maps are useful to find the junction temperature during the LED operation, that is hardly retrievable with other methods.

In order to supply the steady-state voltage reached by the device, that, as we saw, depends on the junction temperature, we need to turn on all the LEDs onto the same PCB and measure the forward voltage one by one.The result of this measurement is here called *supertransient*. This is done using either the channel A of the sourcemeter, that measures the voltage of each device, and the channel B that provides the forward current at which we want to know the junction temperature. Since the feeding current is supplied for all the LEDs using the serial connection, the devices mutually heat when they are turned one during the measurement: this fact will be kept into account during the discussion of the experimental results.

In Figure 5.8 is reported the supertransient relative to the first LED of the XPGA board, that has been realized monitoring the LED during the first hour of stress at the ambient temperature of 85 ^oC.

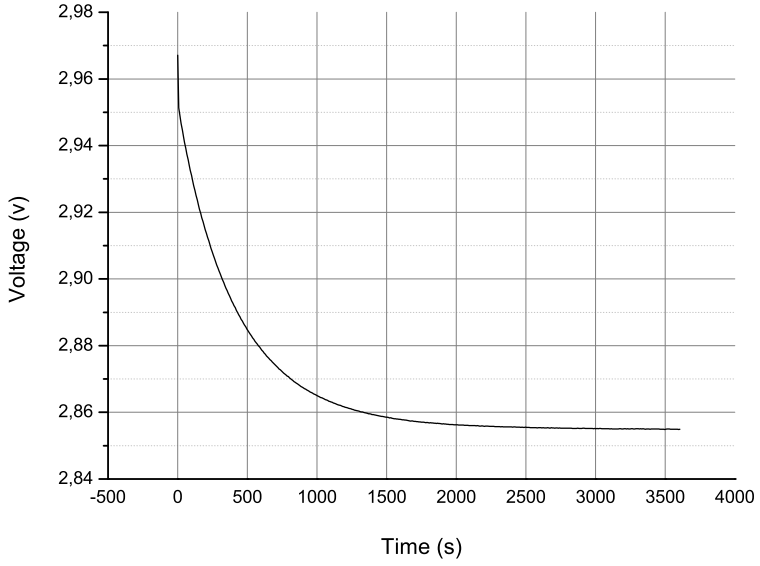

Figure 5.8: Supertransient relative to the first LED of the XPGA PCB, made during the first hour of stress at 700 mA and $T_{amb} = 85\ ^oC$.

5.2.5 The thermal camera use

Because of the hard stress conditions at which the LEDs are subjected, in order no to overheat them a preliminary evaluation of their temperature is possible, using a thermal camera. This is a very simple procedure that consists in turning on the LEDs and, using the images provided by the camera, evaluating their surface temperature and also the relative heating among all the LEDs of the same PCB. As shown in Figure 5.9, the upper left LED suffers from an apparent overheating respect to the others: this could be an index of bad thermal resistance, and probably a quick check of the thermal pad soldering may solve the problem.

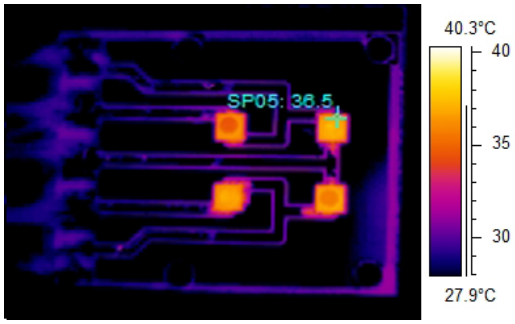

Figure 5.9: Image taken with the thermal camera, of the OSLONB PCB without the heatsink and driven at $350\ mA$. The relative color scale is reported.

5.3 The optical characterization

In this section the optical measurement setup is presented: as already stated, the *integrating sphere* is the most important among the used instruments because it can ensure the quality, repeteability and reliability of the optical measurements, that, being the sphere just a passive enclosure, have been possible by the use of the spectrometer, an important instrument that will be described as well.

The basilar operating principles of the sphere are here described through the reflectometry theory and the spectrometer will be analyzed as well.

5.3.1 The integrating sphere

The function of this device is to spatially integrate the radiant flux: the optical measurements conducted using the sphere allow the complete ignorance of the spatial distribution of the light radiation from the sample, since it is put inside the sphere and a little portion of the light is gathered. Before entering in the design details, it is important to understand how the sphere works, so we will explain the functioning from the basilar reflectance theory to the two related sphere parameters, the sphere multiplier and the average reflectance [17].

The sphere theory

Starting from two planar surfaces dA_1 and dA_2, the radiation exchange from the first to the second can be evaluated, and, if the differential elements are inside the diffused surface of a sphere, the radiance flux from the first to the second is expressed as

$$dF_{d1-d2} = \frac{dA_2}{4\pi R^2} \tag{5.7}$$

where, according to Figure 5.10(a), R is the radius of the sphere. Since R is obviously constant and the equation is independent from the viewing angle, the fraction flux received by dA_2 is the same for any radiating point of the sphere surface. Integrating eq. (5.7) over the entire sphere surface we obtain

$$F_{d1-d2} = \frac{A_2}{4\pi R^2} = \frac{A_2}{A_S}. \tag{5.8}$$

It is even possible to find the *radiance equation*, where the radiance is defined as the amount of flux that can be collected by an optical system that might view the illuminated

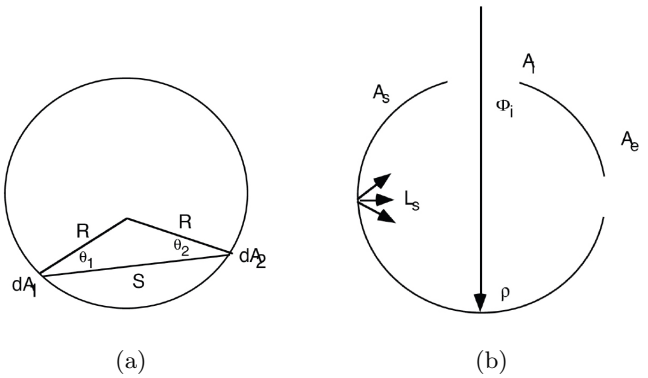

(a) (b)

Figure 5.10: Schematic representation of the light rays dynamics inside the sphere. (Figure taken from [17].)

surface. Figure 5.10(b) shows that two apertures within the sphere surface are required, one to let the light enter and the other as exit port. If a single reflection from one surface is considered, the radiance expression is the following:

$$L = \frac{\Phi_i \rho}{\pi A}, \tag{5.9}$$

where Φ_i is the input flux, ρ is the surface reflectance and A the illuminated area. If we want to apply this to an integrating sphere we have to consider both the multiple reflections inside it and the aperture losses. If the input port area is named A_i and the exit one A_e, the amount of flux incident in the total sphere surface, for just one reflection, can be evaluated as

$$L_{T,1} = \Phi_i \rho \left(\frac{A_S - A_i - A_e}{A_S} \right) \tag{5.10}$$

where the term inside parenthesis, that represents the net amount of light not consumed by the openings can be rewritten as $(1-f)$ with f the port fraction, defined as $f = (A_i + A_e)/A_S$. This parameter is very simple to calculate especially in case of three or more ports. The total incident flux over the entire sphere surface after n reflections is

$$L_{T,n} = \Phi_i \rho (1-f) \left\{ 1 + \rho(1-f) + \ldots + \rho^{n-1}(1-f)^{n-1} \right\}, \tag{5.11}$$

that can be extended for $n \to \infty$ to

$$L_T = \frac{\Phi_i \rho (1-f)}{1 - \rho(1-f)}. \tag{5.12}$$

If we apply this flux equation to eq. (5.9) we retrieve the sphere surface radiance:

$$L_S = \frac{\Phi_i}{\pi A} \frac{\rho}{1 - \rho(1-f)}. \tag{5.13}$$

Observing equation (5.9) we can notice that the first part is very similar to (5.9), and so the second is called *sphere multiplier* (M) because it is the difference between the radiance from a diffuse surface and the one generated by the sphere,

$$M = \frac{\rho}{1 - \rho(1-f)}. \tag{5.14}$$

This term accounts for the increase in radiance due to multiple reflections: its magnitude is very dependant from the port fraction f and the sphere reflectance ρ, as reported in Figure 5.11. Expression (5.14) is derived for an uniform-reflectance sphere wall and for ports with no reflectance, and its general expression is more complicated and not here reported.

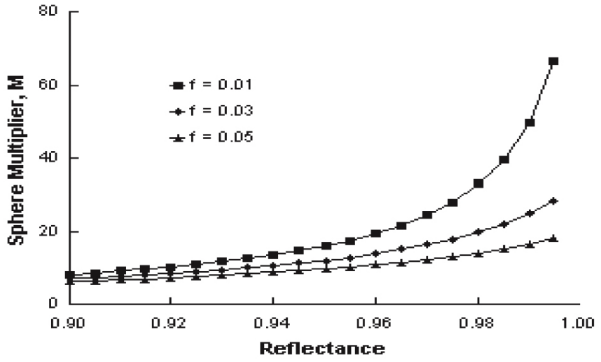

Figure 5.11: The sphere multiplier parameter M versus the coating reflectance and for different values of port fractions: the greater is the reflectance, the higher is M, from [17].

In order to obtain an exact analysis of the radiance distribution inside the sphere we have to consider the geometrical details of the actual sphere design, the reflectance distribution function for the sphere coating and the surface of each device mounted inside the sphere. The value we yield is the spatial integration of the measured light, thus the sphere design has to optimize all these parameters.

The sphere design

In order to meet a large number of applications the sphere design can be very variable, and it involves almost all the analyzed features as the diameter, the coating reflectance and the number and dimension of ports. In particular, the coating layer can be designed for a certain wavelength and the ports are chosen depending on the required devices and even the presence of baffles are here discussed.

The sphere diameter D_S is highly bound to the final required sphere multiplier, that is dependant from the aperture size as indicated in Figure 5.11: if for instance there are two port with unitary diameters, then the relative radiance results

$$L_S \propto \frac{M}{D_S^2}, \tag{5.15}$$

thus the greater the diameter, the lower the relative radiance. Since the integrating sphere is usually employed for its ability to spatially integrate input flux, larger sphere diameter and smaller port fraction will improve the spatial performance.

Another important parameter is the internal coating of the sphere, that can heavily influence the sphere multiplier: Labsphere employs two types of coating, both with a very

high reflectance, over 95% from 350 nm to 1350 nm[2].

In order not to expose the photodetector directly to the irradiated light flux, the aperture predisposed for the detector device has to be covered with a baffle: as a matter of fact the detector must reveal only the reflected light inside the sphere, while the directly irradiated light would introduce a false response. Baffles are coated with the same reflective material of the sphere, and must be positioned in order to cover the entire field of view of the detector, in order to prevent first reflections to be revealed. The baffles are considered an extension of the sphere surface and, although they are not very large compared to the sphere area, their contribution to it must be factored into the radiance equation.

The photodetector design is represented in Figure 5.12(a): in order to avoid the direct light flux is possible to attach to the principal sphere an auxiliary satellite integrating sphere: the port of this sphere is baffled from direct view of incident flux, and the detector with hemispherical field-of-view is directly coupled to it. Obviously, the estimation of the flux received by the photodetector has to take into account the design feature of the overall device.

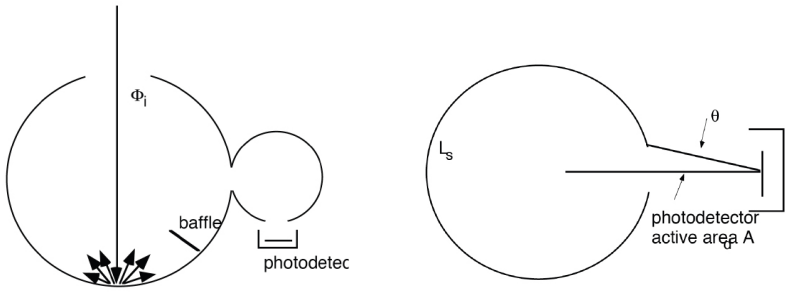

Figure 5.12: Schematic representation of the photodetector coupling with the sphere structure, from [17].

The sphere that we used is a 65-inch diameter sphere, with two ports, one for the detector and the other for the calibration lamp. The inner surface of the sphere is totally covered with a high-reflective coating, the declared reflectance is of 98%. The sphere houses a pedestal where the device is mounted: this can be moved up and down, in order to align the device with the center of the sphere, and that is doted of all the electrical contacts needed for the

[2]The diffuse reflectors offered by Labsphere are known as Spectraflect and Spectralon, more details are provided in [17]

measurements. The sphere itself is made up by two hemispherical halves that can be opened and closed sliding onto apposite rails.

The flux on the photodetector

The radiance of the sphere surface determines the total flux incident on a photodetector mounted at a port of the integrating sphere. Named as A_d the active area of the detector, the total incident light flux on it is:

$$\Phi_d = L_S A_d \Omega \tag{5.16}$$

where Ω is the projected solid angle, which can be approximated as $\Omega = \pi sin^2\vartheta$. We use an optical fiber system instead of a photodetector, thus the actual solid angle is given by the fiber numeric aperture (NA), $\Omega = \pi(NA)^2$. Reflectance losses at the air-fiber interface must be considered while determining the total flux thus eq. (5.16) can be adapted to our case as:

$$\Phi_f = L_S A_f \pi (NA)^2 (1 - R), \tag{5.17}$$

where R is the reflectance at the fiber face and A_f the area of the fiber end calculated from the core diameter. The light emitted from the other end of the fiber is a function of its length, the material extinction coefficient and the exit interface reflection.

We use of the optical fiber because we want to obtain not only the optical power emitted by the device, but also a more detailed spectrum. This is possible if we connect the fiber end to the spectrometer, a very important instrument that will be described in the next section.

Integrating sphere application

As we have just seen, the integrating sphere together with the spectrometer allows the measurement of the total irradiated luminous flux that comes from a lamp put inside it. The whole apparatus needs to be calibrated either with and without the device inserted in it. The two calibrations are called respectively the *sphere calibration* and the *auto-absorption correction*:

- The sphere calibration is performed with no device mounted and using a special halogen lamp, the spectrometer and the SpectraSuite software. The used lamp is halogen because of the continuity of its spectrum, that is very near to the one of a black body. As

a matter of fact the halogen spectrum, in the wavelength region in which the spectrometer operates, is monotonically continous and this feature allows an accurate detection for all the wavelenghts. Furthermore the lamp's spectrum has been carefully measured by the producer and saved in the software: once the calibration lamp is applied to a suitable aperture on the sphere surface, its spectrum is registered and every difference between the measured and the provided one is reported in a special file, that will be read during the successive spectrum acquisitions. These differences are principally due to the reflective substrate imperfections, scale factors introduced by the fiber and the spectrometer, and the normal aging of the sphere.

- While the sphere calibration has to be done once a while, just to verify that the structural and optical characteristics of the apparatus are not significally changed, the auto-absorption correction must take place whenever a different lamp or, generally, lighting device is put inside the sphere. Indeed, while the sphere calibration gives a range of corrections due to perfectioning the reflection response of the sphere, the auto-absorption correction accounts for the light absorptions of the ballast of the lighting device that is put inside the sphere, and so it provides the corrections that should be applied to the final results, concerning that particular device.
  This calibration is performed turning off the device inside the sphere and mounting an auxiliary halogen lamp (different from the previous one) onto the aperture. The lamp is switched on and the final output from the fiber is registered once it is reached the steady-state spectrum. This result is written again in an apposite file, that must be read and compared with the results of the same measurement carried out with the calibration lamp mounted inside the sphere.

5.3.2 The USB2000 spectrometer

The USB2000 spectrometer, manufactured by Ocean Optics, is the device that provides the radiometric, photometric and color characteristics of the light source under test, and since its spectral range is declared to be from 350 to 1050 nm with a 2 nm spectral resolution, it well suits the measurements of LED devices.

In Figure 5.13 is reported a simple scheme of the spectrometer internal configuration, by which is possible to briefly explain its functioning.

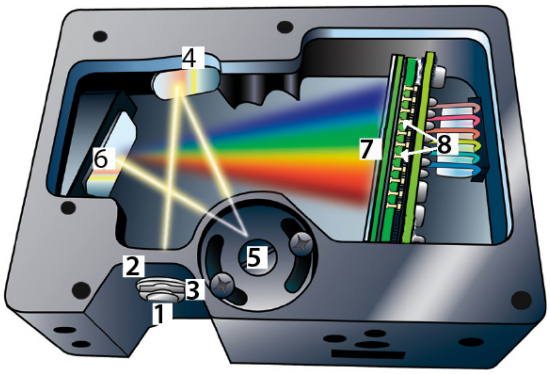

Figure 5.13: The USB2000 spectrometer optical bench scheme with its components: (1) the SMA connector, (2) the slit, (3) the optical filter, (4) the collimating mirror, (5) the diffraction grating, (6) the focusing mirror, (7) Detector Collection Lens and (8) the CCD detector. (Figure adapted from [18].)

1. The optical fiber is attached to the spectrometer via a **SMA connector**, that allows the light to go inside the optical bench.

2. After the SMA connector the light has to pass a rectangular aperture, the **slit**. The size of the aperture regulates the amount of light that enters the optical bench and controls spectral resolution.

3. An apposite **optical filter** can restrict, or generally regulate the spectral region of the light radiation, before it enters the optical bench.

4. As the light passes the SMA, the slit and the optical filter, it is focused by the **collimating mirror** towards the grating of the spectrometer.

5. The **grating** provides a diffraction of the light, that is redirected towards the focusing mirror. Notice that the diffraction can be apted in different ways and the gratings are available in different groove densities, allowing various wavelengths coverage and resolutions of the spectrometer.

6. The **focusing mirror** provides the last reflection before the CCD array, and it focuses the light onto the Detector Collection Lens.

7. The **Detector Collection Lens** is a lens array which is attached to the CCD detector and focuses the light onto the detector elements.

8. The **CCD Detector** is the only active part of the whole device, as it converts the optical signal to a digital signal. Notice that each of the 2048 pixels of the CCD corresponds to a wavelength of light that strikes it, so a single digital response is created for each detected wavelength.

The data acquisition from the CCD detector can be driven by the SpectraSuite software, but for our purposes it was used with Labview and the sourcemeter. As a matter of fact, the spectrometer disposes of an output USB channel which provides the optical data, and a secondary channel by which can be set the measurement trigger. This trigger has been actually set by the 2612.

The optical data obtained with these measurements are:

- the optical power, expressed in W and in lm;
- the efficacy, expressed in lm/W;
- the temperature color (CCT);
- the color rendering index (CRI);
- the chromatic coordinates x and y;

each of them has been measured for a sequence of forward currents, in most cases from 50 mA to 1.05 A with a 50 mA step, and are reported in Figure 5.14. Together with the optical measurements, the used software provides also some electrical information, very useful to verify the right functioning of the device:

- forward voltage;
- electrical absorbed power, that is obtained from the imposed current and measured voltage, and that allows the efficacy calculus;
- I-V measurement, made by a voltage bias and a current measurement;

Let's notice how all these measurements where made by the 2612 and the Switch Unit together, measuring one by one each LED on the same PCB inside the sphere.

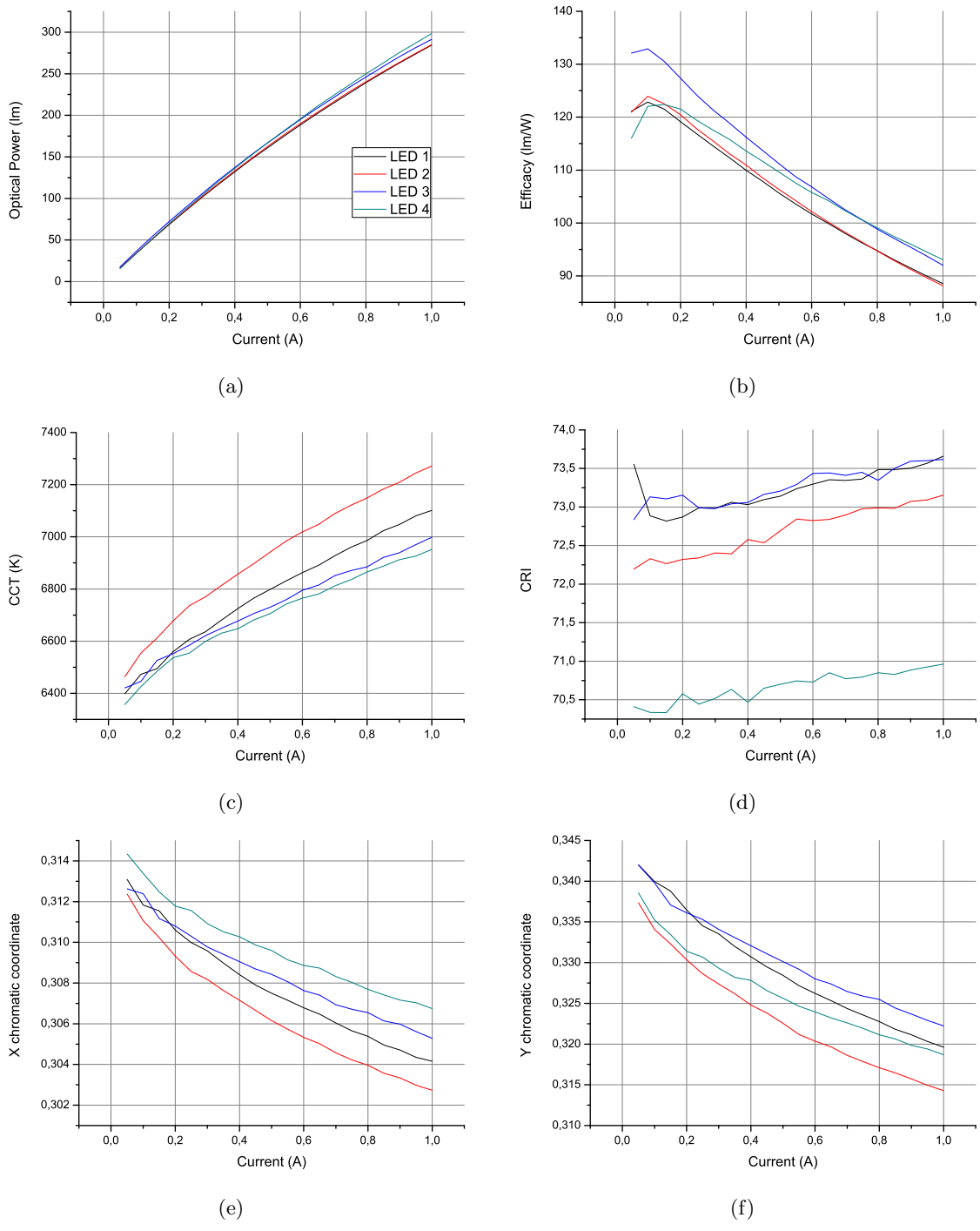

Figure 5.14: A set of measurements given by the optical characterization of the LEDs mounted onto the XPGA board, that has been done before the first hour of stress: (a) the optical power expressed in lm, (b) the efficacy, expressed in lm/W, (c) the Correlated Color Temperature (K), (d) the Color Rendering Index, (e) the x and (f) the y chromatic coordinates. The discussion of these plots is postponed to chapter 7.

CHAPTER 6

Devices setup and thermal characterization results

In this chapter the LEDs setup onto the MCPCB and the whole structure of the device that has been measured will be described, including the applied heatsink and the thermal interfaces. The results concerning the thermal characterization will be presented as well: these have been the most challenging issues because of the criticity of the thermal aspects and the disappointing thermal behaviour of the MCPCB, as it will be explained below.

Because of the thermal problems encountered in the first part of the work, the initially stated experimental procedure has been split into two parts, using in each of them a different type of PCB: in the former a simple MCPCB is adopted, in which the circuit has been ad-hoc designed and milled, while in the latter a different configuration is used, called *star* PCB, that is a simple commercial circuit board designed to provide the contacts to a single LED device.

We will see here how important is the thermal analysis, in order to qualify the stress capability of a certain LED device. Apart from the LED device itself, that presents an intrinsic thermal resistance from junction to solder point, the upper bound is often given by the MCPCB thermal resistance, and in particular by the thermal conductivity of the dielectric layer. As it will be analyzed in this chapter, this feature is the most critical in the quest of an optimum thermal flux from the junction to ambient: related works [19], [20]

tried to increase this conductivity involving special super conductors as diamond or creating special substrates under the thermal pad. These researches provide clear demonstrations of the dependence of the optical efficiency from the thermal management, and in particular from the junction temperature: as reported in Figure 6.1, the luminous flux can be definitely increased as the junction temperature is lowered, and once again this can be obtained only by a better management and design of the thermal properties of the whole LED lamp device.

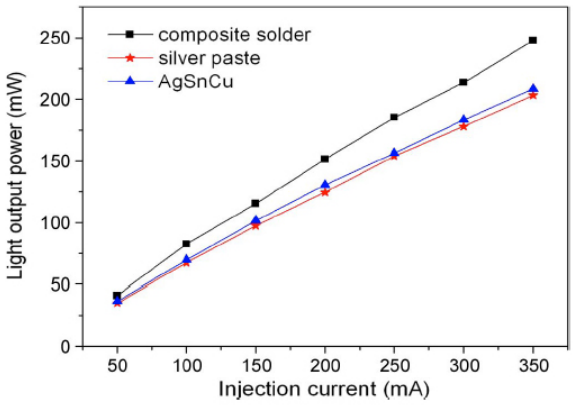

Figure 6.1: Light output power of LEDs solded to a MCPCB using a diamond-added composite solder, a mixture of silver and tin (AgSnCu), or a silver paste. The higher thermal conductivity provided by the diamond leads to a lowering of the junction temperature and an enhancement of the light output is obtained. (Figure taken from [19].)

6.1 The LEDs mounting onto the MCPCB

The electrical configuration of the devices inside the PCB is reported in Figure 6.2, while the photos of Figure 6.3 show the finally mounted LEDs : the four LEDs in the same PCB are connected in series, with an access to the anode and cathode of each one provided by a special contact. In order to provide a direct link to each LED , both for the sense and the force contacts, a 16-wires cable has been used. Since during the stress all the four LEDs onto a single board must be turned on, the series has been current-polarized. This polarization has been possible thanks to two wires connected to the LED 4 anode and LED 3 cathode.

The soldering of the LEDs is probably the more delicate procedure of the LED mounting, because of the tiny size of the packages and the proximity of the anode, cathode and thermal

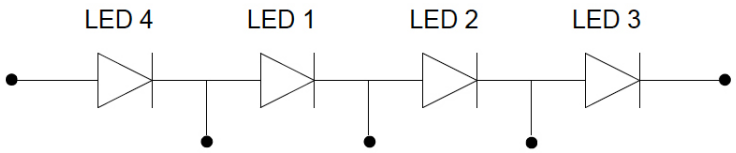

Figure 6.2: The setup of the LEDs devices inside the PCB.

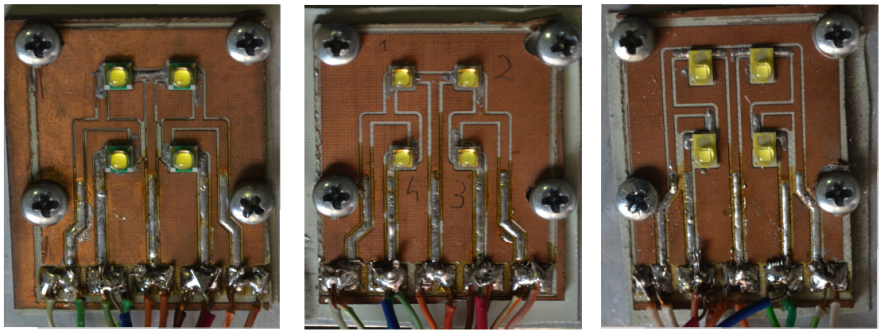

Figure 6.3: The three circuit boards with the LEDs mounted, (a) the XPGA board, (b) the OSLONA and (c) the REBELA.

pad, as reported in Figure 6.4. Initially the soldering was made by tin, that must be applied previously either on the LED contacts and on the printed footprint, and then, after placing the one over the other, a special oven provided a sufficient heat for the soldering. This had to be done for each LED on the same PCB and it soon revealed to be quite destructive for the LEDs that were overheated by the oven many times.

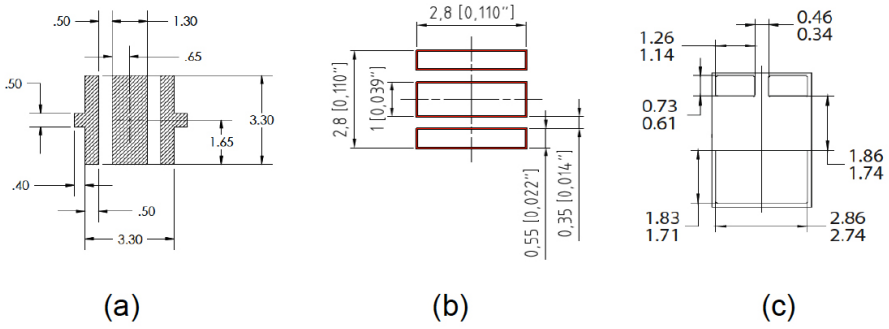

Figure 6.4: The recommended solder pads for the (a) XP-G, (b) OSLON and (c) REBEL LEDs , provided by [11], [12] and [13] respectively.

A second - and more efficient - procedure implies the use of a special soldering paste that, once put upon the contacts between the chip and the PCB, liquefies inside the oven and realizes the soldering. In this way the LEDs and the whole PCB are not overheated because of the small time that they passed into the oven (one minute and a half) and the temperature to which they are exposed (210 ^oC maximum). Once this procedure is completed, the LEDs are perfectly solded and can be still considered as virgin as before.

In order to obtain an effective mechanical and thermal contact between the MCPCB and the heatsink a thermal adhesive and four screws were used. This interface was not ever modified in the successive mountings, this guarantees the measurement reliability and repeteability.

The used heatsink, that is reported in Figure 6.5, consists of an aluminium block of about 600 g of weight, measuring $115 \times 60 \times 80$ mm and doted of a comb of ten plates in order to better dissipate the heat. In the first step a much thinner one was used, a simple aluminium plate measuring $50 \times 10 \times 5$ mm, but it revealed to be insufficient, indeed the LEDs were overheated and reached very high temperatures during the supertransients. The adoption of this bigger heatsink actually guarantees a very efficient heat dissipation.

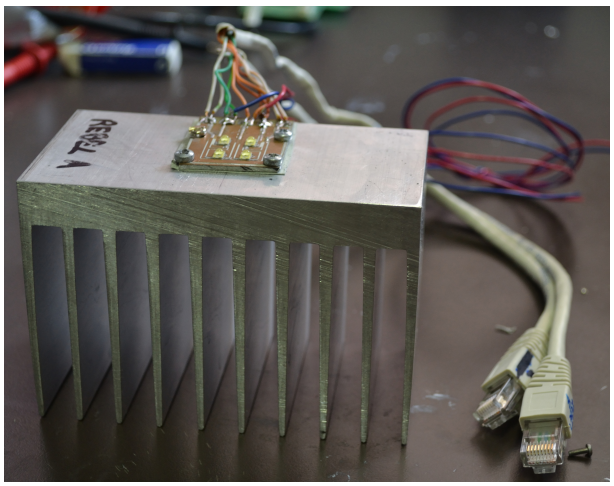

Figure 6.5: A photo of the whole mounted device, including the MCPCB over the heatsink and the cables used for the measurements.

The whole setup of the measured devices is represented in Figure 6.6: providing three different stress temperatures, and disposing of three sets of devices to analyze, a total of 36 LEDs were mounted onto nine PCBs.

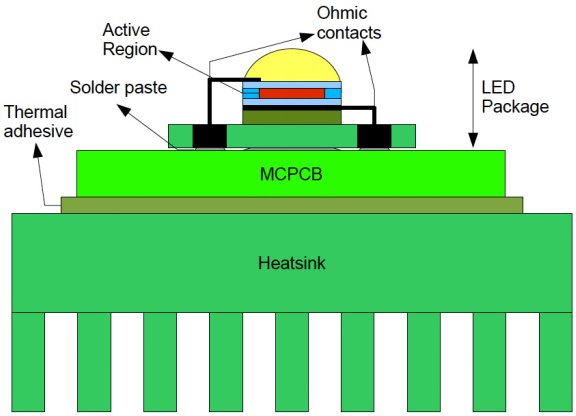

Figure 6.6: The final devices setup, highlighting the LED chip and all the introduced thermal interfaces in the thermal path from the active region to ambient. This figure is not in scale.

6.1.1 Technical data and thermal resistance of the MCPCB

The used MCPCB is manufactured by C.I.F., that provides in its website a detailed datasheet, where the dimensions, the thermal and electrical characteristics are explained. As represented in Figure 6.7, the MCPCB is made up of an aluminium base plate of 1.6 mm height, covered by an electrically-insulating dielectric layer of 76 μm and a standard-measure copper foil, of 35 μm. The aluminium base plate is used to reduce significally the thermal resistance of the circuit board, and to assure the best thermal transfer from the power devices placed over the board to the heatsink.

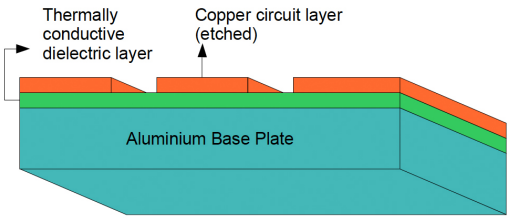

Figure 6.7: The structure of the used MC PCB.

The datasheets also declares the dielectric surface resistivity, 10^9 $M\Omega$, and its thermal conductivity, that is of 3 W/mK. This is a very high value, that should guarantee the best heat dissipation from a solded power device, but these data were not actually verified by our experimental results. In the next section the thermal features of this board are presented and critically described and even a comparative measure is reported, in which the same type

of LEDs mounted onto a different PCB were characterized.

6.2 The thermal characterization results

6.2.1 Thermal images of the mounted LEDs

Before the mounting process was completed, a preliminary evaluation of the thermal capability of the solded LEDs was made using the thermal camera, and the results are reported in Figure 6.8.

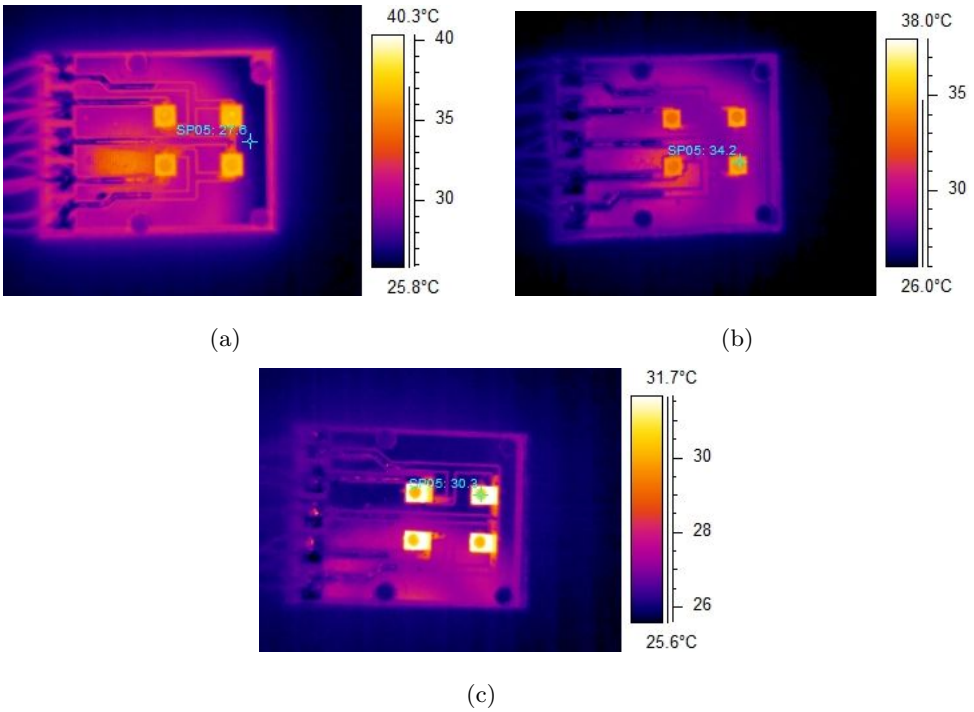

Figure 6.8: The images acquired with the thermal camera, representing (a) the XPGB, (b) the OSLONA and (c) the REBELA board, not yet mounted over the heatsink and driven at 200 mA.

In Figure 6.8 the temperature color scale is not the same onto the three images but there are not significant color differences among the four LEDs on the same PCB: this is actually a confirmation of the reliability and repetibility of the applied soldering process.

6.2.2 The thermal resistance evaluation

Both the thermal maps and the transients have been evaluated for a set of 13 forward currents, i.e. from 0.1 to 1.2 A with a 0.1 A step, including the 350 mA point to represent

the traditional operating current of such devices. As we will see in details in the plotted temperatures, the resulting trends are not perfectly linear, especially for high currents. Moreover for each PCB a more detailed description will be provided.

The XP-G thermal resistance

In Table 6.1 are reported the average thermal resistance R_{th}, its standard deviation $\sigma_{R_{th}}$ and the oven temperature T_{oven} found during the linear fitting of the Temperature-Power relation: the relative plots, realized for each of the A,B and C board, are reported in Figure 6.9.

	R_{th} (K/W)	$\sigma_{R_{th}}$(K/W)	T_{oven} (^oC)
XPGA	25.3	0.9	29.8
XPGB	26.2	1.2	29.8
XPGC	25.5	0.7	31.7
XPG	25.6	0.9 (3.7 %)	

Table 6.1: The thermal properties of the measured XP-G devices.

The manufacturer-declared thermal resistance from junction to solderpoint is of 4 K/W, while the average obtained resistance from junction to ambient is much higher, namely 25.6 K/W: this means, for instance, that a dissipation of 3 W leads to a thermal difference between the ambient and the junction of 3 $W \cdot 25.6\ K/W \simeq 75\ K$. As reported in the plots of Figure 6.9, considering an ambient temperature of 35 ^oC a junction temperature of 110 ^oC is found, which can be acceptable only if no other heating elements are present, such as other LEDs on the same PCB or an elevated ambient temperature[1].

The parabolic trend of those plots is probably due to the poor thermal performance of the used MCPCB: this assumption is confirmed by the characterization of the same LEDs mounted onto another PCB, as described in section 6.3. The non-linear trend reduces the reliability of the found R_{th}: future investigations should provide a reason for this unexpected dependence of the thermal resistance with temperature.

[1]Since the unitary step is the same either in the Celsius and in the Kelvin scale, the transposition between these relative temperatures is trivial. Moreover the thermal resistance is classicaly expressed in K/W, while the ambient temperature is expressed using the Celsius degrees scale.

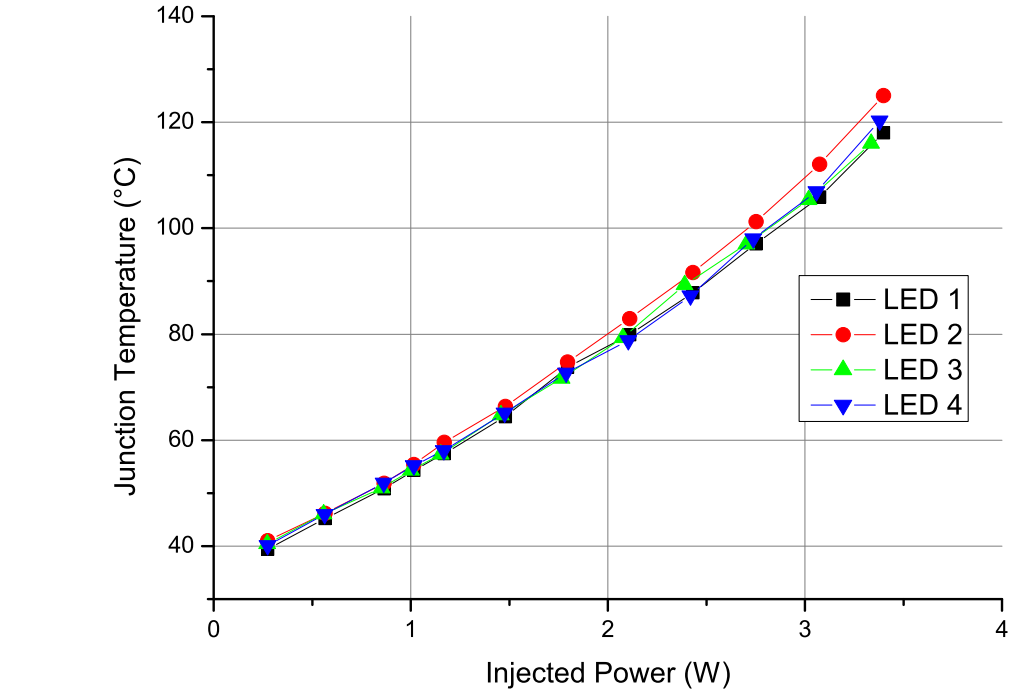

(a)

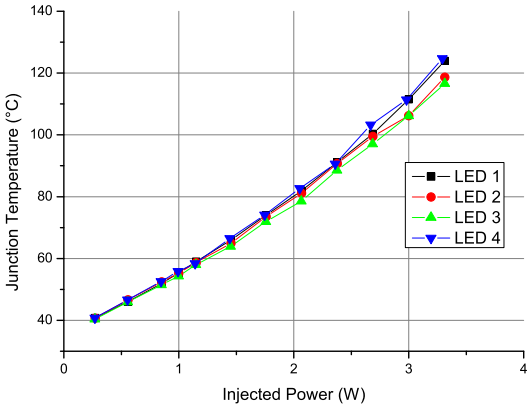

(b)

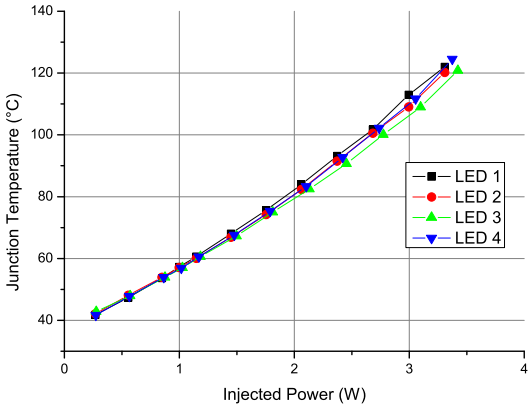

(c)

Figure 6.9: The junction temperature vs. injected electrical power of the (a) XPGA, (b) XPGB and (c) XPGC board. For each plot the trends of the four LEDs are provided, while in Table 6.1 is reported the statistics relative to each board. The results of the first PCB are emphasized, but the other two are analogous.

The OSLON thermal resistance

An analogous characterization has been done for the OSLON devices mounted onto the same CIF boards: the resulting thermal resistances are reported in Table 6.2, while in Figure 6.10 the plots of temperature versus power are provided.

	R_{th} (K/W)	$\sigma_{R_{th}}$(K/W)	T_{oven} (^oC)
OSLONA	38.7	2.8	25.7
OSLONB	36.3	1.8	28.9
OSLONC	34.9	1.8	31.3
OSLON	36.6	2.6 (7 %)	

Table 6.2: The thermal properties of the measured OSLON devices.

Comparing the thermal pads of the XPGs with those of the OSLONs, the bigger dimensions of the latter made expectable a more efficient heat exchange from junction to ambient, and this actually occurs: for the OSLON LEDs a larger thermal resistance has been calculated, of about $R_{th} \simeq 36\ K/W$. Because of the higher R_{th} and the tiny dimensions of this device, thermal issues are demonstrated to attend this device since the soldering work: as a matter of fact, this chip reached the higher junction temperature during stress and its optical behaviour was pretty much influenced by overheating problems.

Even in this case the temperature-power dependence is not linear, for example the acquired data in the LED 3 of the OSLONA board are pretty uncertain, and then unreliable, for high currents. The uncertainty of the actual achieved temperature must be taken into account during the stress operation design, as we will see in the next section. Nevertheless only the OSLON LED has demonstrated such deficit, that is again probably due to the poor thermal removal performances of this device.

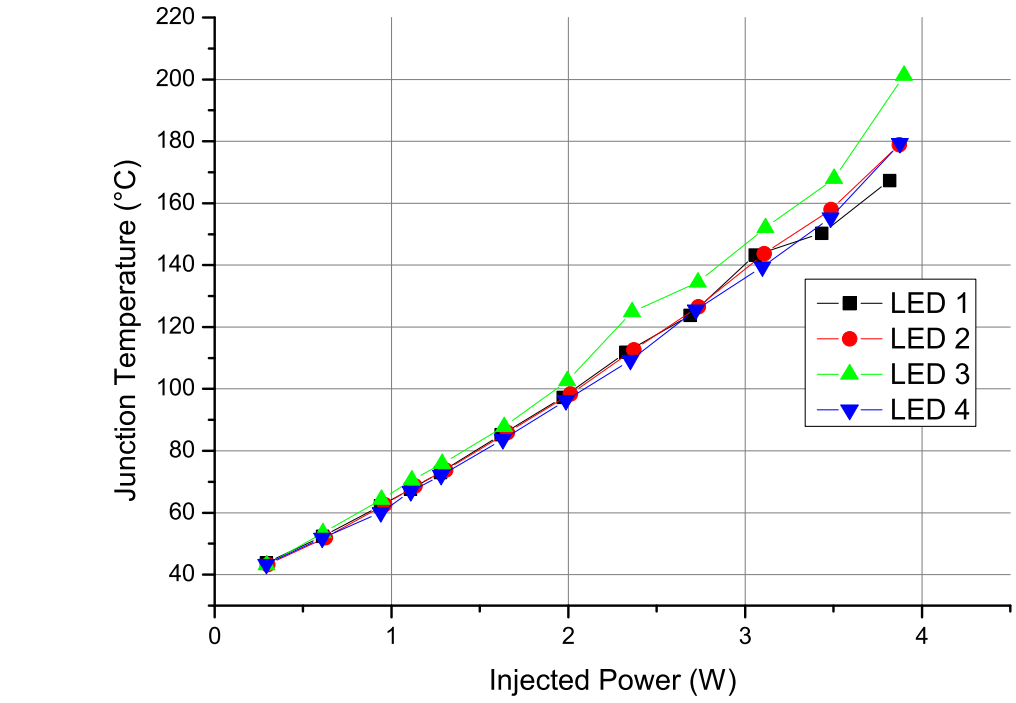

(a)

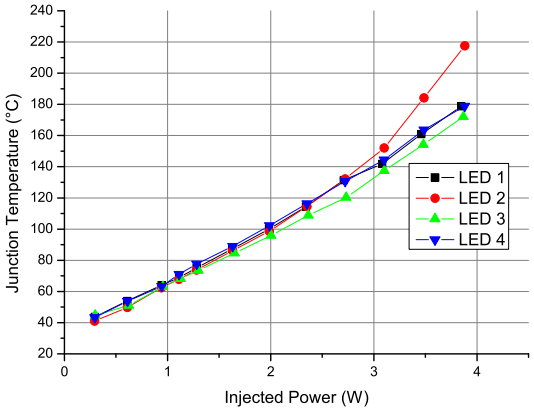

(b)

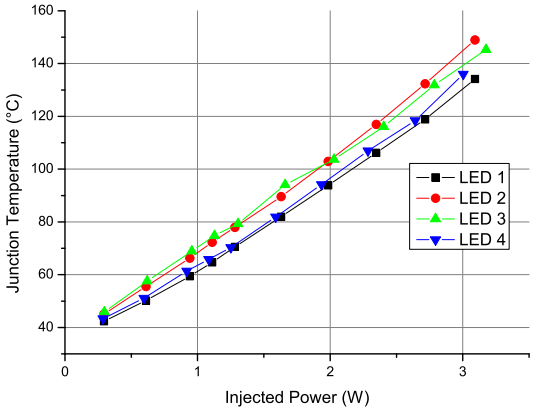

(c)

Figure 6.10: The junction temperature vs. injected electrical power of the (a) OSLONA, (b) OSLONB and (c) OSLONC board. For each plot the trends of the four LEDs are provided, while in Table 6.2 is reported the statistics relative to each board. The results of the first PCB are emphasized, but the other two are analogous.

The REBEL thermal resistance

The REBEL thermal performances are reported in Table 6.3 while the plots of the junction temperature versus electrical power are shown in Figure 6.11. Comparing the table with the previous ones we notice that the thermal resistance of the REBEL device is the highest and the most unreliable as well, since its standard deviation is of 7.6 %: this variability is relative of the statistics of all the LEDs of the three PCBs, and is higher then the one of the OSLON, that is high as well, and the XPG's, the lowest and even the more thermally-performant among the chips considered.

	R_{th} (K/W)	$\sigma_{R_{th}}$ (K/W)	T_{oven} (^oC)
REBELA	43.2	1.9	27.4
REBELB	37.4	1.8	29.5
REBELC	39.3	2.1	32.8
REBEL	40.0	3.0 (7.6 %)	

Table 6.3: The thermal properties of the measured REBEL devices.

Observing the plots and in particular their parabolic trend and the irregularity of measurements for high currents, analogous considerations are possible, as . Since this device is the most thermically resistive, we can approximately evaluate its junction temperature at, for example, a forward current of 1 A and an ambient temperature of 25 ^oC: considering $R_{th} = 40\ K/W$ and that for $I = 1\,A$ the average measured voltage provided by the transients is $V = 3\ v$, we obtain an injected power of $P = 3\ W$. Noticing that the plots correspond to an ambient temperature of 35 ^oC, a junction temperature of about 150 ^oC is retrieved, which is beyond the maximum operating temperature of 135 ^oC declared by the manufacturer.

The REBEL footprint, as represented in Figure 6.4, seems to be optimized from the thermal point of view, since the thermal pad is fairly separated from the electrical contacts, the pad is the larger among the ones considered (see Table 6.4) and it is right below the chip. Despite of all these sagacities the obtained complexive thermal resistance is the highest among the considered devices.

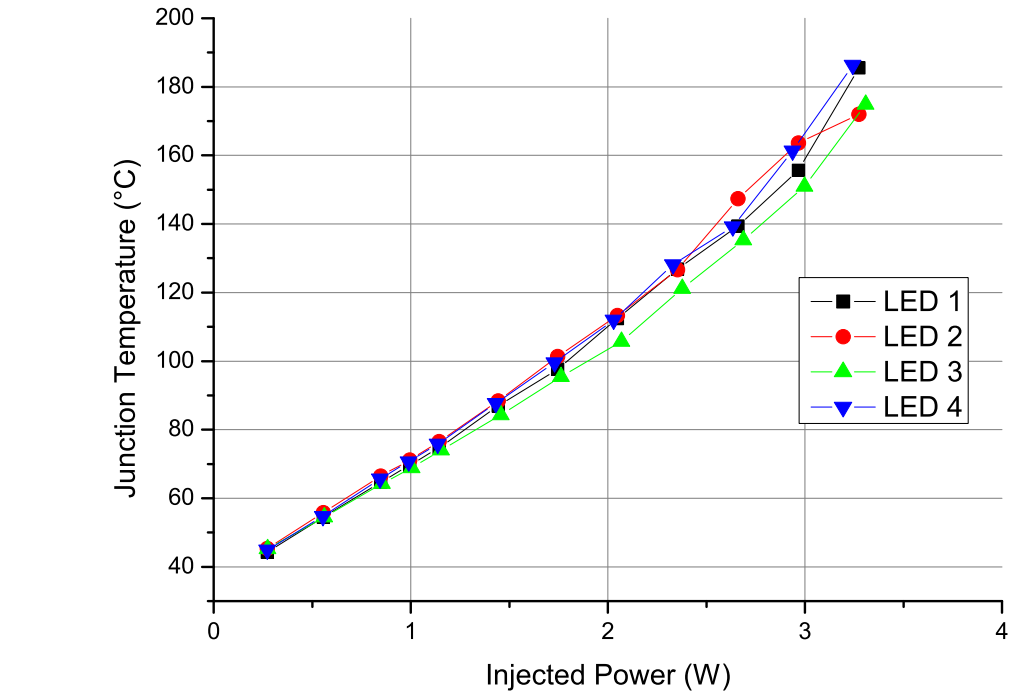

(a)

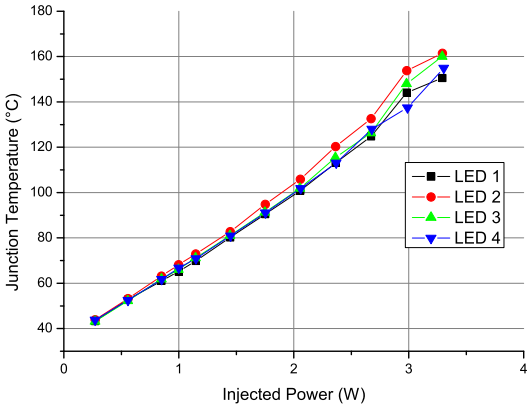

(b)

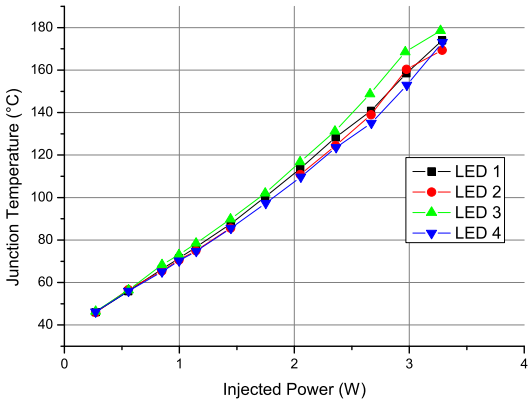

(c)

Figure 6.11: The junction temperature vs. injected electrical power of the (a) REBELA, (b) REBELB and (c) REBELC board. For each plot the trends of the four LEDs are reported, while in Table 6.3 is reported the statistics relative to each board. The results of the first PCB are emphasized, but the other two are analogous.

Comments on results

The thermal characterization, whose results are summarized in Table 6.4, underlines the following two aspects:

- the thermal behaviour of the used MCPCB is evidently not as performant as the datasheet states, since the declared high thermal conductivity of the dielectric substrate has not been confirmed by our thermal measurements: this mismatching could be verified only measuring the same set of LEDs mounted onto a different PCB, as explained in section 6.3. Even the parabolic trend of the plots is probably due to the PCB: future challenges should consider a more accurate characterization of the thermal behaviour of this kind of PCB;

- since the used PCB is the same for all the LEDs sets analyzed, and despite of the high found R_{th}, the results of the thermal characterization complessively follow the manufacturer-provided data. The best thermal behaviour is provided by the XP-G LED that, doted by a very little area onto the thermal pad, presents the lower thermal resistance with the lower statistical uncertainty in its determination. The worst thermal performance is given by the REBEL LED , which presents a very high thermal resistance althought the thermal pad area is the bigger: this poor heat removal is probably due to internal chip design issues.

	R_{th} (K/W)	$\sigma_{R_{th}}$ (%)	R_{thj-sp} (K/W)	A_{th} (mm^2)
XPG	25.6	3.7	4	3
OSLON	36.6	7	7-9.4	2.7
REBEL	40.0	7.6	10	5.3

Table 6.4: The complexive basic results of the thermal characterization, for the three different LEDs types, including the statistical uncertainty, the thermal resistance from junction to solder point and the thermal pad area, as provided in their respective datasheets [11], [12] and [13].

Once the thermal maps are done, the next step consists in measuring the junction temperature with the device operating at different ambient temperatures, via the supertransients measurements. Because of the very high temperature that they could reach during a high-current operation, and in order to avoid the device overrun, we stressed them at a low current

but maintaining a high temperature: such evaluations have been done during the first hour of operations, and their results are reported in the next section.

6.2.3 The supertransients and the junction temperature evaluation

Since the devices at the forward current of 1 A reached very high temperatures, that could be very destructive during stress, we initially chose to inject a current of 700 mA, and to impose a moderate temperature, without using the 85 ^oC oven. Disposing of three PCB for each kind of LED and thus having to choose among three different temperatures, we considered to stress one set of PCBs at the ambient temperature, the second inside the oven at a temperature of 45 ^oC and the last one with the oven set at 65 ^oC.

The first hour of stress was dedicated to the superstransients measurement and to the calculation of the junction temperature in these stress conditions. Recalling that during the stress the PCBs were connected three-by-three in series and thus all the LEDs in the same PCB were turned on, we must consider that the measured temperatures are comprehensive of the mutual heating of the LEDs .

Once the transients of the board stressed at ambient temperature and of the ones put inside the oven at 45 ^oC were measured and the junctions temperatures were calculated, we found that something was wrong: these temperatures are reported in Table 6.5, and we notice that they are similar, this reveals that if the stress, that was yet running the 64th hour, was done in those conditions there would be two sets of LEDs stressed in the same way. Analyzing more in detail the problem, we found that the lack of ventilation in ambient temperature conditions radically influenced the heat removal dynamics during the LEDs operation, thus the devices were actually overheated.

A more detailed investigation brougth us to realize another set of supertransients, inside the oven and at a temperature very near to the ambient one, of 30 ^oC. The results for the three boards, that are reported in Figure 6.12, clearly explain the situation: the devices stressed at ambient temperature, where evidently no ventilation is provided, suffer of a slower thermal exchange (as represented by the transients trend), so that the LEDs were eventually overheated and the perceived ambient temperature was not 25 ^oC but very near to 45 ^oC.

This fact led us to consider the use of the third oven with a settled temperature of 85 ^oC. In this case a proper appuration of the junction temperature were necessary, in order not to waste the devices: the actual temperatures were in most cases right below 200 ^oC, as shown

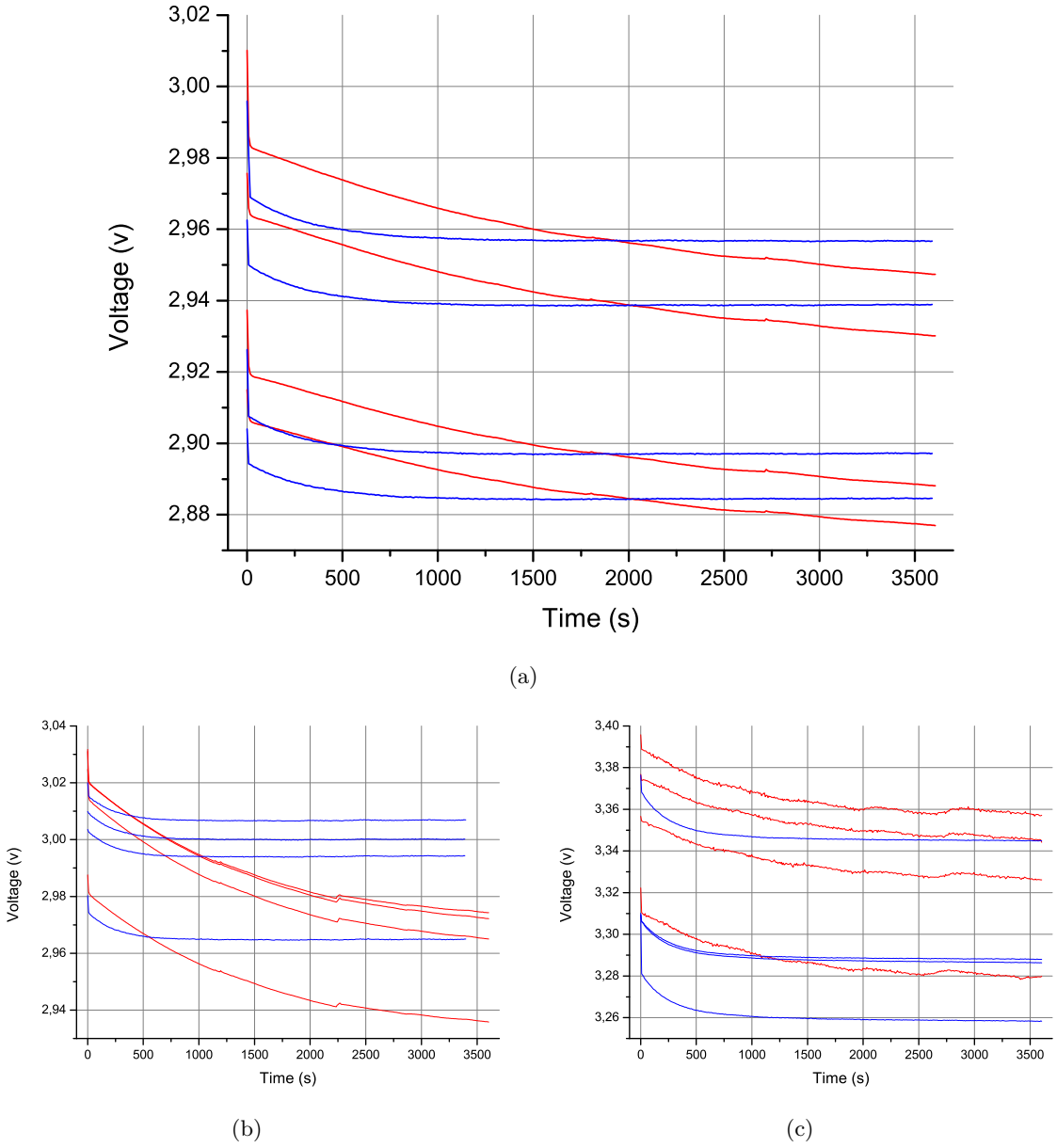

Figure 6.12: The supertransients realized maintaining the LEDs at ambient temperature of approximately $25\ ^{o}C$ (red track) and inside a ventilated oven at $30\ ^{o}C$ (blue). The plots refer to the (a) REBELA, (b) XPGA and (c) OSLONA PCBs and underline the different heat-exchange kinetics in the two cases.

in the last row of Table 6.5, and did not exceed too much the manufacturer's suggested limit, so these stress conditions revealed to be a good trade off to achieve a significant degradation of the devices without destroy them.

T_{oven}	XPG	OSLON	REBEL
Ambient (A series)	98 (4.8)	98 (4.8)	98 (4.8)
30 (A series)	85 (3.5)	131 (17.4)	120 (6.1)
45 (B series)	105 (4.8)	141 (15.3)	124 (5.1)
65 (C series)	135 (7.4)	155 (8.9)	169 (7.7)
85 (A series)	160 (11.2)	208 (25.7)	176 (8.3)

Table 6.5: The junction temperatures provided by the supertransients analysis, expressed in ^oC. In parenthesis the standard deviation is indicated, that has been calculated for the four LEDs of each considered PCB. The temperatures relative to an oven temperature of $30\ ^oC$ and $85\ ^oC$ are calculated from 64-hours stressed devices, for which the thermal maps were re-measured. It is useful to recall the junction temperature limit for each led, that is 150, 125 and $135\ ^oC$ for the XPG, OSLON and REBEL LEDs respectively.

In Table 6.6 are reported some calculations about the temperature that each LED is expected to reach once it is biased by a current of $I = 700\ mA$ and at certain ambient temperature. Notice that in the final results, that should be close to the values found with the supertransients, the mutual heating of the LEDs onto the same PCB was not taken into account: as a matter of fact this quantity, that is not simple to estimate, should be the actual difference between the theoretical predictions and the experimental results.

6.3 Thermal characterization of LEDs onto a different PCB

In order to clarify the reasons of the poor heat performance of the measured devices, a thermal characterization has been conducted onto two different types of PCB, which presented an aluminium depth of 1.1 and 2.2 mm respectively, and the mounted devices were the XP-G. The applied mounting procedure, the LEDs configuration onto the PCB, the used thermal adhesive and the heatsink are the same in each case. The results, that will be explained in the next two sections and that are summarized in Table 6.7, points out that the used PCB during stress was not actually adequate for our purposes, in particular it was probably a photosensitive PCB that should not be milled.

This second set of MCPCBs was a brand new type, provided by a free sample trial: unluckily no additional information about the dielectric layer thickness and its thermal conductivity was available.

	XPG	OSLON	REBEL
R_{th} (K/W)	26.6	36.6	40.0
Power @ 700 mA (W)	2.8	2.35	2.06
Relative T_j (^oC)	55.6	86.0	82.3
Absolute T_j @ $T_{oven} = 65\ ^oC$	120	151	147

Table 6.6: The evaluation of the junction temperature T_j, firstly referring only to the thermal resistance and power value and so retrieving the relative temperature, then adding the ambient temperature, that is provided by each oven configuration and renders the absolute junction temperature. The power has been calculated averaging all the 12 measurements from the same PCBs: the evaluated values are pretty reliable because of the low standard deviation, that is below the $2\ \%$. In the last row is listed only the temperature relative to $T_{oven} = 65\ ^oC$, in the other two cases it can be found simply adding or subtracting $20\ ^oC$.

The $1.1\ mm$ board

For the devices mounted onto this board the thermal investigation was conducted in the same way of the previous ones, and is characterized by a junction-to-ambient thermal resistance of $R_{th} = 14.1\ K/W$, with an accuracy of $0.34\ K/W$. The plot of the junction temperature versus the injected power is reported in Figure 6.13.

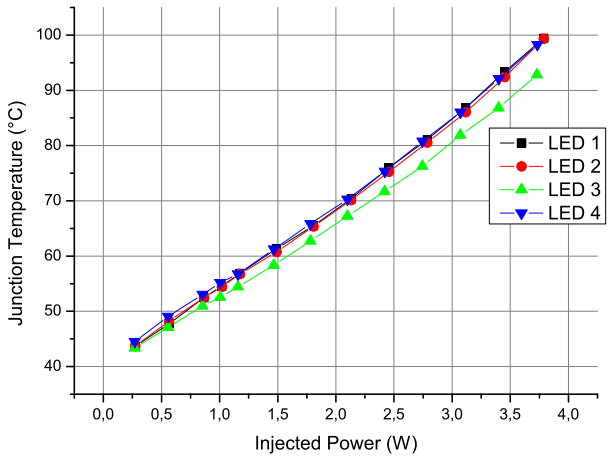

Figure 6.13: The temperature - power plot for the four LEDs provided by the thermal characterization of the $1.1\ mm$ PCB.

The 2.2 mm board

The larger thickness of this PCB should let us expect a better thermal performance and so a lower thermal resistance. By the way the measurements reported a value of $R_{th} = 15.1\ K/W$, with a standard deviation of 0.64 K/W among the four LEDs . These results lead us to conclude that, because of the little uncertainty found, the two PCBs are very similar, but the former is less performant than the latter, probably because of the more direct and fast thermal contact that the thinner one provides to the heatsink.

In the second case the plots are reported in Figure 6.14. The nearly-linear trend of this plot and of the 6.13 ones is to note, and moreover the difference of these ones from the previoulsy calculated, in which the trend was nearly parabolic. In this case the plots can be easily and more accurately linearly fitted, while the old ones were distorted and less reliable, as it has already been discussed.

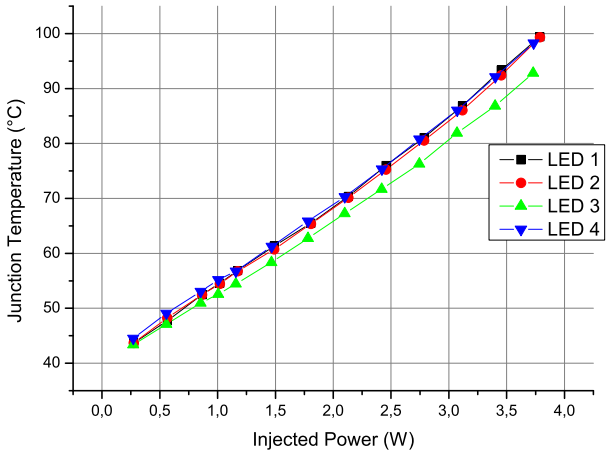

Figure 6.14: The temperature - power plot of the four LEDs provided by the thermal characterization of the second an more thick PCB.

6.3.1 The performance of the 1.1 and 2.2 mm PCBs

In Table 6.7 the results concerning the thermal characterization of the first and the second PCB and the results of the old investigation on the ones used during stress are provided.

After this detailed analysis the thermal performance of this brand new PCB we consider the use of a different mounting board, such as the *star* PCB, in order to achieve a better thermal management during stress and so stressing the devices in more extreme conditions,

	1.1 mm PCB	2.2 mm PCB	old PCB
R_{th} (K/W)	14.1	15.1	25.6
$\sigma_{R_{th}}$ (K/W)	0.34 (2 %)	0.64 (4 %)	0.9 (4 %)
Relative T_j (^oC) @ 700 mA	29.3	31.4	55.6

Table 6.7: The comparative summary of the results for the 1.1 mm and 2.2 mm boards and the report of the old results. Also the relative calculated temperatures for the operation at 700 mA of the LEDs are reported. Notice that these temperatures are relative to an ambient temperature of 0 ^oC. Comparing the new to the old results leads to a difference of about 25 ^oC between the two, thus an hypotetic stress would probably involve higher currents injection.

for example feeding them at a higher forward current. In the next section the mounting of the LEDs onto the stars will be described, and the relative thermal characterization results will be critically discussed.

6.4 The use of the star MCPCB

In order to provide a better thermal management during stress operation than the one presented by the previously used PCB, a mounting of the same set of LEDs on the stars were done. The adopted thermal interfaces were the same, as well as the heatsink: the only difference was the mounting basis and the disposition of the LEDs on it. Notice that, since each LED disposed of a single star PCB, the thermal analysis during the supertransients will be pretty different from the previous case, because of the minor thermal interface condivision among the LEDs and so the lower mutual heating that they could suffer.

6.4.1 The star structure

The used star PCB were produced by OPULENT and are represented in Figure 6.15. Apart from the footprint, that is obviously designed for each of the solded LEDs , the stars present all the same features, such as a dielectric thermal conductivity of 1.8 W/mK and a thickness of 0.1 mm, layered over a 1.5 mm thick aluminium foil. In order to obtain the same circuit disposition of the previous measured PCB, the stars have been connected in series onto the heatsink, as represented in picture 6.16. The same electrical scheme of figure 6.2 was reproduced and the LEDs could be measured one by one with the same software and

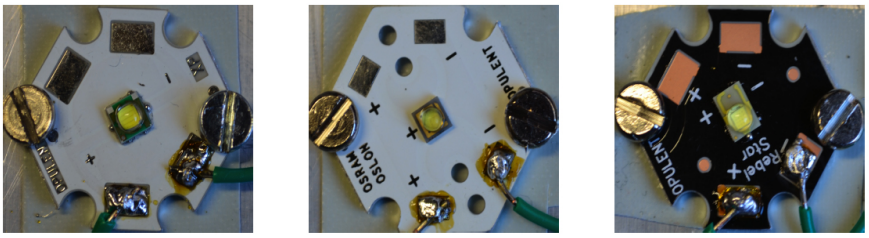

(a) (b) (c)

Figure 6.15: The three star boards with the LEDs mounted, (a) the XPGA, (b) the OSLONA and (c) the REBELA.

turned on all together by the serial connection.

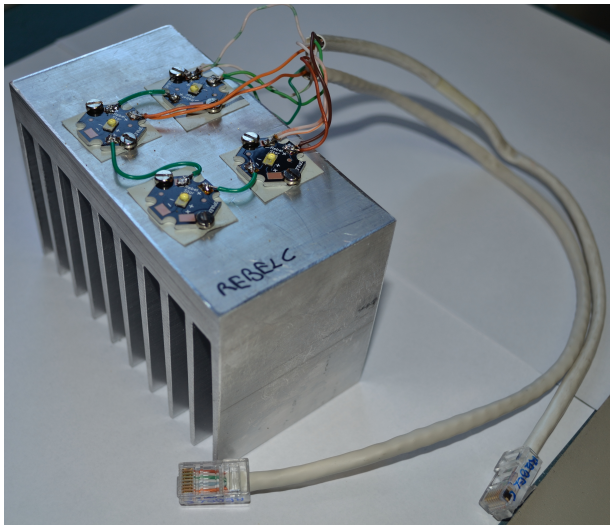

Figure 6.16: A picture of the REBELC mounted device: the setup is the same of the previous case, notice the disposition and connection of the stars onto the heatsink, and the same used thermal adhesive.

6.4.2 The thermal characterization results

The results provided by the thermal characterization of the devices mounted onto the star MCPCB are reported in Table 6.8, while in Figure 6.17 are reported the plots of the junction temperature versus power. These plots differ from the ones found in the previous case in the linear trend and in the greater homogeneity of the results, that indicate the major level of reliability of this second set of measurements: this observation is also confirmed by the lower

standard deviation values reported in Table 6.8.

Since the obtained plots are very similar, just one plot for each kind of device is reported.

	R_{th} (K/W)	$\sigma_{R_{th}}$ (K/W)	T_{oven} (^oC)
XPG	12.7	1.1 (8 %)	32.4
OSLON	18.0	1.7 (9 %)	30.3
REBEL	14.7	1.0 (7 %)	32.5

Table 6.8: The thermal results of the star devices. The values are the average of all the twelve LEDs of the same type.

These results partially confirm the comments done in the previous case: the R_{th} provided by the XP-G LEDs is always the lowest among the ones considered, but in this case the role of the OSLON and REBEL devices is inverted: the Luxeon's LED presents a lower thermal resistance than the Osram's one, and it is even the more accurate. A review of the past results also confirms the better thermal behaviour of REBEL, since the results were as near as the found standard deviation could compare them. These values are the lowest found until now, and they are pretty satisfactory for our purposes.

6.4.3 The supertransients and the temperatures during stress

Because of the superior thermal performance of this kind of board, a higher stress current can be chosen: the supertransients were done at 1.2 A bias and revealed the temperatures reported in Table 6.9.

T_{oven} (^oC)	XPG	OSLON	REBEL
45 (A series)	102 (1.0)	146 (24.9)	125 (16.9)
65 (B series)	130 (5.3)	151 (14.5)	154 (11.6)
85 (C series)	150 (5.7)	177 (20.7)	174 (20.5)

Table 6.9: The junction temperatures provided by the supertransients analysis, expressed in ^oC. In parenthesis the standard deviation is indicated.

In this table the higher reliability of results concerning the XPG board, and the high dispersion in the temperatures of the OSLON ones are noticeable. This uncertainty, present

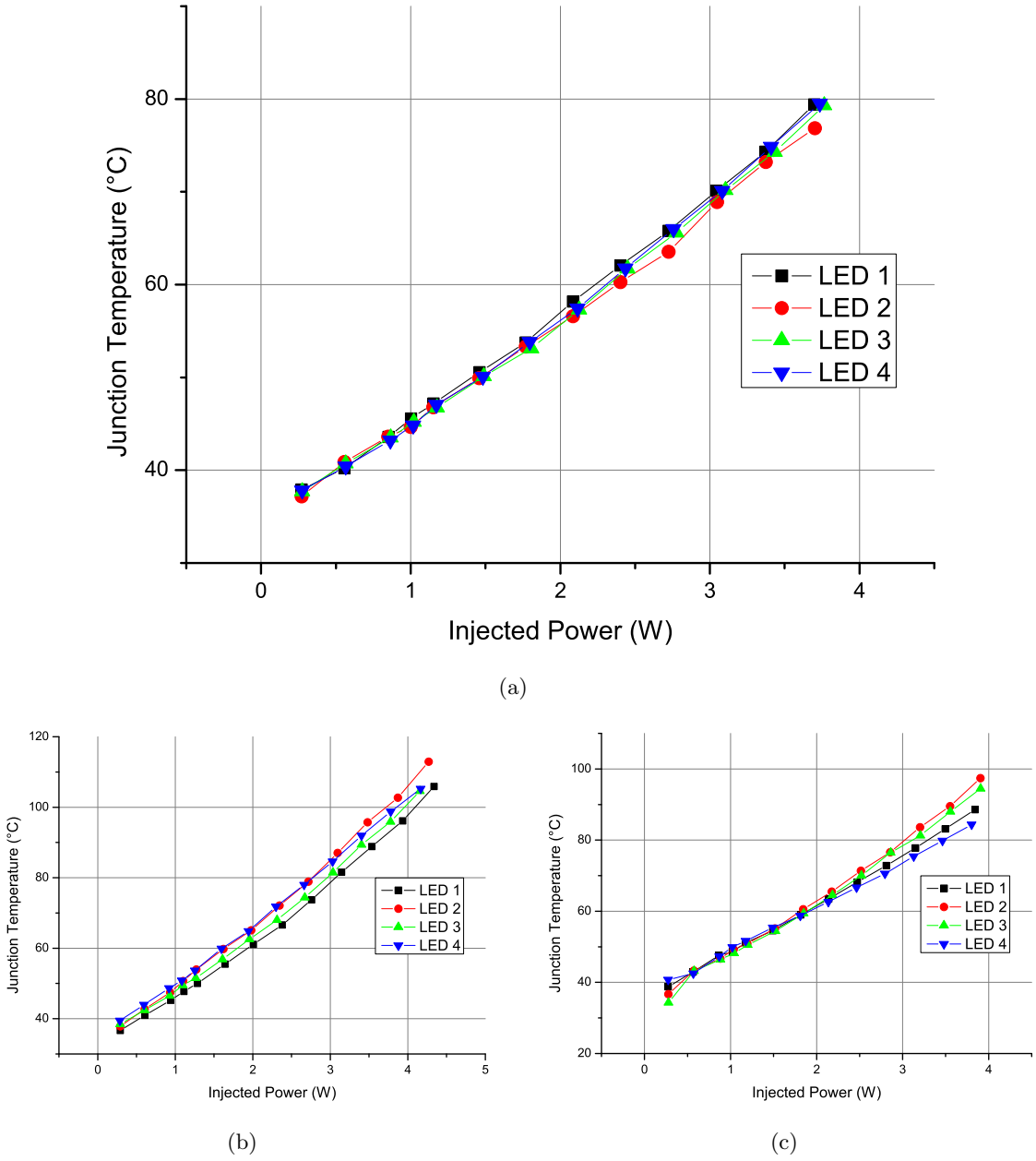

Figure 6.17: The junction temperature vs. electrical power of the (a) XPGA, (b) OSLONA and (c) REBELA board. The plots are found using the thermal maps and transients from the thermal characterization, and the junction temperatures are to be referred to an ambient temperature of 35 ^oC.

in particular in the OSLONA and OSLONC series, comes with a lowering of the average temperature, which seems to be pretty similar in the 45 and 65 ^oC cases. In order to find out the temperature increase due to the mutual-heating of the four LEDs onto the same heatsink,

Table 6.10 reports a brief computing of the expected temperatures that have been evaluated as if each LED was turned on, with the data found during the thermal characterization.

	XPG	OSLON	REBEL
R_{th} (K/W)	12.7	18.0	14.7
Power @ 1.2 A (W)	3.7	4.2	3.9
Relative T_j (^oC)	47	77	57
Absolute T_j @ $T_{oven} = 65\ ^oC$	112	142	122

Table 6.10: The evaluation of the junction temperature T_j, relative to an ambient temperature of $T_{oven} = 65\ ^oC$. The data about the thermal resistance and injected power are the ones provided by the thermal characterization

Comparing this table with Table 6.6 it is easy to notice the lower reached temperature, thanks to the lower thermal resistance, even with a higher forward current.

Observing Table 6.9 one can notice that the difference is just due to the mutual heating effect: as a matter of fact, the heating of each LED is influenced by the other as much as the previous case. The different disposition of the devices and the effective condivision of the heatsink does not influence too much the thermal separation of each LED , since the heatsink, that is heated by the whole series of LEDs lighted upon, represents a thermal barrier that still prevent an optimal flux from the PCB to the ambient, as it would happen if each LED was singly turned on.

Eventually, the thermal characterization details and in particular the found temperatures led us to perform a high-current stress, thus the devices are aged at the three temperatures with an injection of 1.2 A current. Notice that the stressing of the devices, that was previously done by a high temperature level, is obtained in this case by imposing a medium temperature - still higher than the recommended one - but a very high current. The results of this operation would finally yield to certain considerations that should obviously take into account these conditions, but also be comparative with the results obtained with the previous high-temperature stress.

6.5 The comparison of the two stress conditions

Since in most cases the temperature acts a fundamental role in the ageing of a LED device, a proper comparison of the two processes yet explained is necessary. As a matter of facts, the conducted thermal analysis revealed that the temperature conditions are pretty similar for the two experiments, because, thanks to the lower thermal resistance of the second set of PCBs, the higher current injection is possible and the temperature is still near to the one reached in the first case, where the high temperature was caused by the high thermal resistance. In Table 6.11 are reported the average temperatures reached in the two cases, while a more immediate analysis is provided by the histograms reported in Figure 6.18.

LED Name	T_{amb} (^oC)	T_j (σ_{T_j}) @ 700 mA	T_j (σ_{T_j}) @ 1.2 A
XPG	45	105 (4.8)	102 (1.0)
XPG	65	135 (7.4)	130 (5.3)
XPG	85	160 (11.2)	150 (5.7)
OSLON	45	141 (15.3)	146 (24.9)
OSLON	65	155 (8.9)	151 (14.5)
OSLON	85	208 (25.7)	177 (20.7)
REBEL	45	124 (5.1)	125 (16.9)
REBEL	65	169 (7.7)	154 (11.6)
REBEL	85	176 (8.3)	174 (20.5)

Table 6.11: The junction temperature in ^oC measured through the supertransients, for all the devices submitted to the two kinds of stress. Each value is the average of the four LEDs in the same PCB, and in parenthesis also the standard deviation is reported.

The temperatures and the thermal resistances obtained are estensively reported in Table 6.12 and 6.13 for the LEDs mounted onto the MCPCBs and the star PCBs respectively. From these values the mentioned averages and plots have been obtained.

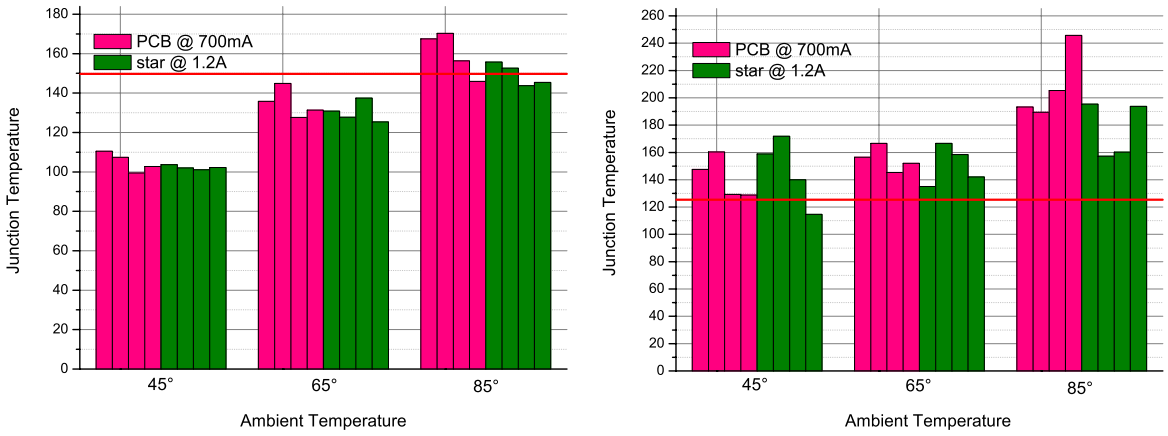

(a) XP-G

(b) OSLON

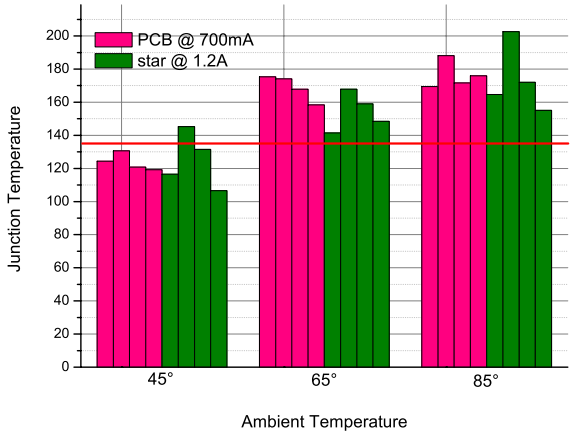

(c) REBEL

Figure 6.18: The junction temperature reached during the supertransients in each LED and the maximum temperature declared by the manufacturer (red line). For a certain ambient temperature the difference between the temperatures of the PCBs (stressed at $700\ mA$) and the star (operating at $1.2\ A$) are put in evidence.

LED Name	R_{th}	T_{amb}	T_j
PCB_XPGB_1	26.94	45	110.5
PCB_XPGB_2	25.40	45	107.4
PCB_XPGB_3	24.94	45	99.5
PCB_XPGB_4	27.41	45	102.8
PCB_XPGC_1	25.93	65	135.8
PCB_XPGC_2	25.50	65	144.9
PCB_XPGC_3	24.51	65	127.6
PCB_XPGC_4	26.23	65	131.4
PCB_XPGA_1	24.82	85	167.5
PCB_XPGA_2	26.58	85	170.3
PCB_XPGA_3	24.68	85	156.4
PCB_XPGA_4	24.99	85	145.9
PCB_OSLONB_1	37.85	45	147.5
PCB_OSLONB_2	34.21	45	160.4
PCB_OSLONB_3	35.45	45	129.3
PCB_OSLONB_4	37.87	45	128.8
PCB_OSLONC_1	33.46	65	156.5
PCB_OSLONC_2	37.41	65	166.6
PCB_OSLONC_3	33.81	65	145.3
PCB_OSLONC_4	35.04	65	152.0
PCB_OSLONA_1	35.68	85	193.3
PCB_OSLONA_2	39.77	85	189.4
PCB_OSLONA_3	42.10	85	205.4
PCB_OSLONA_4	37.21	85	245.7

LED Name	R_{th}	T_{amb}	T_j
PCB_REBELB_1	36.03	45	124.4
PCB_REBELB_2	39.57	45	130.7
PCB_REBELB_3	38.22	45	120.8
PCB_REBELB_4	35.92	45	119.2
PCB_REBELC_1	39.54	65	175.3
PCB_REBELC_2	38.34	65	174.1
PCB_REBELC_3	42.15	65	167.8
PCB_REBELC_4	37.24	65	158.4
PCB_REBELA_1	43.21	85	169.4
PCB_REBELA_2	43.37	85	188.1
PCB_REBELA_3	40.77	85	171.6
PCB_REBELA_4	45.37	85	176.0

Table 6.12: The thermal resistance and the junction temperature obtained for each single LED , mounted on the MCPCB and operating at $700\ mA$ and at the reported ambient temperature.

LED Name	R_{th}	T_{amb}	T_j
star_XPGA_1	12.10	45	103.7
star_XPGA_2	11.46	45	102.0
star_XPGA_3	11.87	45	101.1
star_XPGA_4	12.11	45	102.2
star_XPGB_1	14.92	65	130.8
star_XPGB_2	12.33	65	127.7
star_XPGB_3	13.89	65	137.5
star_XPGB_4	12.51	65	125.4
star_XPGC_1	14.41	85	155.7
star_XPGC_2	12.45	85	152.6
star_XPGC_3	12.12	85	143.8
star_XPGC_4	11.97	85	145.4
star_OSLONA_1	16.91	45	158.9
star_OSLONA_2	18.67	45	171.9
star_OSLONA_3	17.06	45	140.0
star_OSLONA_4	17.22	45	114.6
star_OSLONB_1	18.68	65	135.0
star_OSLONB_2	22.77	65	166.6
star_OSLONB_3	17.88	65	158.5
star_OSLONB_4	17.22	65	142.0
star_OSLONC_1	18.65	85	195.4
star_OSLONC_2	16.72	85	157.2
star_OSLONC_3	17.82	85	160.2
star_OSLONC_4	16.73	85	193.8

LED Name	R_{th}	T_{amb}	T_j
star_REBELA_1	13.73	45	116.5
star_REBELA_2	16.10	45	145.2
star_REBELA_3	15.74	45	131.5
star_REBELA_4	12.40	45	106.6
star_REBELB_1	14.78	65	141.4
star_REBELB_2	14.41	65	167.9
star_REBELB_3	14.94	65	159.0
star_REBELB_4	15.21	65	148.5
star_REBELC_1	15.17	85	164.7
star_REBELC_2	15.73	85	202.6
star_REBELC_3	14.01	85	172.0
star_REBELC_4	14.03	85	155.1

Table 6.13: The thermal resistance and the junction temperature obtained for each single LED , mounted on the star PCB and operating at 1.2 A and at the reported ambient temperature.

CHAPTER 7

LED reliability: analysis and experimental details

In this chapter the principal mechanisms that limit the LED technology reliability will be discussed in order to better understand the obtained experimental results, and to critically indicate future developments and suggest improvements concerning these devices. A special care will be given to the limiting mechanisms concerning the white LEDs reliability, and in particular the optical reliability will be analyzed. The lumen trend during the different hours of operation under stress conditions are presented: notice that since they have been obtained in the last part of the thesis work, and they have to be continued because of the great number of hours necessary to the stress to be effective, they are just a partial view of the reliability issue. Actually all along the analysis the results obtained from other studies are reported, in order to constructively compare them with the ones obtained here.

7.1 The failure of the XP-G LEDs

The first part of this chapter is dedicated to the principal problems encountered with the XP-G devices. During the first operation hours two sets of these devices presented two different problems, concerning the first an electrical failure of some LED mounted on the MCPCB, the second a browning of the epoxy lens over the chip.

7.1.1 The catastrophical failure of the XPGA devices

A detailed analysis should be given to the failure of a part of the XP-G devices during the stress. Three of the four mounted devices, running the 65th hour of stress, catastrophically crashed into a short circuit, that allowed the series of the whole nine boards to keep functioning, but the failed devices never turned on again. The electrical failure soon became evident, and the devices were immediately desolded from the board and analyzed by the microscope. The obtained images are reported in Figure 7.1: in 7.1 (a) is evident the epoxy lens breaking, that could render a worsening of the optical properties but is surely not responsible of the electrical short. On the other hand the bondings are not even ruined or collapsed: the breaking is probably happened inside the package, and the short circuit could involve the whole active region. An electrical characterization via I-V measurements did not give

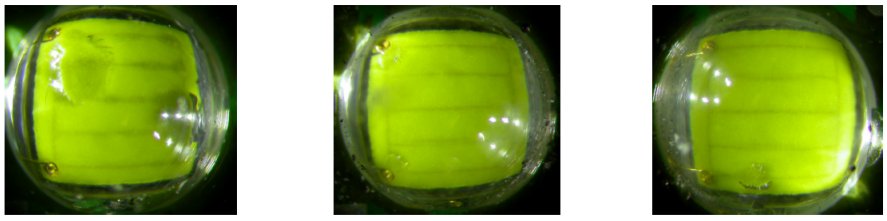

Figure 7.1: Three LEDs from the XPGA board. While the devices' behaviour is a perfect short circuit, the top side of the chips do not present any browning or apparent damage. Notice in (a) and (c) the crashed lenses

any significant response, as they behaved like perfect shorts both in inverse and in forward operation, and so further investigation are recommended to fully understand what happened to them.

The fourth LED mounted onto the same board presented an open circuit behaviour, as it did not turn on at a subsequent trial, and, once a I-V measurement was acted and reported in Figure 7.2, the electrical behaviour was find to be quite resistive. A classical electric failure would have crashed the bondings over the package, but again they are examined to be intact, indeed once again more accurate analysis is necessary.

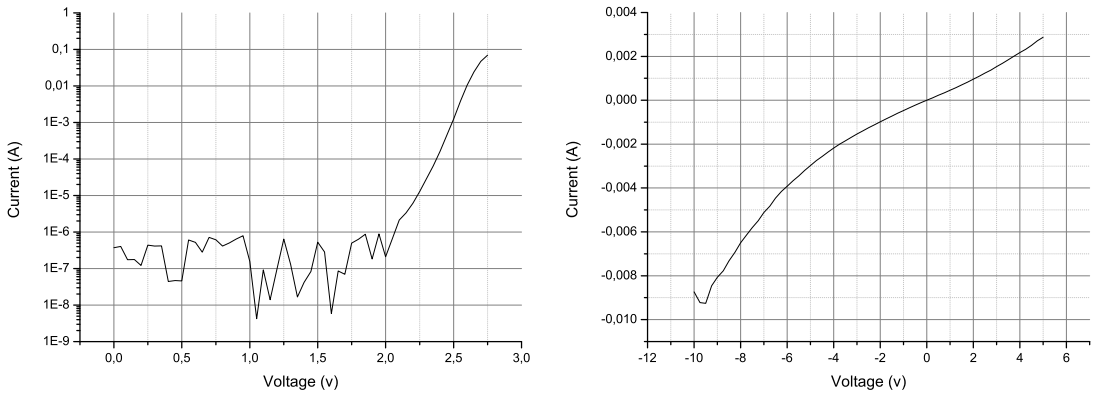

(a) LED before failure (b) LED after failure

Figure 7.2: The I-V plot of the fourth LED of the XPGA board, before (a) and after (b) the failure. In (b) a bias from -10 to $4\ v$ was imposed, and the quasi-resistive trend of the curve was noticed.

7.1.2 The chemical weakness of the XP-G epoxy lens

During the first hours of operation of the star devices a browning of the XP-G epoxy lenses has been noticed. A couple of devices presented an increasing of the browning in the external part of the dome from the 8th to the 16h hour of operation, as represented in Figure 7.3.

Since this problem has been verified in two LEDs of the XP-G type, it was initially considered to be an optical degrading of the epoxy lens, due to the high optical radiation condition these devices were operated. A successive partial browning of one of the OSLON devices made necessary a deeper investigation of the mounting process, which revealed a spreading of the soldering paste flux over the star PCB, that might have contamined in some cases the epoxy lens.

An intentional spreading of the flux over the lens of two more XP-G star devices confirmed this hypotesis: as represented in Figure 7.4 the epoxy lenses suffered of a hard chemical attack, that were evidently enphasized by the LED operation. A 4-hour functioning at the ambient temperature of 65 ^oC revealed to be destructive for the LED that were completely ruined by the lens browning.

As reported in Figure 7.4(a) - 7.4(b) even a little quantity of this chemical substance catastrophically influenced the lens conformation, which presented in both cases a radical modification of its structural, chemical and optical properties.

Since the degrading results represented in Figure 7.3 and 7.4 were due to a high temper-

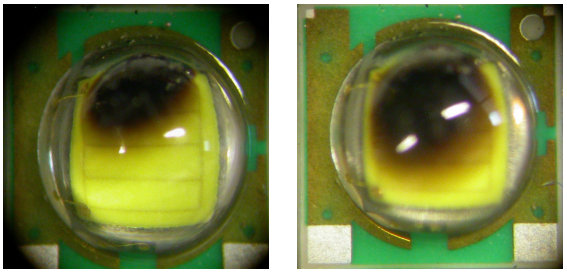

(a) LED after 8 hours (b) LED after 16 hours

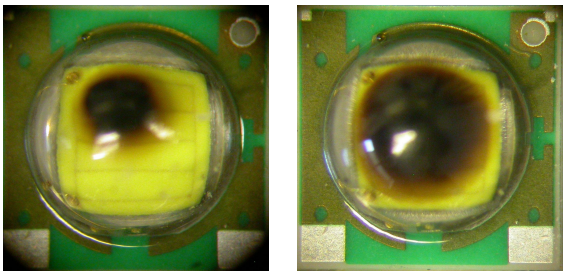

(c) LED after 8 hours (d) LED after 16 hours

Figure 7.3: Photos representing the lens browning of the (a), (b) XPGB3 device and (c), (d) XPGC4 devices. After 8 hours of operation an enlarging of the browning is observed.

ature and high current operation of the devices, the causes of the browning of the fluxant paste and its chemical matching with the epoxy dome are not clear, as they can be thermally-activated or induced by the high luminous flux out from the LED itself. A deeper investigation leads us to consider a thermal storage of the LEDs at the temperature reached during operation, i.e. 130 ^oC, with no bias applied and verifying the behaviour of some flux drops over the lens. The results are reported in Figure 7.5: the high temperature influenced introducing a browning of the flux paste itself, which passed from a semi-transparent color (a) to a deeper brown (c).

Comparing Figure 7.5(c) with 7.4(b) the phenomenon dynamic appears to be clear: the thermal storage induced only a partial browning of the fluxant, but the chemical reaction with the lens is not complete: as the results achieved after 16 hours of thermal storage are not comparable with the ones of only 4 hours of the device functioning, the light output from the LED chip is decisive to the process under investigation. The browning of the lens and its complete wasting is probably caused by an ulterior overheating of the lens surface, due to the

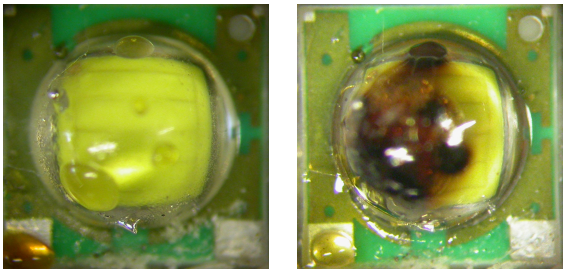

(a) LED 1 at 0-hour (b) LED 1 at 4-hour

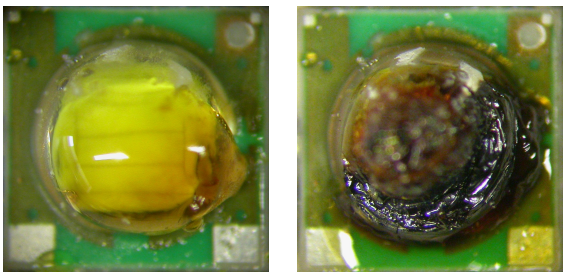

(c) LED 2 at 0-hour (d) LED 2 at 4-hour

Figure 7.4: Pictures (a), (c) represents the intentional spreading of flux paste over the XP-G dome. In (b) and (d) are reported the same LEDs after 4 hours of operation at $1.2\ A$ and $T_{amb} = 65\ ^oC$

multiple internal reflections of the light trapped inside the lens thanks to the brown coating, and these processes induce a chain reaction that leads to an increase of the extension of the brown surface, as were noticed in Figure 7.3.

This process was induced not just in the XP-G LEDs , but an investigation was also performed in the OSLON and REBEL devices, which were stained with some drops of fluxant as well. Figure 7.6 shows how the thermal storage results are much similar to the ones of the XP-Gs, as the high temperature, that in these devices were of $150\ ^oC$, leads to a partial browning of the fluxant itself, and does not influence in the interaction between the lens and the paste. As shown in Figure 7.6 (c) and (f), once the devices were turned on at the temperature of $T_{amb} = 65\ ^oC$ such that the $T_j \simeq 150\ ^oC$, the browning of the lenses were a little bit increased in the OSLON device while the operation did not influence the lens appearence in the REBEL ones.

After 4 hours of operation, the results are not comparable to the ones obtained in the XP-Gs. In particular during the operation no enlargement of the browning surface were verified: for the OSLON device the browning of the fluxant is increased but not its surface over the lens,

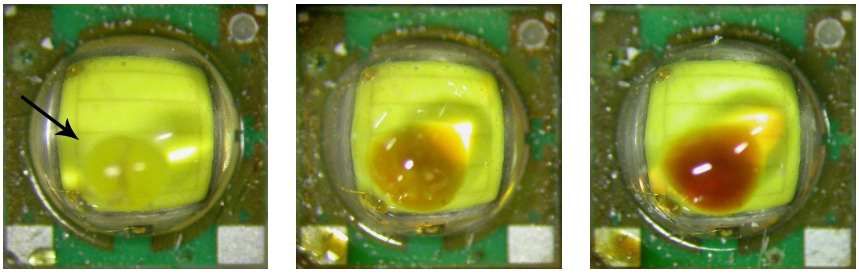

(a) LED at 0-hour (b) LED at 1-hour (c) LED at 16-hour

Figure 7.5: The evolution of the flux browning during 16 hours of thermal storage of the XP-G device, where in (a) the drop of flux paste over the virgin device is indicated, (b) and (c) report the lens state at 1 and 16 hours respectively.

while in the REBEL case the paste remained the same, and even a reduction of its browning is observed. In these two cases a subsequent removing of the residual contamination of the device completely cleaned the lens, thus no chemical reaction nor irreversible wasting of the lens has been verified, like the phenomena encountered in the XP-G investigation.

7.2 The degradation analysis of GaN-based LEDs

As reported in [24], the three degrading aspects of a LED , namely the electrical, thermal and optical ones, are not fully separable: as a matter of fact, on one hand they are all involved during the operation of the device, and they equally contribute to a complexive degradation of either the electrical, thermal and optical characteristics. On the other an experimental distinguish is not completely possible during measurements, since most of the times a single measured parameter involves one or more aspects of the device - as we saw the voltage measurement renders the junction temperature.

The final parameter of interest is the optical output power, and since it is given by a certain injected current, the processes involved in the device degradation can be distinguished as follows:

- modifications of the purely electrical properties of the LED , as the worsening of the ohmic contacts and the subsequent creation of an additive parallel or serial resistance;
- changes in the optical behaviour of the LED chip, like the generation of nonradiative centers that limit the internal quantum efficiency and lower the optical output, or

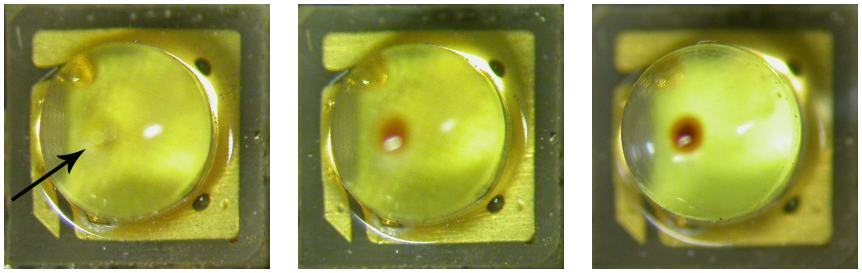

(a) OSLON at 0-hour th. storage

(b) OSLON at 16-hour th. storage

(c) OSLON at 4-hour operation

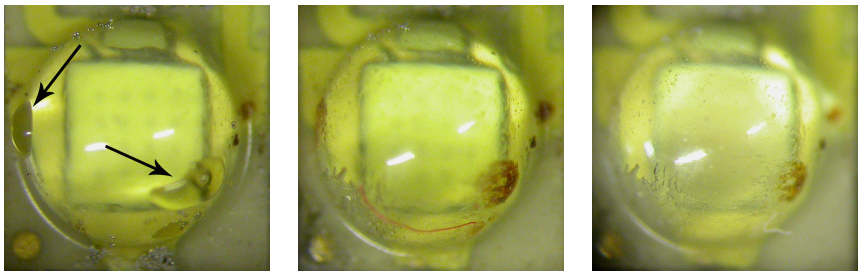

(d) REBEL at 0-hour th. storage

(e) REBEL at 16-hour th. storage

(f) REBEL at 4-hour operation

Figure 7.6: The results after various hours of thermal storage at a temperature of $T_{amb} = 150\ ^oC$ for (a), (b) the OSLON and (d), (e) the REBEL device. In (c) and (f) are reported the same devices after four hours of operation with $T_j \simeq 150\ ^oC$.

modifications of the epoxy lens that reduce the light transmission;

- hybrid modifications, such as changes in the charge injection mechanisms into the active layer: this could be caused by an increased tunnel-effect and is often noticed by a lowering of the optical power.

The listed phenomenology is certainly not exhaustive because the thermal aspect could interfere to accentuate the degrading dynamics or change the structural properties of the devices. The influence of the thermal issues, that becomes more important when a high stress temperature condition is involved, is often responsible of the worsening of the chromatic properties and in general of the degradation of the optical features of the device, such as the browning of the epoxy lens and the degradation of the yellow phosphors.

One of the most common and even simpler stress techniques involves the separation of the high temperature and the high current operation conditions, during which the devices

are stressed either by a high ambient temperature with no applied bias, or by a high applied current and different junction temperatures. Although we observed that the junction temperature can be influenced both by the ambient temperature and by the injected current, the second one is obviously the most general and has been adopted in this work.

The adopted current stress conditions, that in our case have been already explained in details, are over the maximum nominal operating values declared by the manufacturer, thus the acted stress can be considered to be an *accelerated lifetime stress*, as the standard operational conditions are not satisfied and the final results obtained in this way are expected to be reached only after a much longer operation under nominal values.

The principal degrading processes and measurement techniques are presented by many authors [23], [24], [25] and are reported below. These and other experimental results have been compared to the results that are obtained here, in order to understand the causes and effects of the mechanisms activated by the stress in the measured devices.

7.2.1 The increase of nonradiative recombination centers

Among the causes, that involve a decrease of the optical output power, there is the increment of nonradiative centers that renders a minor number of radiative recombinations and a lowering of the internal quantum efficiency. The mechanisms responsible of the nonradiative centers increment are surely accentuated during a high temperature operation, but are demonstrated to be present even during a normal low-current operation [23], so it is very important to understand the involved dynamics, in order to design the right improvements to this technology.

The effects of this degradation can be clearly observed both by I-V and L-I measurements: as a matter of fact, the generation of defects within the active region can leads to an increase of the parallel resistance of the diode and to a lowering of the optical power for low current densities as well. The electrical properties of the active region can be investigated by inverse I-V measurements and by C-V measurements: the former are reported and better explained in the discussion of the results, the latter were not performed in this study [1].

Observing the L-I relation it is possible to point out the creation of the nonradiative

[1]The C-V measurements are conducted during light emitting diodes, power diodes and transistors investigations, as they allow a more detailed knowledge of the dopant distribution inside the junctions. They can reveal the presence of defects inside the semiconductor lattice and modification of the alloy during stress.

centers, since the nonradiative processes commonly prevail for low currents injections over the radiative ones, and the total light output is affected by their increment. Nonetheless the nonradiative recombination paths can saturate for high current injection, and their effect on the overall light output is limited.
To better understand this important distinction, we refer to the continuity equation for the injected electron density n:

$$\frac{dn}{dt} = \frac{J}{qd} - An - Bn^2. \tag{7.1}$$

At steady state conditions, we have $dn/dt = 0$ and two cases are distinguished:

- for a low current injection the nonradiative processes dominates, and the relation is written introducing the light output L:

$$L = Bn^2 \simeq \left(\frac{B}{A^2}\right)\left(\frac{J}{qd}\right)^2, \tag{7.2}$$

  that is evidently proportional to the square of the current injection quantity;

- at high current densities the radiative recombination dominates over the nonradiative, thus the following holds:

$$L = Bn^2 \simeq \frac{J}{qd}, \tag{7.3}$$

  where the light output is directly proportional to the injected current.

The two regions are pretty distinguishable in the L-I plots, so a dilatation of the first region over the second is an evident signal of the increase of nonradiative decays and so the generation of defective centers during the ageing, as it will be pointed out during the results discussion.

The creation of nonradiative centers has been noticed to be current-activated, thus a great current flow towards the active layer can induce the diffusion of defects in there and the generation of nitrogen vacancies in the whole active region. These imperfections represent a discontinuity in the regular semiconductor lattice and they promote the nonradiative decays.

7.2.2 The ohmic contacts worsening

The increase of the serial resistance, or in general a significant change of the electrical properties can be related to a degradation of the electrical bondings of the LED chip: this is noticed both by an increase of the operating voltage and by a complexive lowering of the optical power. The electrical characteristics significantly change during a high temperature

or high current operation, and these can influence the chip structure in several ways, like increasing the resistivity of the metal-semiconductor contacts and of the p-type neutral regions, or worsening the current distribution over the active region due to current crowding effects.

The high-temperature operation of the chip can increase the chemical interaction between Mg-acceptor atoms and Hydrogen which involves a lowering of the effective carrier concentration, the increase of resistivity of the metal-semiconductor interface and of the p-type neutral region, together with a broadening of the Schottky barrier at the p-type ohmic contact. All these effects can lead to a general worsening of the current distribution over the active region, with the subsequent lowering of the current injection inside the active layer and the lowering of the optical power. Since the release of Hydrogen is due to imperfections inside the lattice and is impoved by a high-temperature operation of the device, an improvement of the heterointerfaces is necessary to reduce the presence of hydrogen defects inside the semiconductor structure.

As well as the high temperature operation, high currents lead to a morphological degradation of the ohmic contacts: some works [23] reveal the detachment of the bondings as a consequence of high current conditions, that is probably due to a poor adhesion and/or to a thermal mismatch between different metal layers inside the chip.

7.2.3 The degradation of the chromatic properties

The luminous flux lowering is partially explained by the increase of nonradiative decays, while a more detailed analysis about the quality of the light can be conducted in order to quantify, for example, chromatic shifts or in general significant changes in the optical behaviour of the devices.

The white LEDs are structured by a blue pumping LED chip below a yellow phosphors mix, in order to render a wider spectrum radiation. This double conformation obviously leads to a double degradation, as the blue LED can suffer of a lowering of its output power due to a worsening of the chip structure, and a yellow radiation decrease can be ascribed to a browning of the material used for the encapsulation of the phosphors/chip system, or to the pure worsening of the phosphors: both these elements contribute to a changing of the chromatic coordinates. Under exceptional degrading conditions this changing can lead to a radical variation of the perceived radiation color.

A worsening of the package itself is often caused by high temperatures operation, and consists in a partial carbonization of the reflective surface of the chip, which introduces a decrease of the light extraction efficiency and a complexive lowering of the efficiency of the device.

An overall worsening of the light output can be added by a degrading or browning of the epoxy lens over the chip, which in some cases is observed to be crashed, as reported in Figure 7.1 (a).

The parameters monitored in this work concerning the optical quality of the light are the x and y chromaticity coordinates, the CRI index and the CCT: the comments about the changing of these indexes are postponed to the presentation of the results.

The mechanisms listed above are not exhaustive, and the degradation induced by a reverse current operation or by electrostatic discharge events (ESD) were not considered. These phenomena, that can be fully part of the degradation of the LED and can be a consequence of some catastrophical event over the lamp device, were not observed during the device operation, as well they were not measured. In particular the inverse operation of the LEDs were not settled, because the aim of this work was to verify their behaviour under standard stress conditions, while the ESD events was neither caused by a bad threatment of the devices nor induced on purpose by external instruments [2].

7.2.4 The time to failure evaluation

A more quantitative evaluation of the performance of the LED devices can be apted through the calculus of their lifetime, that is obviously bonded with the degradation dinamics explained above.

The principal manufacturers attach to the description of their products not only the nominal optical characteristics, that as we will see are submitted to change even significally during the device life, but also the previewed lifetime. The LEDs are not supposed to catastrophically fail at the end of their lifetime, as happens for the incandescent lamps, thus the lifetime is often appointed as the useful time of operating of the lamp in which a certain

[2] Altought analyzed devices were supposed to have a high robustness against ESD, their management were apted only with the antistatic bracelet: apart from th XPGA board, no catastrophical event was verified.

characteristic stays below a predetermined limit. For instance this useful parameter, called *Time To Failure* (TTF) can be calculated observing the trend of decay of the light output expressed in lumen, and searching for the moment in which the decay is the 30 % below the initial measure. The operating time that the lamp did accumulate is called $TTF_{70\,\%}$.

In this work the TTF parameter has not been calculated, because the devices actually did not reach a significative decay. As we will see in the next section, only the OSLONs appeared to decrease their lumen output during the stress, but even in this case the decay did not lead to a substantial end of their lifetime. Future challenges would imply the achievement of a much higher number of operation hours under stress conditions, thus once the decay is achieved this parameter would be calculated as explained above, and even a more accurate analysis of the decay dynamics would be apted.

7.3 The degradation mechanisms: experimental details

Considering the three LED types that are here investigated and the two principal stress conditions at which they were submitted, the analysis of the experimental results is here conducted and their dynamics are studied, in order to realize an association with the mentioned degrading processes. Since for each kind of LED at each stress temperature four devices were involved in the same degrading process, in the L-I and I-V plots only the first LED is here considered.

The results concerning the first hour of operation are reported, as well as the optical characterization conduced during the last part of the work, when a greater number of hours of stress has been achieved and the degrading of the device appeared to be more evident. The changing of the lumen output and the electrical characteristics during the stress is evaluated and critically compared for the three kinds of LEDs , while the variation of the chromatic properties is as well analyzed. Note that, since for each LED type the measurements concerning the three stress temperatures are available, the three plots are reported only if significant differences are notable: in order to simplify this tractation, if no difference were noticed among the three stress temperatures only the results concerning one of them (i.e. $T_{amb} = 65\ ^oC$) are reported.

The absolute values of the L-I curves are here not reported, but a better analysis is conducted normalizing the trends to the measurement conducted on the virgin devices. As

a matter of fact the changing of the lumen output for low current operation is much better noticeable in this way, and the variations of the Optical Power (OP) for high currents is as well emphasized.

The I-V measurements take on account not only the variation of the electric properties of the devices, but also the changes that appear in their semiconductor structure: in particular in some cases a lowering of the threshold voltage has been identified, and also the current value at a certain voltage is observed to increase during the operation of the device. Both these elements can be due to the increase of nonradiative centers, that may represent a lower-resistance path for the current through the active region, a changing in the doping profile or some modification in the current-spreading process. The electrical scheme shoud be changed in order to introduct a serial or parallel resistance (R_S, R_P in Figure 7.7) together with the ideal diode functioning.

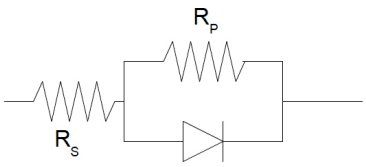

Figure 7.7: The electrical scheme of a LED device, in which the serial (R_S) and parallel (R_P) resistances are highlighted.

7.3.1 The LEDs stressed at 700 mA

The LEDs mounted in the first set of MCPCBs were stressed at the ambient temperature of $T_{amb} = 45$, 65 and 85 ^oC and at a forward current of 0.7 A. The optical measurements were performed at exponential hours steps, and complessively show that the conduced stress did not influence the optical power output of the XP-G and REBEL devices, while the OSLONs suffer of a drastic decay depending both from the temperature and from the operating time. The following analysis reports the optical and electrical features for each kind of LED , in order to underline the strict correlation between the changes in the optical output and the electrical behaviour during the stress. The OP trend of each kind of LED at the different ambient temperatures is as well presented: the reported curves are found by the average of the decays of the four LEDs on the same PCB, and the standard deviation is as well reported through the error bars. Notice that since the presence of nonradiative centers is more relevant

in the low current operation, and the corrispective OP for these currents would be affected by a more accentuated decay, the results concerning a current of 100 mA are reported, as well as the ones measured for the nominal current of 700 mA. In the fourth section is then reported the results concerning the qualitative optical behaviour of the devices, i.e. the x and y coordinate variation during the ageing.

The results concerning the XP-G LEDs

In Figure 7.8 is reported the variation of the lumen output from the measurement conducted on the virgin XP-G device to the one done after 1000 operating hours at the ambient temperature of 45 ^oC.

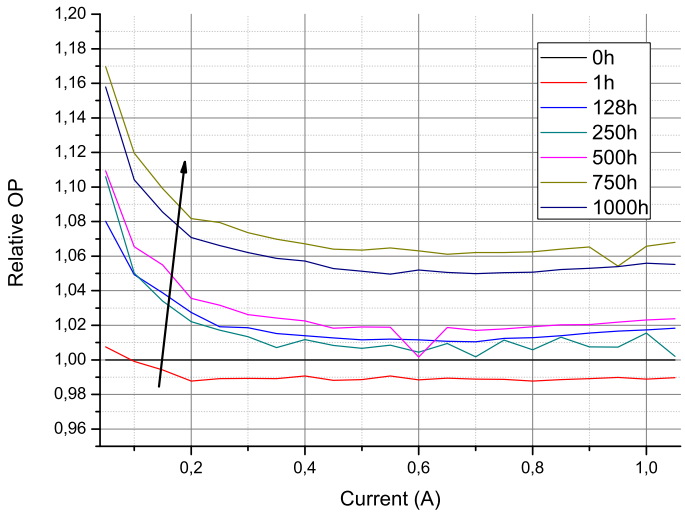

Figure 7.8: The measurements of the Optical Power vs. current conducted on the first XP-G device at various stress steps and normalized to the initial value. The results are relative to an ambient temperature of $T_{amb} = 45\ ^oC$, while the results concerning the board at $65\ ^oC$ are much similar.

The XP-G LEDs are observed to suffer of a slight decay during the first hour, while the subsequent measurements report an increase of the OP in respect to the initial value. Moreover in the low-current region, in which it is said the nonradiative processes prevail, the curve trend is nearly exponential, which means that the nonradiative centers apparently decreased their density, thus the optical efficiency is increased as the OP rises. On the other hand a high current injection leads to a curve with a complexive increase of the OP, that could be a reflection of the lowering of the nonradiative centers, or even a activation of dopers inside the lattice that leads to a more efficient current injection and a greater number of radiative

decays.

The behaviour of the OP for a low and high current injection is reported in Figure 7.9(a) and 7.9(b) respectively. The trends are normalized to the optical measurement conducted before the stress and the results concerning the 45 and 65 ^oC ambient temperature are reported. Notice that the catastrophical failure of the XPGA basis causes the lack of the stress curve at 85 ^oC, while analogous events occurred in two LEDs of the PCB at 45 ^oC and in one at 65 ^oC, thus the relative trends have to be considered less reliable than the others here presented. Since the values are derived by the average of the mounted devices, the error bars report the standard deviation.

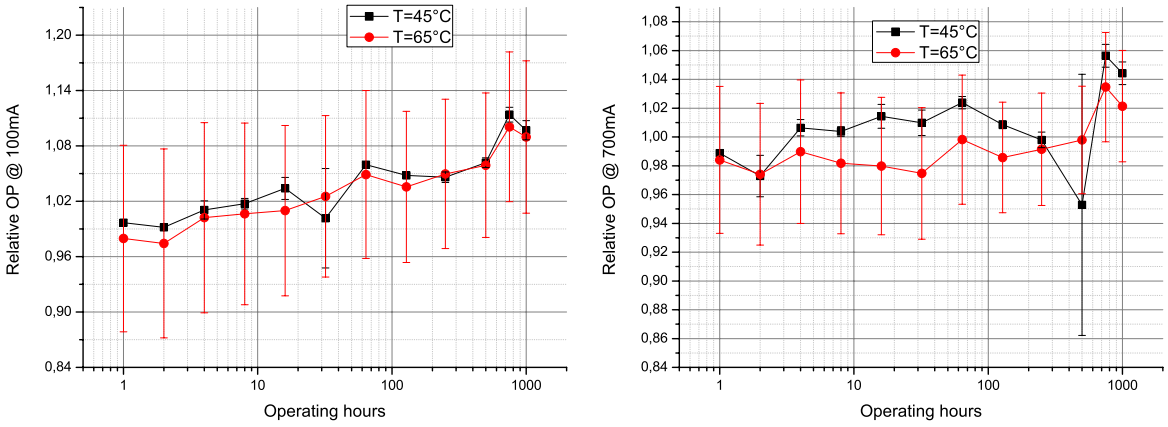

(a) (b)

Figure 7.9: The OP trend for the first 1000 hours of operation of the XP-G devices, measured for a forward current of 100 mA and 700 mA. The values are normalized to the zero-hours measurement, and the results of the boards stressed at $T_{amb} = 45\ ^oC$ and 65 ^oC are reported.

The low values and the high standard deviation confirm that no substantial degradation has been achieved, moreover in both the plots the devices are seen to increase their OP. In particular this is evident under low current operation: as noticed in the L-I curves, for low currents the devices are improving their output in the last measurements, and this is clearly shown comparing the OP level reached in the two plots.

In the I-V characteristic, reported in Figure 7.10, no variation of the threshold voltage has been noticed and the currents do not suffer of a great changing during the stress. This is in accordance with the absence of a substantial creation of nonradiative centers that can influence the electrical characteristics of the device. Moreover an assestment of the electrical condition can be verified from the inset plot, in which some little variation of the current

flow can be noticed: this is due to the normal device assestments during the first hour, and reveals to be neglegible in the successive measurements.

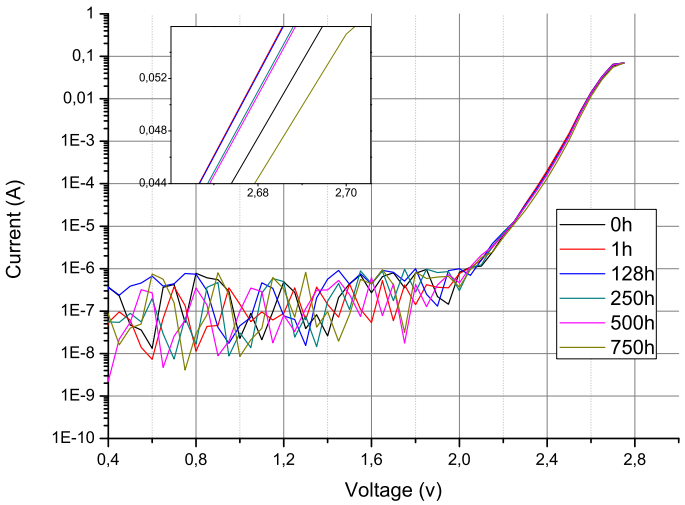

Figure 7.10: The I-V characteristics for the XP-G device stressed at $T_{amb} = 45\ ^oC$. The values are plotted in logarithmic scale and in the inset plot the disposition of the currents after each stress step is reported.

The results concerning the OSLON LEDs

The OSLON devices evidently present a progressive increase of the nonradiative centers during operation: Figure 7.11 clearly points out how in the initial hours the light output is nearly constant, while a drastic lowering is observed in the subsequent measurements: after just 128 hours of operation (blue curve) the increase of defects inside the semiconductor lattice is evident for low currents. In the high currents region the nonradiative centers still influence the optical output, that is lowered even after 1000 hours of operation.

The presence of the nonradiative centers is put in evidence by the plots in 7.12, which show the OP decay of the OSLON devices at the three ambient temperatures. As a matter of fact, the creation of nonradiative centers that appeared evident in the previous analysis is here confirmed by the lower OP value reached by the plots in the leftmost figure, in respect of the values obtained for a higher current operation. In the same plot a slight dependence of the decay with the temperature can be noticed, especially in the last measurements.

The I-V characteristics show to suffer of a relevant changing during the device operation: Figure 7.13 clearly points out the creation of a preferential path for the current flow, which

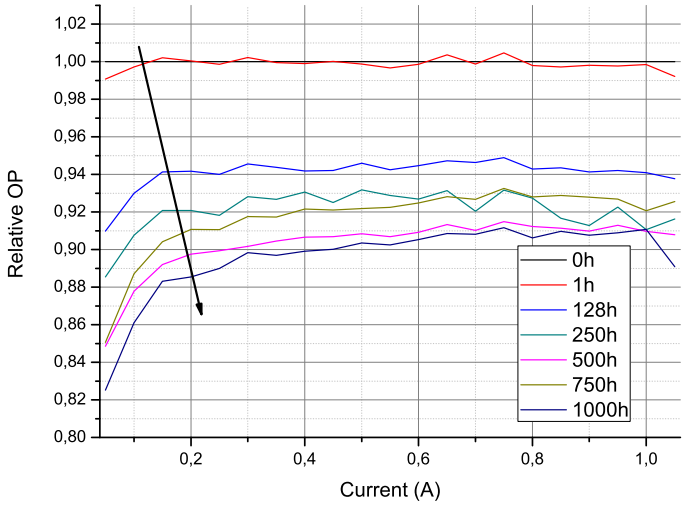

Figure 7.11: The L-I relation for the OSLON devices stressed at $T_{amb} = 65\ ^oC$. The curves are normalized to the first measurement.

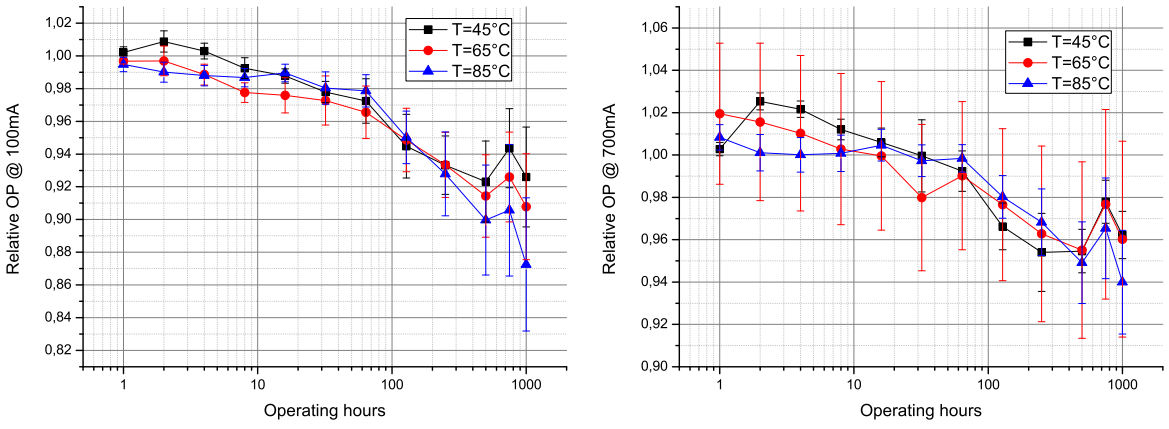

(a) (b)

Figure 7.12: The OP trend for the first 1000 hours of operation of the OSLON devices, measured for a forward current of $100\ mA$ and $700\ mA$. The values are normalized to the zero-hours measurement.

is highlighted by the non-neglegible current absorption below the threshold voltage and the increase of the current for higher voltages. This is due to a parallel resistance that is represented by the nonradiative centers and other impurities trapped inside the lattice, whose presence has already been noticed within the L-I curves.

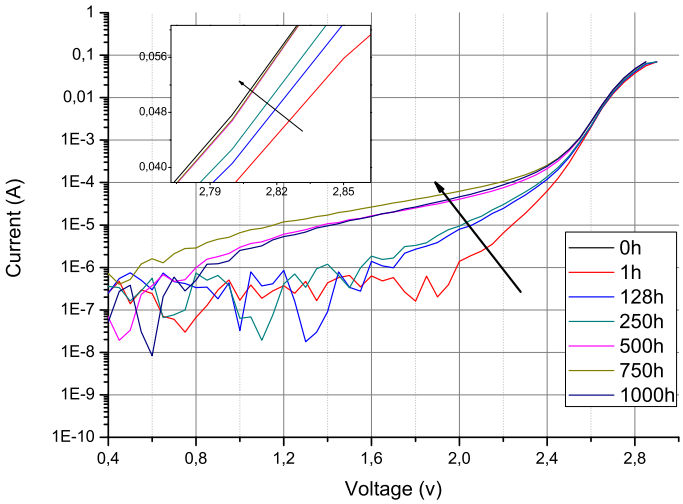

Figure 7.13: The I-V characteristics for the OSLON device stressed at an ambient temperature of $T_{amb} = 65\ ^oC$. The values are plotted in logarithmic scale and in the inset plot the disposition of the currents after each stress step is reported.

Because of the presence of the parallel resistance in the electrical behaviour of the OSLON devices, the presence of a serial one has not been noticed: as a matter of fact, the parallel electrical path yields to an increase of the current that could hide the effect of the eventual worsening of the ohmic contacts, or in general of the electric changes of the chip. Moreover a deeper investigation through C-V measurements should reveal how the stress influenced the charge disposition inside the active region: in some cases [23] the shift of the I-V curve towards lower voltages has been found to be due to substantial changes in the carrier concentration inside the active region, that is reflected by an increase of the junction capacitance. The investigations conducted in this matter revealed that the shift of the I-V curve is almost due to the increase of the defects concentration inside the lattice, or in general to a diffusion of impurities in the SCR.

The results concerning the REBEL LEDs

As happens for the XP-Gs, these devices do not suffer of a relevant decay of the OP after 750 hours of operation and no dependace with the ambient temperature has been verified. As shown in Figure 7.14, no increase of nonradiative centers is noticeable, but just a monotonic increase of the OP affects the operation under all the current injections conditions. Nevertheless a slight decay of the OP for low currents is noticed after the first hour of operation, as well as a faint increase for higher injections. After this assestment the increase of the OP is equally verified for all the currents conditions, thus the subsequent curves still present a slope that can be eliminated after a normalization in respect to the first hour of operation.

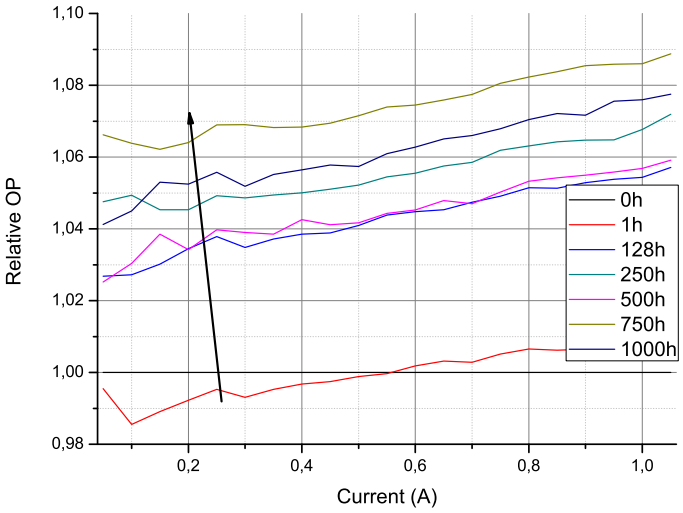

Figure 7.14: The Optical Power vs. current data relative to the REBEL device, normalized to the initial measurement. The results are relative to an ambient temperature of $T_{amb} = 65\ ^oC$, while the other two analyzed temperatures are analogous.

The plots in 7.15 confirm that these devices are observed to maintain an increase of the OP even after a great number of operating hours and under the higher stress temperature: moreover the two set of plots are identical, so the relative light output has demonstrated to not depend from the injection current, and this is again a confirmation that no generation of nonradiative centers is happened.

The last measurements show a slight OP decrease that is verified especially for the devices at the higher ambient temperature. This could be due to the worsening of the ohmic contacts, that can be noticed within the electric behaviour description.

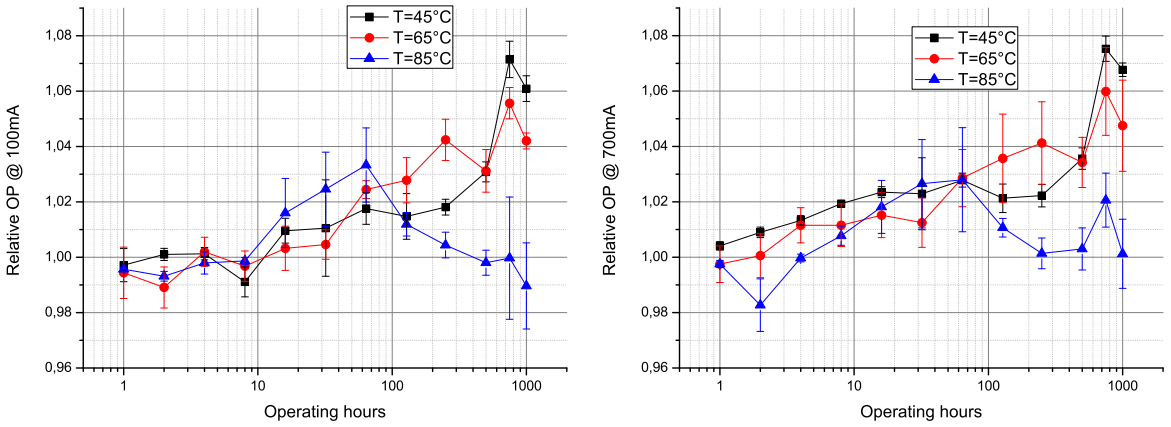

(a) (b)

Figure 7.15: The OP trend for the first 750 hours of operation of the REBEL devices, measured for a forward current of 100 mA and 700 mA. The values are normalized to the zero-hours measurement.

As concerns the I-V measurements, two important phenomena have been verified: firstly, the threshold voltage has demonstrated to shift towards lower values as the operation time increases, while for higher voltages the current absorption is lowered. The former is due to a gradual creation of a parallel resistance, while the latter can be ascribed to the presence of a serial resistance. The parallel resistance is certainly caused by changes into the semiconductor lattice, while a worsening of the ohmic contacts can lead to the increase of the serial one. From the plots in Figure 7.16 the dependence of these processes with the temperature can be noticed, and in particular a high temperature operation influences the creation of the serial resistance, as represented in the inset plots. The presence of the serial resistance is also confirmed by the decay of the OP that is verified for the devices operating at the higher temperature.

The chromatic properties variation: x, y coordinates

The analysis of the changing of the chromatic features of the devices can be conducted from different points of view, depending by which photometric unit is considered: for example the variation of the CCT can be analyzed, or the CRI can be as well considered. In this tractation the more general properties are considered, i.e. the x and y chromaticity coordinates. From these quantities the CCT and the perceived color of the light source is evaluated, and their shift upon the chromaticity space takes on account the variation of the

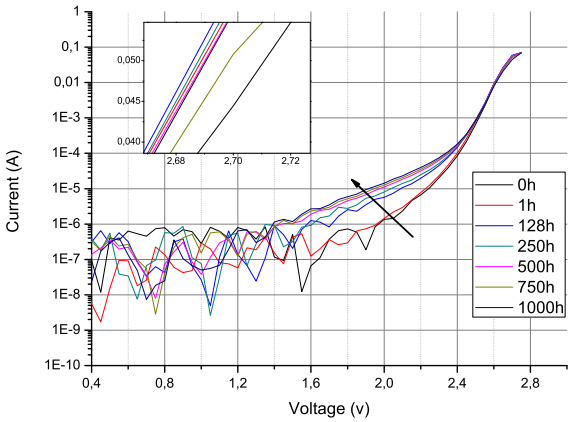

(a) $T_{amb} = 45\ ^oC$

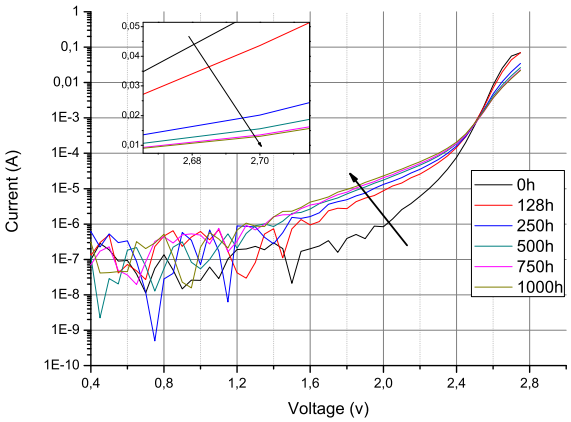

(b) $T_{amb} = 65\ ^oC$

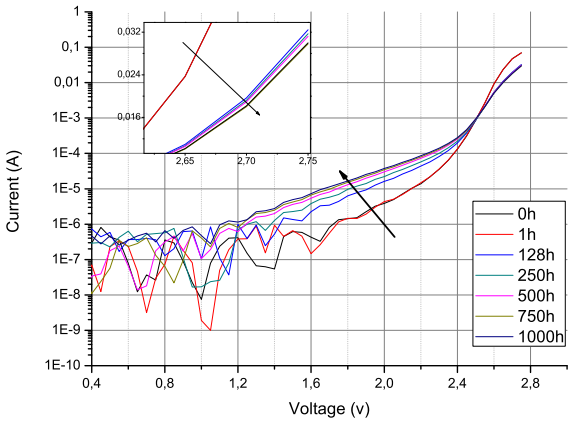

(c) $T_{amb} = 85\ ^oC$

Figure 7.16: The I-V relation of the REBEL devices. Each plot refers to the measurement of the first device stressed at a different temperature, and the in-set plots show the progressive lowering of the current, both with the ageing time and with the temperature.

chromatic properties at which the devices are submitted.

In this case the analysis is conducted averaging the trend of the coordinates vs. ageing time for the four LEDs stressed at the same conditions: this is done both because they demonstrated to have a very low standard deviation, and because in this way it is possible to present the results concerning the three different ambient temperatures at which the devices were stressed.

The plots reported in Figure 7.17 show that:

- the chromaticity of the XP-G LEDs is not changing at all: the variations of the coordinates are below the 0.5 % of the initial value and no dependence from the temperature is noticed;
- the OSLON devices show a slight increase of both the coordinates, i.e. a shift towards a warmer color and a decrease of the CCT. The entity of this phenomenon is below the 2 %, which means that the variations are very low. Moreover a dependence with the temperature is noticeable, indeed higher ambient temperatures lead to an increase of the variation;
- in the REBEL case the variation is more evident, and even the dependence with the temperature is stressed.

The increase of the chromatic coordinates can be ascribed to a variation of the phosphors behaviour, under stress: in particular Figures 7.17(c) and 7.17(b) show that under higher temperature conditions the phosphors radiation is increased and the resulting color is warmer. Since this behaviour has been noticed also in the second stress condition, the analysis is postponed to the last section of this chapter.

7.3.2 The LEDs stressed at 1.2 A

The results concerning the second ageing process are much similar to the ones yet presented. These devices were stressed at the forward current of 1.2 A and using the same three ambient temperatures of the previous case. In particular no significant variation of the behaviour of each device has been verified in respect to the first stressing process, nevertheless in most cases the same degradation has been achieved after a number of operating hours lower than the previous. As a matter of fact the devices mounted onto the star PCBs presented a

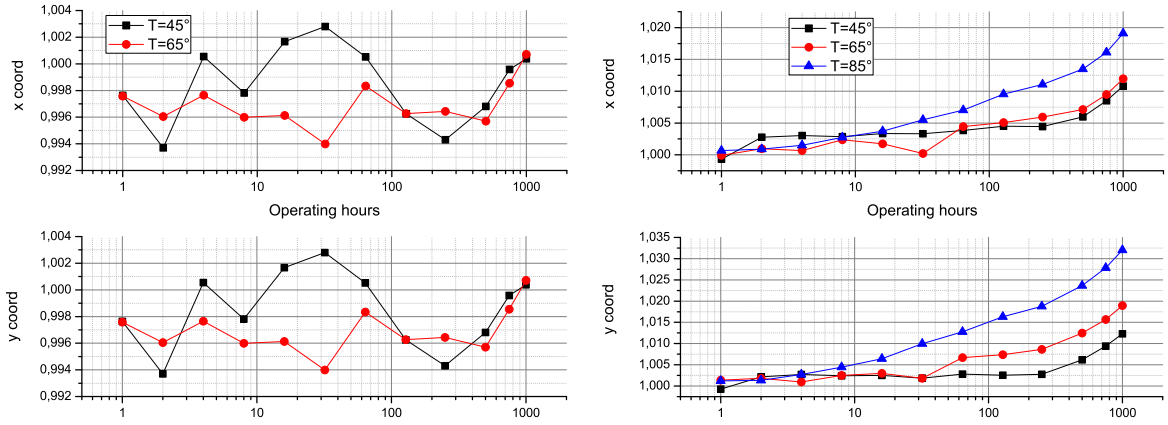

(a) XP-G LEDs

(b) OSLON LEDs

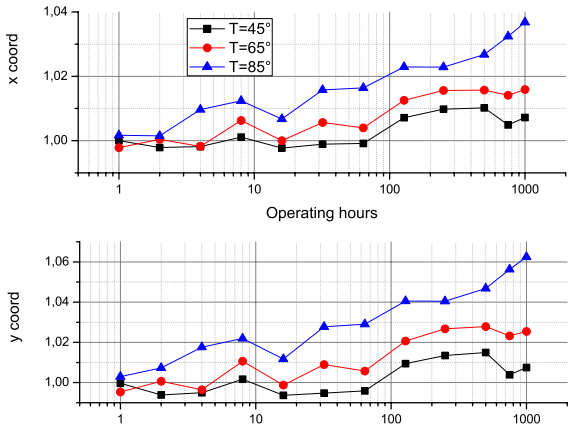

(c) REBEL LEDs

Figure 7.17: The x and y coordinate measurements for the three boards. They are the average of the four LEDs values at $700\ mA$, and the three boards, each stressed at a certain temperature, are reported.

lower thermal resistance that allowed a higher current injection, i.e. 1.2 A, with the junction temperature maintained nearly at the same level of the previous case.

The complexive OP decay of the devices is as well presented: the plots are obtained averaging the four trends of LEDs mounted onto the same PCB, and are relative to the lumen decay measured at a current of 100 mA and 700 mA, normalized to the first measurement.

The results concerning the XP-G LEDs

The XP-Gs present an increase of the OP for low current operation, that is luckily due to the activation of dopant elements inside the lattice, and the subsequent increase of optical radiation that is traduced as a lowering of the nonradiative centers. This phenomenon is noticed in all the three temperatures examined, thus only the plot about the $T_{amb} = 65\ ^oC$ is reported in Figure 7.18.

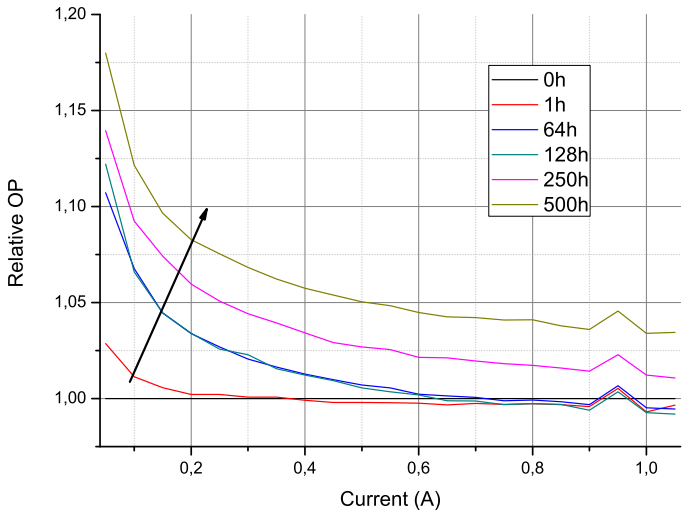

Figure 7.18: The Optical Power vs. current data relative to the XP-G LED , normalized to the initial measurement. The results are relative to an ambient temperature of $T_{amb} = 65\ ^oC$, while the results provided by the other two analyzed temperatures are analogous.

As Figure 7.19 points out, the OP is as well increased under high current injection conditions, even after 500 hours, and no dependance from the temperature is noticed. The increasing is in this case much evident in the leftmost plots, where the optical output for a low current injection is reported and a substantial increase of these values is obtained in the last measurements.

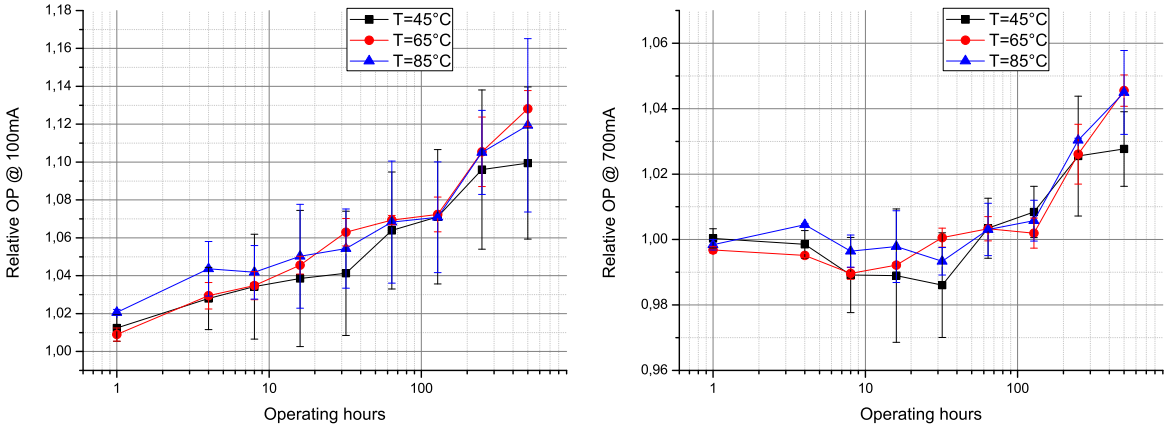

(a) (b)

Figure 7.19: The optical decay of the XP-G LEDs measured at the forward currents of $100\ mA$ and $700\ mA$, relative to the measurement conducted on the virgin devices. For each graph the results concerning the three temperatures are reported.

The I-V characteristics are in accordance with these result, because no sensible variation is noticed. In particular the threshold voltage is not varied during the stress, and even when the LED is turned on, no lowering or increasing of the current can be verified. In Figure 7.20 is reported the I-V measurement conducted on the device at $T_{amb} = 65\ ^oC$.

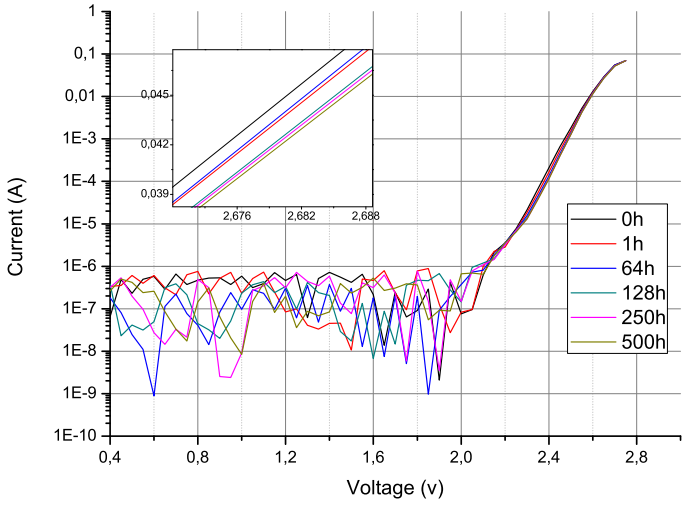

Figure 7.20: The I-V characteristics of the XP-G device stressed at an ambient temperature of $T_{amb} = 65\ ^oC$. The values are plotted in logarithmic scale and in the inset plot the disposition of the currents under high voltage operation is reported.

The results concerning the OSLONs

These devices have demonstrated to suffer of a strong OP decay depending from the hours of operation at which they were submitted: the graphs in 7.21 report the normalized L-I relations for one of the devices stressed at the temperature of $T_{amb} = 65\ ^oC$, and they clearly show how the number of nonradiative decays is increased after 500 hours.

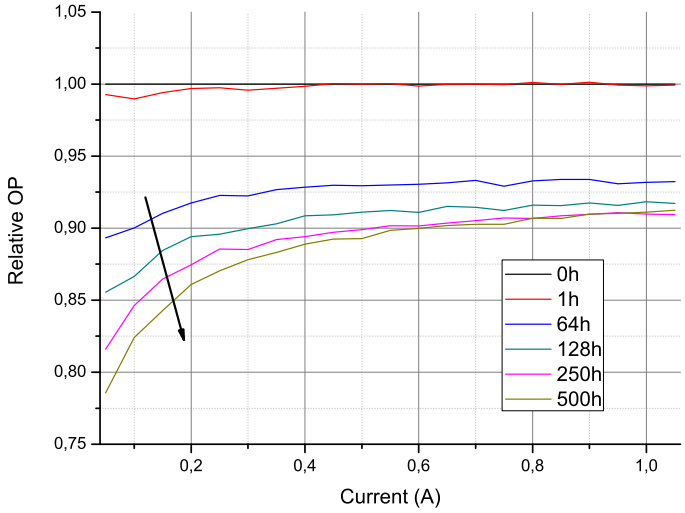

Figure 7.21: The L-I trends relative to the OSLON LED , normalized to the initial measurement. The results are relative to an ambient temperature of $T_{amb} = 65\ ^oC$, while the results provided by the other two analyzed temperatures are analogous.

Even in this case the OP decay for a low and high current injection is reported in Figure 7.22: the results are here much similar to the ones obtained in the previous process, because the decay is more evident in the low current operation. Nevertheless in this case the high temperature does not inflence the OP decrease, on the contrary the devices operating at the higher ambient temperature are the more performant ones.

The I-V measurements have demonstrated the influence of the nonradiative centers in the electrical behaviour of these devices. Figure 7.23 points out the lowering of the threshold voltage, that is evident after 500 hours of operation: this is due to the creation of a parallel resistance that allows an additive current flow also for high voltages, as shown in the inset plot. This feature has demonstrated to be equally present in all the three temperature conditions, thus only the one measured at $T_{amb} = 65\ ^oC$ is reported.

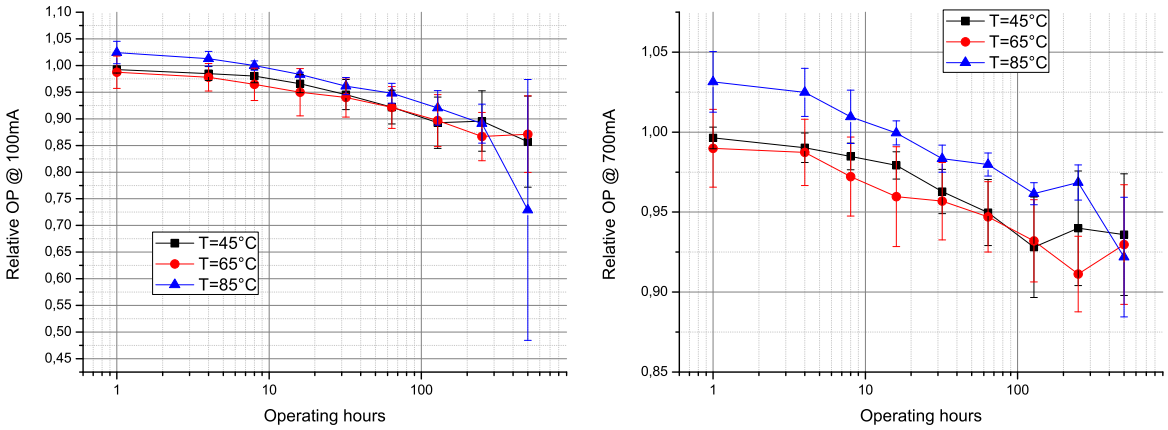

(a) (b)

Figure 7.22: The optical decay of the OSLON LEDs measured at the forward currents of $100\ mA$ and $700\ mA$, relative to the measurement conducted on the virgin devices. For each graph the results concerning the three temperatures are reported.

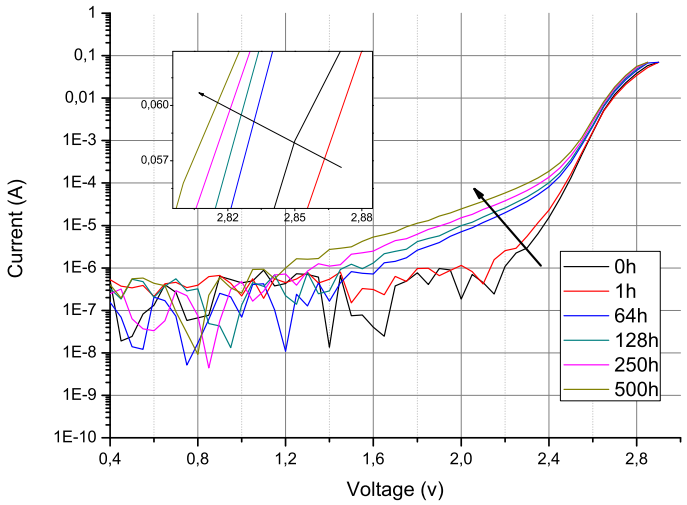

Figure 7.23: The I-V characteristics for the OSLON device stressed at an ambient temperature of $T_{amb} = 65\ ^oC$. The values are plotted in logarithmic scale and in the inset plot the disposition of the currents after each stress step is reported.

The results concerning the REBEL devices

The REBEL LEDs increased their optical performance during the stress. In particular the apparent absence of the creation of nonradiative centers is to notice: in Figure 7.24 is reported the L-I characteristic for one LED stressed at $T_{Amb} = 65\ ^oC$, and the ones submitted to the other two temperatures maintain the same trend. Thus the OP increase does not depend from the temperature (see Figure 7.26), nor from the variation of the electric features. As a matter of fact the I-V relation presented two important variations: after 128 hours the threshold voltage is lowered and the current injection at higher voltages is decreased; this process is dependant from the temperature, and the in-set plots of Figure 7.25 clearly show that as the temperature rises the presence of the serial resistance is accentuated.

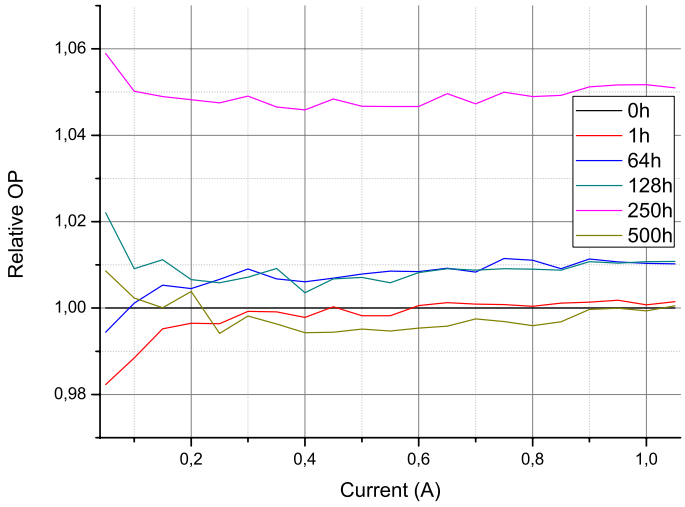

Figure 7.24: The Optical Power vs. current data relative to the REBEL device, normalized to the initial measurement. The results are relative to an ambient temperature of $T_{amb} = 65\ ^oC$, and the ones from the other two temperatures are analogous.

The plots in Figure 7.26 present the same features of the ones in 7.15: also in this case they are increasing their performance and moreover no difference can be noticed between the low and high current injection.

The chromatic variations

Even in this case, the variation of the x and y coordinates has demonstrated to be very different in the three analyzed devices. In particular the variation of the color of the XP-Gs

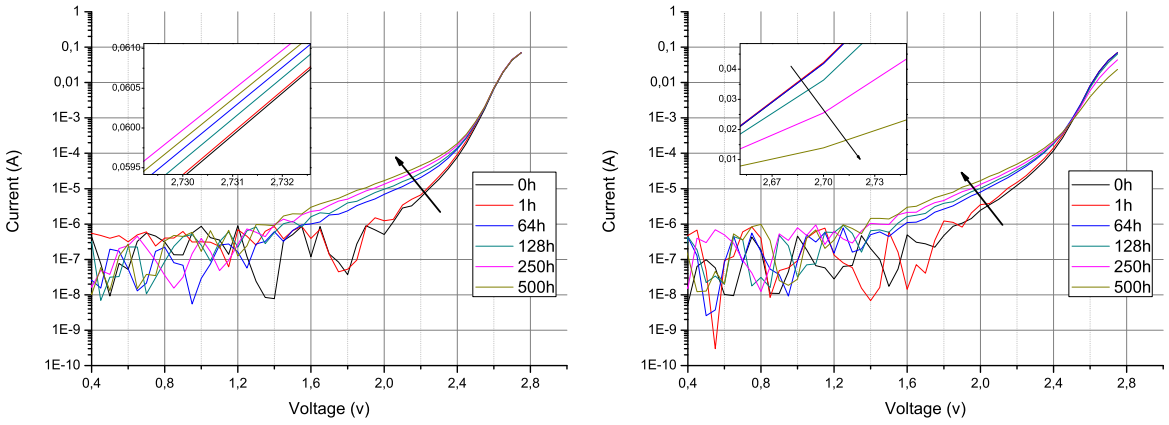

(a) $T_{amb} = 45\ ^oC$

(b) $T_{amb} = 65\ ^oC$

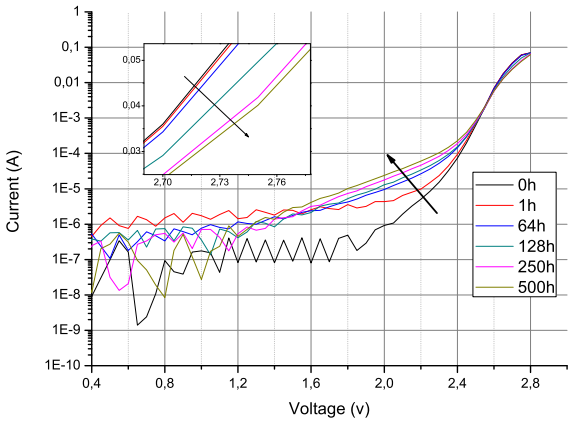

(c) $T_{amb} = 85\ ^oC$

Figure 7.25: The I-V relation for the REBEL devices. Each plot refers to the measurement of the first device stressed at a different temperature, and the in-set plots show the progressive lowering of the current, both with the ageing time and with the temperature.

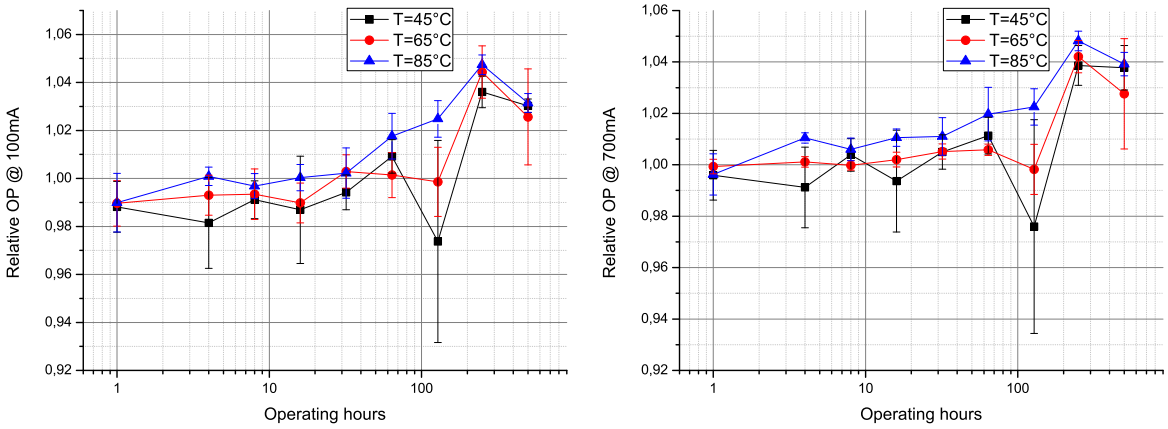

(a) (b)

Figure 7.26: The optical decay of the REBEL LEDs measured at the forward currents of 100 mA and 700 mA, relative to the measurement conducted on the virgin devices. For each graph the results concerning the three temperatures are reported.

is pretty neglegible (Figure 7.27(a)), while the coordinates of the REBEL LEDs (7.27(c)) are slightly increasing but this does not depend from the temperature. The OSLONs indeed suffer of a rising of both the coordinates that is also depending from the temperature, as shown in Figure 7.27(b). The increasing of the coordinate values are reconducible to a changing of the phosphors behaviour, that are actually increasing their performance: even if an increasing of the x and y coordinates means a lowering of the CCT, the slight shift towards a warmer color is due to a more relevant influence of the phosphors radiation. By the way the values variation is very low and can not be noticed by a human observer.

7.3.3 Comments to the results

These results confirm the fact that the optical output given by the XP-Gs and the REBEL devices does not suffer the stress conditions at which they are submitted, in particular the XP-G devices are not degrading at all, while the REBELs are increasing their output in respect to the first measurements. On the other hand the OSLON devices suffer from a gradual degradation especially under the low current operation, and this is again in according with the L-I trends that have been so far analyzed.

A comparative analysis of the two stress conditions can be apted for each kind of LED , because the two different current injections at which the devices were operated emphasized

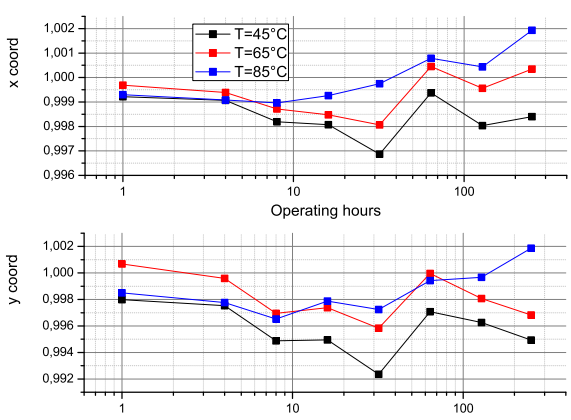

(a) XP-G LEDs

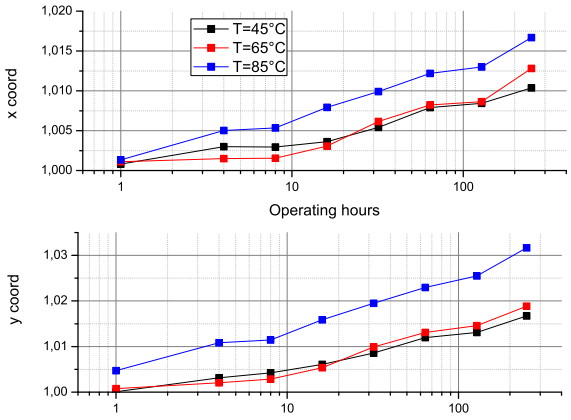

(b) OSLON LEDs

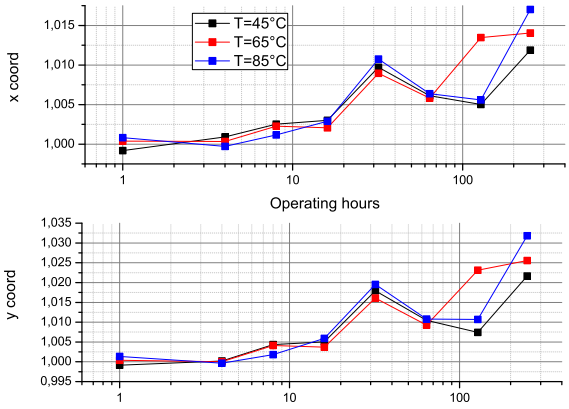

(c) REBEL LEDs

Figure 7.27: The x and y coordinate measurements for the three boards. They are the average of the four LEDs trends at the classical operation current of $700\ mA$. The three boards, each stressed at a certain temperature, are reported.

the current-dependant processes.

- The XP-G LEDs are seen to maintain a perfect electrical behaviour even after a long-term operation and in both the two conditions, since no substantial variation has been noticed both in the threshold voltage and in the higher voltage operation. The optical output has revealed to be enhaced for low current injections and along the ageing of the devices, and this is evident both from the L-I plots and the computation of the OP trend for a current of 100 mA. A slight increase of the OP is noticed even under a higher current injection. The overall chromatic features are pretty constant during the ageing, thus no variation of the phosphors performance has been noticed. In the two cases the devices present the same behaviour, e.g. the analyzed L-I curves are pretty equal and even the chromaticity did not changed nor showed dependance from the current and temperature condition.

- The OSLON LEDs are evidently decreasing their OP during the ageing, and this is essentially due to the generation of nonradiative centers. Since the results obtained in the first and the second stress condition are the same even though there are 500 hours of difference, it is clear that a higher current injection lead to an accelaration of the decay trend. The nonradiative centers are thus represented by defects current-diffused in the active layer. Their presence is put in evidence by the L-I trends and by the creation of a preferential path for the current flow that is pointed out in the I-V plots. The diffusion of imperfections is esclusively due to the current injection and no dependence is demonstrated from the temperature at which the devices were operated. On the other hand in both cases the high current operation is still suffering a general decay of the luminous output that is caused by the nonradiative decays, while the electric behaviour is affected by a slight increase of the current flow for high voltages that is due to the creation of a resistance in parallel to the normal diode scheme. The chromaticity of the devices is shown to suffer of a slight shift towards a warmer color, which can imply a modification of the phosphors behaviour, that are enhancing their efficiency, or can be due to the lowering of the blue peak in respect to the yellow radiation that is thus prevalent.

- The REBELs are increasing their OP during the ageing, and no substantial creation of nonradiative centers is observed. Despite of this the threshold voltage is affected by

a slight decay and the high voltage operation reveals a drastic lowering of the current absorption during the ageing. This is also dependant from the temperature at which the LEDs operated, and is consistent with the hypotesis of the creation of a serial resistance due to the worsening of the ohmic contacts. Moreover this resistance should enhance the OP decay especially for high currents, but this has not been observed, apart from the slight decay noticed in the devices mounted onto the MCPCB and operating at the ambient temperature of 85 ^oC. Even in this case the phosphors are increasing their efficiency, because the chromatic coordinates are observed to rise during the ageing. All these features have been verified in both the ageing processes, especially the OP increase has revealed to reach the same levels. This is again a confirmation that the higher current flow of 1.2 A produced an accelerated ageing in respect to the one performed at 700 mA.

A complexive comparison of the two ageing processes reveal that the three devices are seen to reach the same levels of OP relative to the first measurement, although there is a difference of about 500 hours of operation between the last two measurements. This fact yields to consider the second stress condition to be more accelerated than the first. Since the only substantial difference in the two conditions is the much elevated current injection in the second case, and because no difference among the results concerning the various temperatures has been noticed, we can appoint that the investigated processes, i.e. the generation of nonradiative centers, are induced by this high current flow, while the temperature influence is noticed only in the last measurements, and should be more investigated through a longer ageing time.

In Table 7.1 (a) and (b) there is a confirmation of the accelerated dynamics provided by the second ageing process. As a matter of fact, tables present the OP level relative to the first measurement and reached after 500 hours of operation in both the two stress processes. In 7.1 (a) the values are relative to a forward current of 100 mA, while in 7.1 (b) they are retrieved from a current injection of 700 mA: this allows a comparison between the OP degradation under a low and high current injection. In both the two tables the involved dynamics appear evidently accelerated in the second ageing process, because the values reported in the righmost column are seen to maintain the same trend of the ones provided by the lower-current stress, but they are mostly amplified. For example the OP decay of the OSLON devices is noticeable in the first case, and especially under a low current

injection (first table), but it is much more evident under a higher current injection, and the same observation is due to the increase of OP for the low-current operation in the XP-G devices. The REBELs are shown to maintain the same OP level in both the conditions and this is consistent with the previous observations, in which the graphs of the OP decay vs. ageing time were seen to mantain a moderate increase. Moreover the results obtained in both the conditions are again demonstrated to not depend from the ambient temperature.

(a)

LED Name	T_{amb}	OP (%), aged @ 700 mA	OP (%), aged @ 1.2 A
XPG	45	-0.32	+9.95
XPG	65	+5.90	+12.82
XPG	85	N.A.	+11.94
OSLON	45	-7.68	-14.28
OSLON	65	-8.56	-12.88
OSLON	85	-10.04	-27.09
REBEL	45	+3.08	+3.03
REBEL	65	+3.12	+2.57
REBEL	85	-0.33	+3.15

(b)

LED Name	T_{amb}	OP (%), aged @ 700 mA	OP (%), aged @ 1.2 A
XPG	45	-4.71	+2.77
XPG	65	-0.21	+4.55
XPG	85	N.A.	+4.50
OSLON	45	-4.54	-6.41
OSLON	65	-4.49	-7.03
OSLON	85	-5.08	-7.81
REBEL	45	+3.56	+3.77
REBEL	65	+3.42	+2.76
REBEL	85	+0.05	+3.92

Table 7.1: Relative OP calculated for each board from the average of four LEDs , and normalized to the initial measurement. The values refer to an ageing of 500 hours and the OP is measured for a current injection of 100 mA (a) and 700 mA (b).

The low correlation between the temperature of the devices and the reached OP is evident

in Table 7.2 and 7.3, where are presented the OP levels reached for every single LED stressed at 700 mA and 1.2 A respectively, together with the junction temperature calculated in the thermal analysis. The reported temperatures and the degradation values are a confirmation of the fact that the involved processes were mostly not dependant from the temperature.

LED Name	T_{amb}	T_j	OP (%)
PCB_XPGB_1	45	110.5	+1.70
PCB_XPGB_2	45	107.4	N.A.
PCB_XPGB_3	45	99.5	N.A.
PCB_XPGB_4	45	102.8	-11.13
PCB_XPGC_1	65	135.8	-3.00
PCB_XPGC_2	65	144.9	+4.04
PCB_XPGC_3	65	127.6	-1.65
PCB_XPGC_4	65	131.4	N.A.
PCB_XPGA_1	85	167.5	N.A.
PCB_XPGA_2	85	170.3	N.A.
PCB_XPGA_3	85	156.4	N.A.
PCB_XPGA_4	85	145.9	N.A.
PCB_OSLONB_1	45	147.5	-3.71
PCB_OSLONB_2	45	160.4	-5.25
PCB_OSLONB_3	45	129.3	-3.60
PCB_OSLONB_4	45	128.8	-5.58
PCB_OSLONC_1	65	156.5	-8.97
PCB_OSLONC_2	65	166.6	+0.71
PCB_OSLONC_3	65	145.3	-6.38
PCB_OSLONC_4	65	152.0	-3.31
PCB_OSLONA_1	85	193.3	-7.01
PCB_OSLONA_2	85	189.4	-2.59
PCB_OSLONA_3	85	205.4	-6.11
PCB_OSLONA_4	85	245.7	-4.63

LED Name	T_{amb}	T_j	OP (%)
PCB_REBELB_1	45	124.4	+3.23
PCB_REBELB_2	45	130.7	+3.24
PCB_REBELB_3	45	120.8	+3.81
PCB_REBELB_4	45	119.2	+3.97
PCB_REBELC_1	65	175.3	+4.70
PCB_REBELC_2	65	174.1	+2.68
PCB_REBELC_3	65	167.8	+3.41
PCB_REBELC_4	65	158.4	+2.90
PCB_REBELA_1	85	169.4	+0.07
PCB_REBELA_2	85	188.1	-0.32
PCB_REBELA_3	85	171.6	+1.14
PCB_REBELA_4	85	176.0	-0.71

Table 7.2: The ambient and junction temperatures of each LED mounted on the MCPCBs (expressed in ^oC), together with the percentage OP level reached after 500 hours of operation at 700 mA, relative to the initial measurement and calculated for a current of 700 mA. The results of some XP-G devices are not reported, and this is due to the catastrophical failures descripted in section 7.1.

LED Name	T_{amb}	T_j	OP (%)
star_XPGA_1	45	103.7	+3.73
star_XPGA_2	45	102.0	+3.75
star_XPGA_3	45	101.1	+2.06
star_XPGA_4	45	102.2	+1.53
star_XPGB_1	65	130.8	+4.21
star_XPGB_2	65	127.7	+4.89
star_XPGB_3	65	137.5	N.A.
star_XPGB_4	65	125.4	N.A.
star_XPGC_1	85	155.7	N.A.
star_XPGC_2	85	152.6	+3.59
star_XPGC_3	85	143.8	+5.40
star_XPGC_4	85	145.4	N.A.
star_OSLONA_1	45	158.9	-7.04
star_OSLONA_2	45	171.9	-1.39
star_OSLONA_3	45	140.0	-6.56
star_OSLONA_4	45	114.6	-10.64
star_OSLONB_1	65	135.0	-9.73
star_OSLONB_2	65	166.6	-4.48
star_OSLONB_3	65	158.5	-10.70
star_OSLONB_4	65	142.0	-3.20
star_OSLONC_1	85	195.4	-8.09
star_OSLONC_2	85	157.2	-4.80
star_OSLONC_3	85	160.2	-12.99
star_OSLONC_4	85	193.8	-5.38

LED Name	T_{amb}	T_j	OP (%)
star_REBELA_1	45	116.5	+4.50
star_REBELA_2	45	145.2	+3.24
star_REBELA_3	45	131.5	+2.84
star_REBELA_4	45	106.6	+4.52
star_REBELB_1	65	141.4	-0.25
star_REBELB_2	65	167.9	+4.82
star_REBELB_3	65	159.0	+3.35
star_REBELB_4	65	148.5	+3.13
star_REBELC_1	85	164.7	+3.77
star_REBELC_2	85	202.6	+4.52
star_REBELC_3	85	172.0	+3.96
star_REBELC_4	85	155.1	+3.42

Table 7.3: The ambient and junction temperatures of each LED mounted on the star PCBs (expressed in ^oC), together with the percentage OP level reached after 500 hours of operation at $1.2\ A$, relative to the initial measurement and calculated for a current of $700\ mA$. The results of some XP-G devices are not reported, because of the lens contamination descripted in section 7.1.

Conclusions

In this work various aspects of the LED reliability have been investigated, and many observations and suggestions are possible. Even though the examined devices are in this moment commercialized and used in the LED SSL, their reliability is still under investigation and decisive improvements are needed to obtain a better products.

The thermal management is stated to depend both from the chip thermal resistance, and moreover from the board on which the devices are solded: the latter has demonstrated to represent the upper bound of the thermal resistance of the whole device, thus the research of thermally-improved PCBs could be a solution in the quest for an optimal thermal dissipation. Once a lower thermal resistance from junction to ambient is obtained, the temperature achieved within the chip is lowered, thus either a longer lifetime or a greater current injection are allowed: both these conditions represent a success for the LED technology. As a matter of fact, the two ageing conditions, in which the devices were operated at approximately the same temperature but different currents, highlighted the fact that a certain OP decay can be reached both by devices with a higher thermal resistance and lower current, and vice versa with devices stressed at higher currents but with a lower thermal resistance. Since the OP trend has been emphasized during the high current operation of the second set of devices, we can appoint that the investigated dynamics are in most of the cases current-induced, and a higher current injection yields to an acceleration of the phenomena here reported.

The optical power decay is strictly bonded not only to the thermal managements, but

moreover to the device structure. In particular the three studied devices, that evidently offered different configurations of chip and package structure, presented each a peculiar degrading trend. The observations made in their expositions yield to the following considerations:

- the design issue can be decisive in the optimization of the LED performances: even if the intrinsic thermal resistance of the REBEL devices is not the highest, this LED is the most performant in terms of OP along the ageing process, because its optical output is observed to not significantly decrease even after 1000 hours of operation, and even though some problems concerning the generation of nonradiative centers and the increase serial resistance has been encountered. The chip design of this package can be actually improved, moreover the resistance issue should be eliminated, but very high optical performances are noticed;

- the dimensions of the device are strictly correlated both with the thermal resistance and the temperature affordable, and with the optical decay: the OSLON devices are the ones in which not only the area and the maximum achievable temperature are the lowest, but also the electrical absorbed power is the highest. These features are certainly correlated with the poor optical and electrical performance of these devices, that presented a non-neglegible creation of nonradiative centers during the ageing which led to the monotonic decay of the OP;

- not only the electrical and optical features are fundamental in a SSL device, but also its chemical robustness is an important requirement to assure the long life and the non-variability of the optical properties. The XP-G devices have demonstrated to offer a great optical performance under stress conditions, that is partially given by the quite constant electric behaviour along the ageing. Nevertheless these devices revealed to be quite weak from the chemical point of view: in particular the action of contaminants during the soldering process has been deleterious on the epoxy lens. The investigation conducted in this matter revealed how a simple staining of the lens over the chip can lead to a complete wasting of the device and, since the same procedure did not influence the operation of the other two LEDs , further improvements of the lens chemical structure are suggested.

The studied device are all the state-of-art of the commercial LEDs , and they are actually used as part of the LED -based lamps. They demonstated to suffer of a substantial OP

decay only after several hours, thus the complexive performance observed in this work is satisfactory. Even the measured efficiency is the one expected: the measurements render a value of 100 lm/W for almost all the devices, which, if compared with the 18 lm/W of the incandescent lighting, would lead to a lowering of the 80 % of the power consumption in respect to the old technology. The efficiency trend during the ageing has not been considered, but the slight decay of the OP suggests that this technology is capable of a high efficiency but still unreliable and not constant over the lifetime of one device. From the optical point of view, the color characteristics have demostrated to remain quite constant along the ageing, which means that the blue LED -phosphors system is to consider stable and reliable, and moreover that the changes in the chip, lens and package structure did not influence in the chromatic properties of these devices.

Concluding, the suggested improvements concern the electrical characteristics of the devices, with a review of the chip structure and the further reduction of lattice imperfections/impurities that are considered the principal cause of the generation of nonradiative centers here observed. A deeper investigation should be conducted as well on the structural changes of the chip during the ageing, concerning the variations of the dopant concentration and the eterostructure conformation.

Bibliography

[1] I.L. Azevedo, M.G. Morgan, F. Morgan, *The Transition to Solid-State Lighting*, Proceedings of the IEEE, Vol. 97, No. 3, March 2009;

[2] Optoelectronic Devices course didactical material, followed in the academic year 2009/2010;

[3] S.M. Sze, Kwok K. Ng, *Physics of semiconductor devices*, Wiley Interscience, 2007;

[4] E.F. Schubert, *Light Emitting Diodes*, Cambridge Univ. Press;

[5] M.R. Krames, O.B. Shchekin, R. Mueller-Mach, G.O. Mueller, L. Zhou, G. Harbers, M.G. Crawford, *Status and Future of High-Power Light-Emitting Diodes for Solid-State Lighting*, Journal of display technology, Vol. 3, No. 2, June 2007;

[6] M.H. Crawford, *LEDs for Solid-State Lighting: Performance Challenges and Recent Advances*, IEEE Journal of selected topics in quantum electronics, Vol. 15, No. 4, July/August 2009;

[7] K. Bando, K. Sakano, Y. Noguchi, Y. Shimizu, *Development of High-bright and Pure-white LED Lamps*, J. Light & Vis. Env, Vol. 22, No. 1, 1998;

[8] A. Laubsch, M. Sabathil, J. Baur, M. Peter, B. Hahn, *High power and high efficiency InGaN based light emitters*, IEEE Transactions on Electron Devices, 2009;

[9] Y. Narukawa, M. Ichikawa, D. Sanga, M. Sano, T. Mukai, *White light emitting diodes with super-high luminous efficacy*, Journal of Physics D: Applied Physics, Vol. 43, August 2010;

[10] Y. Xi, E.F. Schubert, *Junction-temperature measurement in GaN ultraviolet light-emitting diodes using diode forward voltage method*, Applied Physics Letters, Vol. 85, September 2004;

[11] Datasheet for Cree XLamp XP-G LEDs available at
`http://www.cree.com/products/pdf/XLampXP-G.pdf`
(Last update: 31 August 2011);

[12] Datasheet for OSRAM OSLON LCW CP7P.PC LEDs available at
`http://www.osram-os.com/osram_os/EN`
(Last update: 25 July 2011);

[13] Datasheet for PHILIPS LUXEON REBEL General purpose white LEDs available at
`http://www.philipslumileds.com/uploads/28/DS64-pdf`
(Last update: 20 August 2010);

[14] D.N. Donahoe, *Thermal Aspects of LED Automotive Headlights*, Vehicle Power and Propulsion Conference, 2009;

[15] Datasheet for the 2612 SourceMeter, available at
`http://www.keithley.com/data?asset=50827`;

[16] Datasheet for the 3488A Switch Unit, available at
`http://www.testequipmentdepot.com/usedequipment/pdf/3488A.pdf`;

[17] Labsphere Company, *A guide to integrating sphere theory and applications*, available at
`http://www.labsphere.com/uploads/technical-guides`;

[18] OceanOptics Company, USB2000 spectrometer datasheet, available at
`www.oceanoptics.com/technical/USB2000␣Operating␣Instructions.pdf`;

[19] R.H. Horng, J.S. Hong, Y.L. Tsai, D.S. Wuu, C.M. Chen, C.J. Chen, *Optimized Thermal Management From a Chip to a Heat Sink for High-Power GaN-Based Light-Emitting Diodies*, IEEE Transactions on Electron Devices, Vol. 57, No. 9, September 2010;

[20] N. Wang, A. Hsu, A. Lim, J. Tan, C. Lin, H. Ru, T. Jiang, D. Liao, *High Brightness LED Assembly using DPC substrate and* Super*MCPCB*, Microsystems, Packaging, Assembly and Circuits Technology Conference, 2009;

[21] J. Singh, *Semiconductor Optoelectronics - Physics and Technology*, McGraw - Hill, Inc.;

[22] L. Trevisanello, M. Meneghini, G. Mura, M. Vanzi, M. Pavesi, G. Meneghesso, E. Zanoni, *Accelerated Life Test of High Brightness Light Emitting Diodes*, IEEE Transactions on Device and Materials Reliability, Vol. 8, No. 2, June 2008;

[23] M. Meneghini, A.Tazzoli, G. Mura, G. Meneghesso, E. Zanoni, *A Review on the Physical Mechanisms That Limit the Reliability of GaN-Based LEDs*, IEEE Transactions on Electron Devices, Vol. 57, No. 1, January 2010;

[24] J. Hu, L. Yang, W. Shin, *Electrical, optical and thermal degradation of high power GaN/InGaN light-emitting diodes*, Journal of Physics D: Applied Physics, Vol. 41, No. 3, February 2008;

[25] M. Meneghini, L.R. Trevisanello, G. Meneghesso, E. Zanoni, *A Review on the Reliability of GaN-Based LEDs*, IEEE Transactions on Device and Materials Reliability, Vol. 8, No. 2, June 2008;

[26] T. Yanagisawa, *Estimation of the Degradation of InGaN/AlGaN Blue Ligh-Emitting Diodes*, Microelectronic Reliability, Vol. 37, No. 8, August 1997;

[27] A. Uddin, A.C. Wei, T.G. Andersson, *Study of degradation mechanism of blue ligh emitting diodes*, Thin Solid Films, Vol. 483, No. 1/2, July 2005;

Ringraziamenti

Alla fine di questo lungo ma appassionante cammino volevo ringraziare prima di tutto la mia famiglia, che mi ha supportato e soprattutto capito nei momenti più difficili e impegnativi, questo traguardo lo devo a loro: grazie, senza di voi non sarei quello che sono oggi.

In conclusione di questa esperienza di tesi vorrei ringraziare il mio relatore Enrico Zanoni per avermi dato questa possibilità, e dire un forte grazie ai due Matteo con i quali ho lavorato a stretto contatto in questi mesi: il primo per avermi tracciato il solco del lavoro e accompagnato passo passo negli sviluppi e nei problemi, il secondo per aver risposto con infinita pazienza al migliaio di domande che gli ho fatto e per avermi aiutato a risolvere i più svariati e inimmaginabili problemi quotidiani. Devo ringraziare anche gli altri ragazzi in laboratorio come Nicola, Simone, Carlo, Marco, Diego e Alessandro, ai quali ho chiesto più volte qualche consiglio nei momenti di difficoltà, e che mi hanno risposto con una mano tesa e disponibile.

Sentiti ringraziamenti li devo anche agli amici universitari nonchè compagni di viaggio come Matteo Meneghesso con il quale non penso sia passata una giornata senza una bella cazzata, Michele ('T-T-Toh! Cosa fai tu, r-r-ragazzo?'), l'altro Matteo, l'altro Michele, Massimo (che spero applichi la sua capacità di massimizzare i profitti col minimo sforzo anche per la laurea!), Riccardo, Marco, Matteo e Antonio (che però qualcuno chiama Alessandro...).

Non posso non ringraziare i miei amici da una vita: Chiara grazie mille sei stata bravissima a correggere la montagna di errori che ho fatto, non so come sdebitarmi! Stefania grazie dei bellissimi momenti passati insieme, sei un'amica fenomenale di quelle che tutti dovrebbero avere! Alessio Falso Fasolo grazie per tutte le volte che hai insistito perchè uscissi ma io dovevo studiare e forse qualche volta mi hai pure convinto, Alessio Zagallo Amerrica Do Brazial, Stella, Riccardo, Antonio, Sara e Giuseppe, non riesco a pensare a nessun momento passato con voi senza il divertimento e il sorriso nel cuore: grazie delle risate e del bellissimo tempo passato insieme!